University of Groningen

Accurate relative stopping power prediction from dual energy CT for proton therapy

van Abbema, Joanne Klazien

IMPORTANT NOTE: You are advised to consult the publisher's version (publisher's PDF) if you wish to cite from it. Please check the document version below.

Document Version
Publisher's PDF, also known as Version of record

Publication date:
2017

Link to publication in University of Groningen/UMCG research database

Citation for published version (APA):
van Abbema, J. K. (2017). *Accurate relative stopping power prediction from dual energy CT for proton therapy: Methodology and experimental validation*. Rijksuniversiteit Groningen.

Copyright
Other than for strictly personal use, it is not permitted to download or to forward/distribute the text or part of it without the consent of the author(s) and/or copyright holder(s), unless the work is under an open content license (like Creative Commons).

The publication may also be distributed here under the terms of Article 25fa of the Dutch Copyright Act, indicated by the “Taverne” license. More information can be found on the University of Groningen website: https://www.rug.nl/library/open-access/self-archiving-pure/taverne-amendment.

Take-down policy
If you believe that this document breaches copyright please contact us providing details, and we will remove access to the work immediately and investigate your claim.

Downloaded from the University of Groningen/UMCG research database (Pure): http://www.rug.nl/research/portal. For technical reasons the number of authors shown on this cover page is limited to 10 maximum.

Download date: 12-10-2022

Accurate relative stopping power prediction from dual energy CT for proton therapy

Methodology and experimental validation

PhD thesis

Joanne van Abbema

The research presented in this thesis has been in part funded by the 'Stichting voor Fundamenteel Onderzoek der Materie (FOM)', which is financially supported by the 'Nederlandse Organisatie voor Wetenschappelijk Onderzoek (NWO)' and by Siemens Healthcare (Forchheim, Germany).

university of groningen

kvi - center for advanced radiation technology

Cover: Particle interaction and energy loss.
Printed by: Gildeprint – Enschede

ISBN: 978-94-6233-764-0 (printed version)
ISBN: 978-94-6233-765-7 (electronic version)

rijksuniversiteit
groningen

Accurate relative stopping power prediction from dual energy CT for proton therapy

Methodology and experimental validation

Proefschrift

ter verkrijging van de graad van doctor aan de
Rijksuniversiteit Groningen
op gezag van de
rector magnificus prof. dr. E. Sterken
en volgens besluit van het College voor Promoties.

De openbare verdediging zal plaatsvinden op

vrijdag 24 november 2017 om 12.45 uur

door

Joanne Klazien van Abbema

geboren op 12 september 1984
te Berkel en Rodenrijs

Promotor
Prof. dr. S. Brandenburg

Copromotores
Dr. E.R. van der Graaf
Dr. M.J.W. Greuter

Beoordelingscommissie
Prof. dr. B.J.M. Heijmen
Prof. dr. ir. E.N. Koffeman
Prof. dr. ir. J.M. Schippers

Contents

Chapter 1

General introduction

1.1 Introduction

Over the last decades, knowledge based technological developments have improved the quality in treatment of cancer. The success of treatment increases but cancer still remains a challenging disease to cure considering the 5 year survival rate of patients of around 60%[1]. The life expectancy strongly depends on the type of tumour and the extension of the disease. Improvement of the treatment is needed to achieve a higher cure rate.

In 40 to 50% of the cases radiotherapy is part of the treatment[2]. Radiotherapy is either applied as the primary treatment or combined with chemotherapy and/or surgery. Conventional radiotherapy includes internal irradiation of tumours using radioactive sources (brachytherapy) and external beam irradiation using high energy photons or electrons. External beam therapy has developed from simple treatments with 2 or 3 combined static fields to intensity-modulated radiotherapy (IMRT) and volumetric-modulated arc therapy (VMAT). IMRT and VMAT can provide dose distributions with a higher conformity to the tumour reducing the dose to surrounding healthy tissues and critical structures[3,4]. This information technology-driven development of dose delivery optimization has led to a reduction in the probability and severity of radiation induced complications, but due to the physics of dose deposition by photons and electrons the possibilities for further significant improvement are very limited[2]. Energetic protons or other ions have a finite range and a strong maximum in dose deposition (Bragg peak) at the end of their path. Their potential clinical use for therapy was first suggested by Robert R. Wilson in 1946[5]. By using these ions for therapy further improvement in the conformity of dose distributions can be achieved[2]. This is expected to result in a decrease of radiation induced complications as compared to the most advanced radiotherapy with photons and electrons. In the Lawrence Berkely Laboratory in California experimental studies with proton, deuteron and helium beams on mice were performed followed by treatment of the first patients with protons and helium ions in 1954. The Gustav Werner Institute in Uppsala (Sweden) treated the first patient with protons in Europe in 1957. In a dedicated facility developed in a collaboration between the Harvard Cyclotron Laboratory and Massachusetts General Hospital the first patients were treated with protons in 1961 up to a total of 9116 patients until 2002.[6] The first facility for proton therapy inside a hospital was built in 1990, the Loma Linda University Medical Center in California, where in total a number of over 17,500 patients were treated up to now for various types of tumours[7]. Children and patients with tumours in the head and neck region (including eye tumours) provide the most important indications for particle therapy.

For the growing number of patients treated with radiotherapy that survive cancer, radiation induced toxicity and secondary tumours are important risks. Compared to radiotherapy with photons radiotherapy with ion beams can, in principle, reduce these risks by providing a higher conformity of the high dose region to the tumour. Due to the finite range and Bragg peak an important challenge of radiotherapy with ion beams lies in the accurate positioning of the high dose region in the tumour volume. This requires an accurate method to convert imaging data of a patient to a planned dose distribution. In this study we aim at developing a new method based on photon imaging to more accurately characterize tissues for proton dose calculations. Photons and ions interact differently with matter. This difference is not only responsible for the differences in dose deposition, but has also to be taken into account in the translation of x-ray imaging information into the material properties needed to accurately predict the dose deposition by protons. A short description of the processes in which photons and protons loose energy to matter is provided in the next section. More details on the relevant photon interaction processes for imaging are given in chapter 2. In chapter 3 and 4 the theory on proton interactions will be discussed.

1.2 Energy loss of photons and protons

1.2.1 Photon interactions with tissue

Photons interact with tissue through photoelectric absorption, coherent (Rayleigh) scattering, incoherent (Compton) scattering and pair production. Photoelectric absorption can take place if the photon energy is large enough to overcome the binding energy of the electron and liberate the electron from its shell. If an inner shell (e.g. K-shell) vacancy is filled by an electron from an outer shell a photon is emitted with an energy equal to the difference in energy levels between the two shells. These photons are called characteristic x-rays. For high Z materials the difference between the energy levels is large enough to produce x-rays with sufficient energy to travel a certain distance in tissue. In low Z materials the x-rays are absorbed locally. Rayleigh scattering is an interaction of the photon with the whole atom which causes a small angle deflection of the incident photon. In Compton scattering the incident photon transfers some of its energy to an electron. After the interaction, the incident photon is deflected and the electron recoils where the angle of recoil and energies of the electron and scattered photon are determined by conservation of energy and momentum. When the energy of the incident photon is larger than 1.022 MeV, pair production is possible.

In the interaction of photons with the tissue through photoelectric absorption, Compton scattering and pair production energetic secondary electrons are produced. These electrons transfer their energy to the tissue by collisions with atomic electrons (collisional energy loss) and interactions with the electric field of the nuclei (radiative energy loss, bremsstrahlung). When a secondary electron removes an atomic electron from its shell the atom is ionized, when it transfers energy to an atomic electron the atom is excited. Collisional energy loss through ionization and excitation of atoms depends on the electron's energy and the electron density of the tissue (number of electrons per unit volume). Radiative energy loss increases with atomic number and electron energy.[8,9]

1.2.2 Proton interactions with tissue

Protons predominantly loose energy by ionization and excitation of atoms. In the frequent Coulomb interactions the protons transfer energy to the electrons in the tissue and travel along a nearly straight path. For clinically relevant proton energies (< 250 MeV), the energy gained by the secondary electron in each interaction is just enough to travel a few millimetres in tissue. When a proton travels in the vicinity of an atomic nucleus it is subject to a repulsive Coulomb force which deflects the proton from its original path. This process is called elastic (without energy transfer) Coulomb scattering. These small angle deflections of the protons cause an increase of radial beam spread with depth. In an inelastic nuclear reaction of the proton with an atomic nucleus the primary proton is removed from the beam and the reaction products are secondary protons, heavy ions, neutrons or γ-rays.

The energy loss of protons to the electrons is quantified by the electronic stopping power of the tissue. This electronic stopping power can be estimated with the Bethe-Bloch equation which depends on the electron density and mean excitation energy of the tissue. The mean excitation energy is determined by the composition of the tissue and represents an interaction probability weighted effective value of the minimum possible energy transfer in a collision. The electronic stopping power is proportional to the electron density and increases with decreasing proton energy up to a maximum. The maximum of the energy loss (the Bragg peak) occurs at approximately 70-80 keV for protons in water.[10,11]

1.2.3 Photon and proton dose distributions

The difference between the dose as a function of depth for photons and protons in water is visualized in figure 1.1. The depth dose distribution of photons with therapeutic energies (6-15 MV) in water shows a dose build-up region of approximately 1.5 to 2.5 cm depth due to the relatively long range of the forward scattered electrons. These secondary electrons transfer the energy lost by the photons to the medium. The position of the dose maximum depends on the energy of the secondary electrons which depends on the primary energy of the photons. After this dose maximum the dose nearly exponentially decreases with depth due to the exponential attenuation of the photon beam with traversed distance.

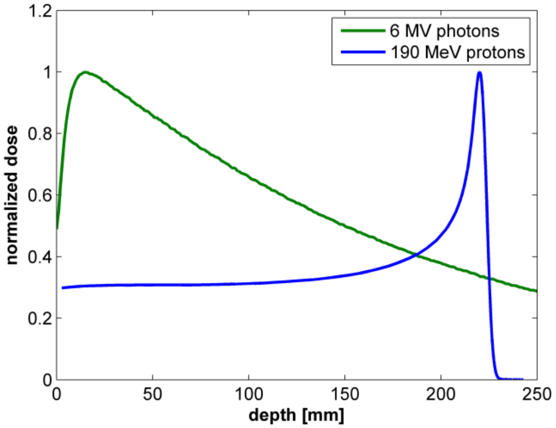

Figure 1.1. Normalized depth dose distributions for 6 MV photons and 190 MeV protons measured in water.

Protons continuously transfer energy to the electrons in the medium by Coulomb interactions. The proton energy (and velocity) decreases, increasing the stopping power and initiating the relatively sharp Bragg peak. After the steep distal falloff the protons have lost their kinetic energy and are stopped. Since the number of collisions and energy loss per collision are stochastically distributed, energy and range straggling determine the width and gradient of the distal falloff of the Bragg peak. The interaction probability of protons and other ions is much larger than for photons, while the energy transfer in each interaction is large for photons and small for protons.[8,10,11]

In photon therapy, in general several fields are combined to achieve a conformal high dose in the tumour while optimally sparing critical structures. With IMRT, dose constraints can be allocated to critical structures and used in treatment planning optimization. The dose distribution achieved in this optimization process is limited by the physical characteristics of photons as visualized in figure 1.1. Therefore in general, IMRT leads to a redistribution of dose from critical structures to surrounding tissues and an increase of the integral dose (total energy deposited) with respect to conventional approaches. This increase in integral dose, by increasing the irradiated volume, is an important risk factor for secondary tumour development which is mainly of importance for young patients and patients with a substantial life expectancy considering the latency period of 5 to 10 years.[12] In contrast, when using protons, the low entrance dose and finite range enable localizing the high dose region at the tumour while sparing surrounding critical structures. The state of the art technique for proton therapy is pencil beam scanning with range and intensity modulation[13,14].

1.2.4 Monte Carlo dose calculation

Monte Carlo simulations are often used for verification of dose calculations in quality assurance of photon and proton therapy treatment planning. Monte Carlo simulations are transport calculations of all the particles and photons produced in the interactions of photons or protons with a medium. Each individual particle is tracked until the user specified range cut value is reached.[15] The different interaction processes are included in the simulations. In particular for heterogeneous treatment sites in proton therapy, Monte Carlo simulations provide a more reliable dose distribution compared to the analytical dose calculation algorithms used in most treatment planning systems. By calculating the transport of individual particles, Monte Carlo simulations can more accurately predict multiple Coulomb scattering than analytical algorithms.[16] To characterize the medium, Monte Carlo simulations require the mass density and composition as an input. For application in treatment planning this information needs to be derived from imaging data of a patient.

1.3 Radiotherapy and proton therapy treatment planning

For treatment planning in radiotherapy and proton therapy, x-ray computed tomography (CT) imaging data of the patient is used to characterize the tissue in terms of density, electron density or proton stopping power. These parameters are used for calculation of the dose to the tissue. The steep dose gradients of protons, in particular at the distal falloff of the Bragg peak, cause an increased sensitivity to non-accurate tissue characterization compared to photons. A small error in proton stopping power estimation can potentially cause a clinically relevant range shift of the proton beam. As a consequence, healthy tissue can receive a high dose or part of the tumour receives no dose. For photons, a small error in the depth dose calculation only corresponds to a relatively small shift on the exponential falloff (figure 1.1). Therefore the quality of tissue characterization is more critical for proton than for photon therapy.

1.3.1 X-ray computed tomography

Computed tomography (CT) images are reconstructed from measured transmitted intensity profiles of a photon beam after traversing a slice of the patient's body. Datasets of transversal slices (xy plane) are reconstructed from helical scans acquired by a system of an x-ray tube producing a fan photon beam and an opposing detector matrix measuring the transmitted photon intensity, rotating over 360 degrees around the patient (figure 1.2).

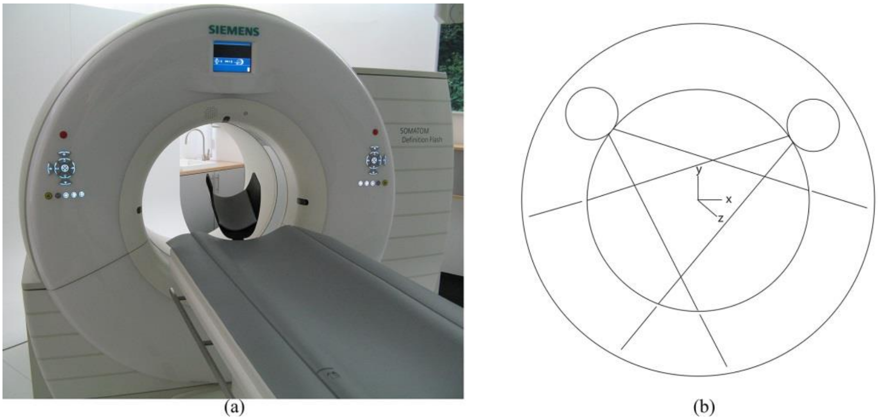

(a) (b)

Figure 1.2. (a) Dual source computed tomography (DSCT) system. (b) Schematic drawing of the two x-ray tubes (circles) producing a fan photon beam and opposing detector systems.

Reconstructed CT images provide a 3D matrix of voxels filled with CT numbers, given in Hounsfield units (HU), representing the linear attenuation coefficient μ of the tissue relative to water averaged over a certain volume element (voxel). The minimal size of this voxel is determined by the scanner resolution in the x and y direction and the reconstructed slice thickness in the z direction. For modern CT systems the xy resolution is in the order of 0.4 mm and the z resolution in the order of 0.6 mm. The x-ray tube in a CT system typically consists of a cathode assembly with a hot filament emitting electrons that are focussed by a focussing cup and then accelerated by the tube voltage towards a tungsten anode. In the interaction of the accelerated electrons with the anode material a continuous spectrum of bremsstrahlung photons is produced with a maximum energy corresponding to the electron energy. In addition, characteristic x-rays of tungsten are produced represented by sharp lines at specific energies in the polyenergetic x-ray spectrum.

In figure 1.3a an example of two spectral photon distributions is given. The sharp lines of the characteristic x-ray peaks are broadened due to the energy resolution of the scintillator crystal with which the spectra have been measured. When such a spectrum of photons travels through the tissue low energy photons are more readily absorbed, resulting in an increase of the effective energy of the x-ray beam. This process is called beam hardening. The detector system opposite to the x-ray tube consists of arrays of small scintillator crystals. In figure 1.3b the detector response of a Gd_2O_2S scintillator CT detector is presented. The detector response represents the signal due to the energy deposited in the detector by an incoming photon of energy E. Photons with energies between 1 and 50 keV lose all of their energy in the scintillator and the response is linear. Around 50 keV, an edge in the response corresponds to the K-shell electron binding energy of gadolinium. Just above this energy the detector responsivity suddenly drops because the energy transferred by the photon in photoelectric absorption in the scintillator detector is used to eject the photoelectron and is imparted to the characteristic x-ray. The characteristic x-ray can escape from the scintillator and the depth of the edge in the response depends on the chance of escape of the x-ray. In the balance of energy sharing between the characteristic x-ray and the photoelectron, the energy transferred to the photoelectron steadily increases for higher energies and more energy is deposited in the scintillator due to which the response increases.[10] Above 115 keV the detector response drops due to transmission of photons.

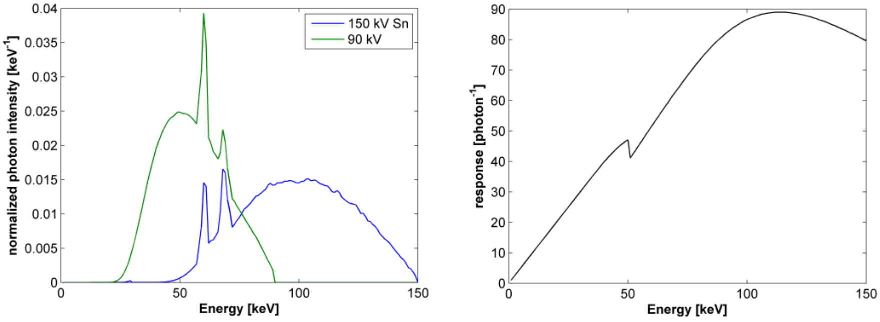

(a) (b)

Figure 1.3. (a) Spectral photon distributions at x-ray tube potentials of 90 kV and 150 kV (with additional Sn filtration). (b) Gd_2O_2S scintillator CT detector response as a function of photon energy. The data is valid for the SOMATOM Force and has been provided by Siemens Medical Solutions, Forchheim, Germany.

1.3.2 CT based treatment planning

The interaction mechanisms of photons and protons with the electrons in the tissue indicate the importance of accurate knowledge of the tissue electron density for dose calculation in both photon and proton therapy. In photon therapy the electron density is needed for calculation of energy transfer due to Compton scattering. Energy transfer by pair production depends on atomic density and atomic number. For proton therapy the energy loss of protons in tissue is determined by the tissue electron density and the mean excitation energy. The composition of the tissue is needed for estimating this mean excitation energy. The current clinical standard for deriving the tissue characteristics is based on single energy CT (SECT) imaging of the patient. For photon therapy a calibration curve relates the measured CT numbers to mass densities or electron densities often based on measurement of a phantom with a range of tissue substitutes. These tissue substitutes are artificial materials with the same attenuation properties for x-rays as tabulated average tissues. In treatment planning systems for proton therapy the CT numbers are related to proton stopping powers relative to that of water (relative stopping powers, RSPs). This relation is obtained from measured CT numbers of tissue substitutes for which the RSPs have been calculated or by using CT numbers and RSPs calculated with tabulated average tissue compositions and densities (stoichiometric calibration method)[17,18]. For Monte Carlo dose calculation an estimate of the mass density and composition of the tissues is generally derived from a lookup table that links CT numbers to mass densities and compositions and is based on data from average tissues[19].

With the introduction of dual source CT[20] and other CT systems enabling dual energy CT (DECT) acquisitions, the application of DECT for radiotherapy treatment planning has become feasible. With DECT linear attenuation coefficients of the scanned object are measured for two different spectral distributions. From these two measured attenuation coefficients and a theoretical model of the dependence of the attenuation coefficient on the atomic number and the electron density, an effective atomic number and electron density can be derived. This is possible because of the difference in energy and atomic number dependency of the photoelectric effect, Rayleigh scattering and Compton scattering. The effective atomic number of the scanned material represents its effective composition for the relevant photon interaction processes at a weighted average of the two spectral photon distributions. Several studies[21,22] have shown the potential of DECT for accurate determination of the electron density. To improve dose calculations for particle therapy (including proton therapy and carbon ion therapy) accurate knowledge of both the tissue electron density and mean excitation energy is required. The logarithm of the mean excitation energy has been related to the effective atomic number[23] but this relation is not single valued over the entire domain. A more accurate tissue mean excitation energy may be derived if a strong relation between the effective atomic number of the tissue and its mean excitation energy can be established. Combined with accurate electron densities this is expected to improve the accuracy of the relative stopping power estimation from CT imaging of a patient.

Other new CT methods in development are spectral CT and proton CT. Spectral CT provides linear attenuation coefficients at more than two energy bins. This is in particular useful for identification of high Z materials, like contrast agents, with a K-edge above 40 keV.[24,25] The added value of spectral CT over dual energy CT for characterization of tissues is a topic for future research. Proton CT has the advantage of using high energy proton beams for imaging, thus directly providing proton stopping powers from energy loss measurements[26]. The limitations for proton CT are energy loss straggling and multiple Coulomb scattering which degrade the spatial resolution of the image. Tracking individual protons by measuring the entrance and exit points and angles of the individual protons enables reconstruction of the proton trajectories and their corresponding energy loss. Single events should be measured in coincidence at the entrance and exit side of a patient to enable accurate reconstruction.[27] Proton CT or radiography can potentially be used for calibration of relative stopping powers derived from dual energy CT.

1.3.3 In vivo dose verification

During treatment the planned dose distribution can be verified in vivo by positron emission tomography (PET) or prompt gamma imaging. In the nuclear interactions of the protons with the tissue short-lived radioactive nuclides are produced which decay by positron emission. When a positron has slowed down it combines with an electron and two 511 keV annihilation photons are emitted at a 180 degree angle which can be detected outside the patient's body. In the decay of excited atomic nuclei in the tissue prompt gamma rays are emitted.[28] With a prototype knife-edge slit camera Richter *et al.*[29] reported on the first clinical application of prompt gamma imaging. Calculation of the radioactive nuclide and prompt gamma ray production in the tissue requires the composition of the tissue. The requirements on the quality of tissue characterization in terms of elemental composition for PET and prompt gamma dose verification are much higher than for dose calculation since the weight percentages of all relevant elements are needed. The accuracy which can be achieved with dose verification is limited by the quality of the tissue characterization.

1.4 Uncertainties associated with proton therapy

The challenge in proton therapy is to realize optimal conformity of the high dose region with the tumour. Uncertainties in the predicted range impose significant restrictions on the treatment planning process, such as large margins due to which healthy tissue receives a high dose and forced suboptimal beam angles and fields in order to avoid possible displacement of the high dose region to nearby organs at risk. Due to the uncertainty in proton stopping power estimation a suboptimal dose distribution limits achieving the full advantage of healthy tissue sparing in proton therapy. The use of SECT for estimation of proton stopping powers introduces two types of uncertainty. Firstly, the stoichiometric calibration method or related calibration curves are generic models with inherent uncertainties. Secondly, the correspondence between tissue properties of individual patients and those assumed in the generic models is uncertain. The SECT models are composed of several linear fits which relate the CT numbers to RSPs. This will not account for the fact that the CT number depends on both the electron density and composition of the tissue. The CT numbers measured in single energy mode are not tissue specific; two different tissues can have the same CT number while having a different electron density and effective atomic number. This reveals the most important advantage of dual energy CT, namely its tissue and patient specificity by deriving both the electron density and effective atomic number of a given tissue in a given patient. This advantage of DECT could, in principle, provide a large improvement in proton stopping power estimation over the SECT models.

In literature different range uncertainties circulate with very limited experimental validation. Range uncertainty margins are typically quoted at 3.5% of the prescribed range in water plus 1 mm to account for uncertainties in patient setup[16,30]. This range uncertainty of 3.5% originates from an uncertainty in the measurement of CT numbers of ~2% and an uncertainty in the translation of CT data to water equivalent densities of ~1%[16]. The uncertainty which arises from the translation of SECT data to relative proton stopping powers using the stoichiometric calibration curve has been estimated by Schaffner and Pedroni[18] at 1% from animal tissue measurements. Including the uncertainty due to beam hardening an uncertainty of 1.8% for bone and 1.1% for soft tissue has been suggested[18]. Paganetti[31] referred to this study and assumed the uncertainty directly attributable to the stoichiometric calibration method (without the uncertainty in mean excitation energy) to be ~0.5%. The corresponding total range uncertainty for inhomogeneous treatment sites has been consequently estimated at 4.6% + 1.2 mm for analytical dose calculation and 2.4% + 1.2 mm for Monte Carlo dose calculation. A generic range uncertainty of 2.7% + 1.2 mm for analytical dose calculation has been proposed.[31] Schuemann *et al.*[16] derived similar values and emphasized the site specificity of range uncertainties and the importance of the dose calculation method.

The correspondence between the tabulated average tissue compositions and densities, used in the extraction of relative stopping powers from SECT data, and the patient specific tissue compositions and densities is unknown. The stoichiometric calibration method assumes that all human tissues are basically very similar to the tabulated tissues. In providing the average values, Woodard and White[17] also analysed the variability of the data and reported a wide spread in composition for e.g. adipose tissue and mammary gland. In a theoretical study, Yang *et al.*[23] compared the sensitivity of the SECT stoichiometric calibration method and a DECT method for variations in elemental composition and density. The DECT predicted RSPs were found to be independent of density variations while for SECT a root mean square (RMS) difference of 2.7% has been found for a 5% change in density. For 5% variations in elemental compositions the RMS differences for SECT are in the order of 4.5% compared to 1.0% for DECT. This indicates the robustness of DECT for variations in tissue composition and density and offers potential for reducing the range uncertainty caused by the conversion of patient CT data to RSPs.

1.5 Aim and overview of this thesis

The aim of this study is to improve the accuracy of dose delivery in proton therapy by reducing the uncertainty in the determination of proton energy loss in tissues from imaging data of a patient. In this work a new DECT analysis method has been developed and described to translate photon interactions with the tissues measured using CT into proton stopping powers required for proton therapy treatment planning. This study provides a comprehensive experimental assessment of the proposed DECT analysis method and the SECT stoichiometric calibration method. From this experimental assessment, the uncertainty in the translation of CT data to proton stopping powers with DECT and SECT is estimated.

In chapter 2 of this thesis a method for the determination of effective atomic numbers and electron densities from DECT images is presented. In this chapter an image based implementation of a local weighting function (LWF)[32] is introduced which provides a local spectral weighting in deriving the effective atomic numbers and electron densities. The accuracy of the method has been assessed on a large phantom for different tissue substitutes and aluminium.

In chapter 3 the method to calculate relative proton stopping powers from the DECT derived effective atomic numbers and electron densities is presented. The predictive value of this method has been examined for 32 materials covering a clinically relevant variety in composition and density. In addition, the accuracy of Geant4 Monte Carlo simulations for RSP prediction has been determined. In this analysis, proton range measurements of the 32 materials relative to water provide high accuracy ground truth RSPs.

Chapter 4 discusses the uncertainties in proton stopping theory. The developed experimental setup for high accuracy proton range measurements is described and measured depth dose distributions are compared to Geant4 Monte Carlo simulations. The factors contributing to the uncertainty in determination of experimental relative stopping powers are estimated.

The proposed DECT analysis method for calculation of RSPs has been compared to the SECT stoichiometric calibration method in chapter 5. Both methods have been compared for the 32 materials and for 17 bovine tissues.

A summary of the most important results and outlook to future research and clinical implementation are presented in chapter 6.

Relative electron density determination using a physics based parameterization of photon interactions in medical DECT

Joanne K van Abbema[1], Marc-Jan van Goethem[2], Marcel J W Greuter[3], Arjen van der Schaaf[2], Sytze Brandenburg[1] and Emiel R van der Graaf[1]

[1] University of Groningen, KVI - Center for Advanced Radiation Technology, Zernikelaan 25, 9747 AA Groningen, The Netherlands
[2] University of Groningen, University Medical Center Groningen, Department of Radiation Oncology, PO Box 30.001 Groningen, The Netherlands
[3] University of Groningen, University Medical Center Groningen, Department of Radiology, PO Box 30.001 Groningen, The Netherlands

Phys. Med. Biol. 2015; 60: 3825-3846

Abstract

Radiotherapy and particle therapy treatment planning require accurate knowledge of the electron density and elemental composition of the tissues in the beam path to predict the local dose deposition. We describe a method for the analysis of dual energy computed tomography (DECT) images that provides the electron densities and effective atomic numbers of tissues.

The CT measurement process is modelled by system weighting functions (SWFs), which apply an energy dependent weighting to the parameterization of the total cross section for photon interactions with matter. This detailed parameterization is based on the theoretical analysis of Jackson and Hawkes and deviates at most 0.3% from the tabulated NIST values for the elements H to Zn. To account for beam hardening in the object as present in the CT image we implemented an iterative process employing a local weighting function (LWF), derived from the method proposed by Heismann and Balda. With this method effective atomic numbers between 1 and 30 can be determined. The method has been experimentally validated on a commercially available tissue characterization phantom with 16 inserts made of tissue substitutes and aluminium that has been scanned on a dual source CT (DSCT) system with tube potentials of 100 kV and 140 kV using a clinical scan protocol.

Relative electron densities of all tissue substitutes have been determined with accuracy better than 1%. The presented DECT analysis method thus provides high accuracy electron densities and effective atomic numbers for radiotherapy and especially particle therapy treatment planning.

2.1 Introduction

Radiotherapy and in particular particle therapy treatment benefit from accurate electron density determination of the tissues to be irradiated. Clinically relevant improvements of dose delivery in proton therapy can be achieved by reducing the systematic uncertainty in the determination of proton energy loss in the tissues from imaging data of the patient[16,33]. Proton energy loss in the tissues determines the position of the high dose and distal dose falloff regions. The positioning of these regions is critical in order to deliver a high dose to the tumour while optimally sparing the surrounding healthy tissues and critical organs. The uncertainty in this energy loss may constrain the treatment planning process to suboptimal beam directions and significant range margins. In a recent study the range margin for heterogeneous treatments sites (e.g. head and neck) has been estimated at 6.3%+1.2 mm[16]. Computed tomography (CT) imaging of the patient provides three dimensional attenuation characteristics of the tumour site and nearby healthy tissues. To predict the range of protons in the tissue, a conversion of these CT data into electron density relative to water and mean excitation energy is needed. The relative proton stopping power strongly depends on the relative electron density and accurate knowledge of this parameter is therefore indispensable[34]. In our study we aim at sub percent accuracy for proton stopping powers at ≤ 1 mm xyz-resolution to provide sufficient resolution for state of the art proton therapy treatment planning using Monte Carlo simulations[16]. The typical beam spot size for pencil beam scanning is around 3 mm (1σ) for large ranges and increases with depth due to scattering in the patient. However, sharp transitions between tissues with a large difference in proton stopping power, e.g. bone and lung, require high resolution imaging data to avoid partial volume artefacts which results in a shift of the predicted range of the protons in the tissue.

As stated by Yang *et al.*[23,30], dual energy CT (DECT) is able to reduce the uncertainty in relative proton stopping powers by simultaneous determination of both the electron density and effective atomic number. To derive these parameters from DECT data an accurate parameterization is required, describing the dependency of the linear attenuation coefficient measured in CT on the electron density and atomic number. Especially the objective of a sub percent accuracy for proton stopping powers demands relative electron densities of tissues at a sub percent level which requires a high accuracy of the parameterization. Different parameterizations based on fitting and interpolation procedures of tabulated cross section data have been described in literature, notably the methods of Rutherford *et al.*[35], Heismann *et al.*[36] and Bazalova *et al.*[37]. A main drawback of directly fitting tabulated cross sections is the limited Z interval which can be accurately covered by a simple fitting procedure. Typically this Z interval is chosen between 5 and 15[37] which spans the range of the effective atomic numbers of inserts in the Gammex tissue characterization phantom (Gammex Inc., Middleton, WI, USA) but excludes hydrogen and calcium from the analysis. Especially hydrogen, with a relatively small contribution of the photoelectric effect, is difficult to include in basic fitting methods. Other approaches have been based on the calculation of CT numbers for mean tissue compositions and densities[19,34] as listed in e.g. ICRP Report 23[38] and White *et al.*[17,39,40]. However, tissue compositions and densities vary between individuals. In addition, the measured CT numbers change with beam hardening in the patient and therefore depend on patient dimensions and tissue arrangement. Calibration methods apply a fitting procedure on data of a tissue characterization phantom in order to determine the relative electron density[41] and effective atomic number[42]. As these methods depend on the phantom used for calibration, their predictive value for human tissues is questionable.

Already in 1981, Jackson and Hawkes[43] proposed a parameterization of the x-ray attenuation coefficient which is accurate over a Z range of 1 to 30 for energies between 30 and 150 keV. This parameterization is based on fundamental theory, rather than on equations that directly fit tabulated cross sections as a function of energy and atomic number. Torikoshi *et al.*[21] made a simplified implementation of this method and assessed it using monochromatic DECT. We have developed a method in which the accurate, physics based parameterization proposed by Jackson and Hawkes has been extended with fit functions of fundamental quantities to obtain a complete equation as a function of energy and atomic number. Using this equation we have derived effective atomic numbers and electron densities from reconstructed CT images with an iterative procedure which accounts for beam hardening in the object and corrections in the CT reconstruction process. This iterative procedure employs a local energy weighting as proposed by Heismann and Balda[32]. We have investigated the quality of the analysis method on experimental DECT data acquired on a dual source CT (DSCT) system.

2.2 Theoretical methods

2.2.1 X-ray spectral attenuation and detection

The attenuation (A_j) of the incoming x-ray spectrum measured in CT is given by

$$A_j = \frac{I_j}{I_{0,j}} = \int_0^\infty w_j(E) \exp\left(-\int_L \mu(E,\boldsymbol{r}) d\boldsymbol{r}\right) dE \qquad (1)$$

where I_j and $I_{0,j}$ are the measured intensities with and without attenuating material, respectively and w_j is the system weighting function (SWF) for spectral distribution j. The spectral attenuation coefficient $\mu(E,\boldsymbol{r})$ for energy E at position $\boldsymbol{r}$ is integrated over the projection path L. The system weighting function is defined by

$$w_j(E) = \frac{S_j(E)D(E)}{\int_0^\infty S_j(E)D(E)dE} \tag{2}$$

with the spectral distribution of the source output after tube filtration $S_j(E)$ weighted with the detector efficiency $D(E)$. For simplification we neglect the influence of the bow-tie filter.

Heismann and Balda[32] related a reconstructed "effective" attenuation coefficient $\bar{\mu}_j(\boldsymbol{r})$ to the actual $\mu(E,\boldsymbol{r})$ of the material by defining a local weighting function (LWF) $\Omega_j(E,\boldsymbol{r})$

$$\bar{\mu}_j(\boldsymbol{r}) = \int_0^\infty \Omega_j(E,\boldsymbol{r})\, \mu(E,\boldsymbol{r})dE \tag{3}$$

and

$$\Omega_j(E,\boldsymbol{r}) = w_j(E)\frac{R^{-1}\{P\{\mu(E,\boldsymbol{r})\}\}}{\mu(E,\boldsymbol{r})} \tag{4}$$

with $R^{-1}\{\cdot\}$ the inverse Radon transform and $P\{\cdot\}$ the measurement operator. This LWF represents the effective spectral weighting at a particular position in the scanned object. The reconstruction and measurement processes are included by $R^{-1}\{\cdot\}$ and the projected sinogram data $P\{\mu(E,\boldsymbol{r})\}$, respectively. A voxel-based LWF can be calculated by replacing the term $R^{-1}\{P\{\mu(E,\boldsymbol{r})\}\}$ by $\bar{\mu}_j(\boldsymbol{r})$ extracted from a reconstructed CT image.

The measured attenuation characteristics of different materials in an object are represented by CT numbers or Hounsfield units, defined as

$$\bar{H}_j(\boldsymbol{r}) = \frac{\left(\bar{\mu}_j(\boldsymbol{r}) - \mu_j^w\right)}{\mu_j^w}1000 \tag{5}$$

where μ_j^w denotes the attenuation coefficient of water.

2.2.2 Determination of effective atomic numbers and relative electron densities

For a compound *l*, the total electronic cross section (${}_e\sigma^{tot}$) is a function of the effective atomic number Z'. The linear attenuation coefficient μ in terms of the electron density (ρ_e^l) and the total electronic cross section is defined as

$$\mu(E) = \rho_e^l \; {}_e\sigma^{tot}(E,Z') \tag{6}$$

where the electron density (ρ_e^l) is the product of the mass density (ρ^l) and the mass electron density (N_g^l)

$$\rho_e^l = \rho^l N_g^l = \rho^l N_A \sum_k \omega_k \frac{Z_k}{A_k} \tag{7}$$

with Avogadro's number N_A, mass fraction ω_k, atomic number Z_k and atomic weight A_k of element k in the compound l. The electron density ρ_e^l is related to the electron density of water ρ_e^w to obtain the relative electron density ρ_e^l/ρ_e^w which is normally used in dose calculations.

Measuring two different attenuation coefficients $\bar{\mu}_j$ by operating the DSCT x-ray tubes at different kV settings, the total electronic cross sections (${}_e\sigma^{tot}$) will be weighted by the SWFs as defined in eq. (2). For spectral distributions $j = 1$ (high kV) and $j = 2$ (low kV) of energies i, the ratio of the measured attenuation coefficients then becomes

$$\frac{\bar{\mu}_1(\boldsymbol{r})}{\bar{\mu}_2(\boldsymbol{r})} = \frac{\int_0^\infty w_1(E)\left({}_e\sigma^{tot}\big(E, Z'(\boldsymbol{r})\big)\right) dE}{\int_0^\infty w_2(E)\left({}_e\sigma^{tot}\big(E, Z'(\boldsymbol{r})\big)\right) dE} \tag{8}$$

Solving this equation gives an effective atomic number Z' for a compound or mixture from the Z dependence of the individual electronic cross sections. The effective electron density ρ_e' can be calculated with one value for $\bar{\mu}_j$ by the use of Z'.

2.2.3 Parameterization of the electronic cross section based on theoretical analysis of photon interactions

A parameterization for the total electronic cross section, as a function of the energy and the atomic number, enables solving eq. (8) to an effective atomic number Z' and subsequently deriving the relative electron densities $\rho_e{}'/\rho_e^w$. Jackson and Hawkes[43] have proposed formulas that accurately parameterize the photon interaction processes over an energy range of 30 to 150 keV, relevant to medical CT. In this energy range, the total electronic cross section for a given element is the sum of the electronic cross section of photoelectric absorption (ph), coherent (coh) and incoherent ($incoh$) scattering

$${}_e\sigma^{tot}(E,Z) = Z^{-1}\left({}_a\sigma^{ph}(E,Z) + {}_a\sigma^{coh}(E,Z) + {}_a\sigma^{incoh}(E,Z)\right) \tag{9}$$

2.2.3.1 Photoelectric effect

The atomic cross section for photoelectric absorption is expressed by Jackson and Hawkes as

$$ {}_a\sigma^{ph}(E,Z) = \left[4\sqrt{2}Z^5\alpha^4\left(\frac{mc^2}{E}\right)^{7/2}\frac{8}{3}\pi {r_e}^2\right]\left[2\pi\left(\frac{\varepsilon_K}{E}\right)^{1/2} f(n_1)\right] \\ [1 + F_{ns}(\beta)]UN(E,Z) \tag{10} $$

in which the first two factors represent the atomic Stobbe cross section (${}_a\sigma_{1s}^{ST}(E,Z)$) for the bound 1s state (*K*-shell). The first factor is the Born approximation and the second is a correction factor for small photon energies E close to the absorption edge. The factor $[1 + F_{ns}(\beta)]$ represents a relativistic correction and the normalization coefficients $UN(E,Z)$ account for screening of the nucleus by the atomic electrons and for higher shell contributions. In eq. (10) α is the fine structure constant, mc^2 is the electron rest mass and r_e is the classical electron radius. The second factor in eq. (10) includes the *K*-shell binding energy ε_K which is approximated by

$$ \varepsilon_K = \frac{Z^2me^4}{2\hbar^2(4\pi\varepsilon_0)^2} = \frac{1}{2}(Z\alpha)^2(mc^2) \tag{11} $$

and

$$ n_1 = \left[\frac{\varepsilon_K}{(E - \varepsilon_K)}\right]^{1/2} \tag{12} $$

$$ f(n_1) = \frac{\exp(-4n_1\, cot^{-1}\, n_1)}{1 - \exp(-2\pi n_1)} \tag{13} $$

When $E < \varepsilon_K$ the energy is insufficient to remove a *K*-shell electron from the bound 1s state ($n = 1$) and the 1s contribution to the total cross section for the photoelectric effect vanishes. The relativistic correction factor for the 1s and 2s cross sections is parameterized by

$$ [1 + F_{ns}(\beta)] = 1 + 0.143\beta^2 + 1.667\beta^8 \tag{14} $$

where $\beta = v/c$ with v the velocity of the photoelectron.

For $1 \leq Z \leq 30$, $\varepsilon_K < 13$ keV and when only taking the Stobbe cross section for the 1s state into account, the missing *Z* dependence of the photoelectric cross section can be parameterized using an optimized normalization function

$$UN(E,Z) = \frac{{}_a\sigma^{ph}(E,Z)}{{}_a\sigma_{1s}^{ST}(E,Z)[1 + F_{ns}(\beta)]} \tag{15}$$

where ${}_a\sigma^{ph}(E,Z)$ represents the tabulated atomic cross sections for photoelectric absorption.

2.2.3.2 Scattering

For the combined atomic cross section for coherent and incoherent scattering, a parameterization is proposed by Jackson and Hawkes[43] of

$$\begin{aligned} &{}_a\sigma^{coh}(E,Z) + {}_a\sigma^{incoh}(E,Z) \\ &\qquad \simeq Z\ {}_e\sigma^{KN}(E) + (1 - f(Z)Z^{-1})\left[\left(\frac{Z}{Z_s}\right)^2 {}_a\sigma^{coh}(E_s,Z_s)\right] \end{aligned} \tag{16}$$

where ${}_e\sigma^{KN}(E)$ is the evaluated Klein-Nishina differential cross section, $f(Z) = Z^b$ with b equal to 0.50 and Z_s is a standard element used for scaling the coherent atomic cross sections as a function of a standard energy $E_s = (Z_s/Z)^{1/3}E$. The Klein-Nishina differential cross section evaluated over the solid angle equals

$$\begin{aligned} {}_e\sigma^{KN}(E) = 2\pi {r_e}^2 &\left\{\frac{1 + \delta}{\delta^2}\left[\frac{2(1 + \delta)}{1 + 2\delta} - \frac{1}{\delta} ln(1 + 2\delta)\right]\right. \\ &\left. + \frac{1}{2\delta} ln(1 + 2\delta) - \frac{(1 + 3\delta)}{(1 + 2\delta)^2}\right\} \end{aligned} \tag{17}$$

with $\delta = E/mc^2$.

2.2.4 **Fit functions for the parameterization of the electronic cross section**

For the electronic cross section for photoelectric absorption, the normalization coefficients UN in eq. (15) have been calculated using the tabulated values from XCOM (NIST)[44]. Values for the fundamental physical constants have been used from CODATA (NIST)[45]. The energy dependence of the calculated values for UN has been examined as a function of the energy and the atomic number by calculating the relative difference between UN data averaged over the energy range of 20 to 150 keV ($UN(Z)$) and UN data as a function of energy and atomic number ($UN(E,Z)$). This relative difference has been found to be smaller than $5\text{x}10^{-5}$ for energies between 20 and 150 keV and atomic numbers between 1 and 30. Therefore, only $UN(Z)$ data averaged over the energy range of 20 to 150 keV has been fitted as a function of Z. For this fit we used a five parameter function, which gives an accurate description of the relation between $UN(Z)$ and Z

$$UN(Z) = y_0 + a[1 - \exp(-bZ)] + c[1 - \exp(-dZ)] \tag{18}$$

with values for the fit parameters given in table 2.1 ($R^2 = 0.9994$). The averaged $UN(Z)$ data and the corresponding fit are given in figure 2.1a. The relative differences between fit and data are smaller than 0.5% for the elements H to Zn except for the elements He and Li showing slightly larger deviations but still less than 1.3%.

The atomic cross section for coherent scattering ${}_a\sigma^{coh}(E_s, Z_s)$ in eq. (16) has been evaluated for a standard element Z_s of 8 in order to accomplish a high accuracy of the model in the soft tissue region. The tabulated values for ${}_a\sigma^{coh}(E_s, 8)$[44] have been fitted as a function of the standard energy E_s using a best-fit seven parameter function

$${}_a\sigma^{coh}(E_s, 8) = f_0 + g\exp(-hE_s) + k\exp(-lE_s) + m\exp(-nE_s) \tag{19}$$

with values for the fit parameters given in table 2.2 ($R^2 = 0.9999$). Data values and corresponding values obtained with the fit function are presented in figure 2.1b. The relative differences are within 3.4% for energies between 20 and 150 keV.

The accuracy of the final parameterization of the total electronic cross section in eq. (9) has been analysed as a function of the energy and the atomic number by comparison with the tabulated data[44]. The difference between the calculated and tabulated values is shown in figure 2.2. For Z between 2 and 5 and for energies between 20 and 35 keV the largest differences, up to -1.9%, are found. However, differences for the biologically relevant elements (H, C, N, O, P, S and Ca[17]) are less than 0.7% for all energies above 20 keV.

Table 2.1. Fit parameters for the function in eq. (18) of normalization coefficients $UN(Z)$.

Fit parameter *UN*(*Z*)	Value
y_0	-0.0588
a	0.2266
b	0.0418
c	0.9771
d	0.8222

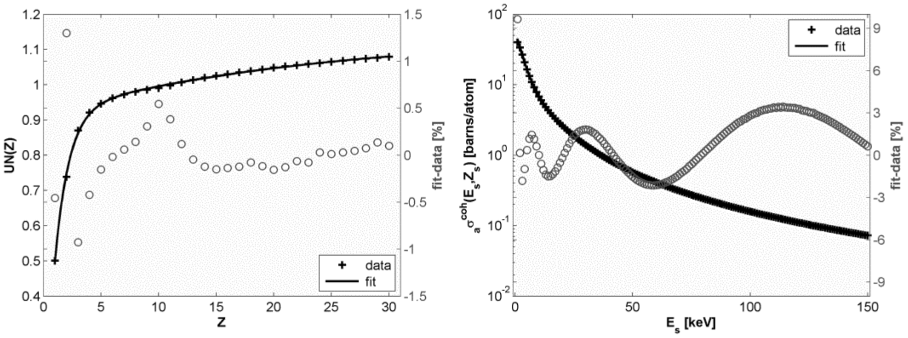

(a) (b)

Figure 2.1. (a) Normalization coefficients $UN(Z)$ averaged for energies between 20 and 150 keV and the corresponding fit obtained with the function in eq. (18). (b) Atomic cross sections for coherent scattering of oxygen (Z_s = 8) as a function of standard energies E_s and the corresponding fit to the data using the function in eq. (19). The circles represent the relative differences between the fit and the data.

Table 2.2. Fit parameters for the function in eq. (19) of the atomic cross sections for coherent scattering $_a\sigma^{coh}(E_s, Z_s)$ with Z_s = 8.

Fit parameter $_a\sigma^{coh}(E_s, Z_s = 8)$	Value
f_0	0.0191
g	8.9242
h	0.0781
k	0.9607
l	0.0192
m	47.605
n	0.3213

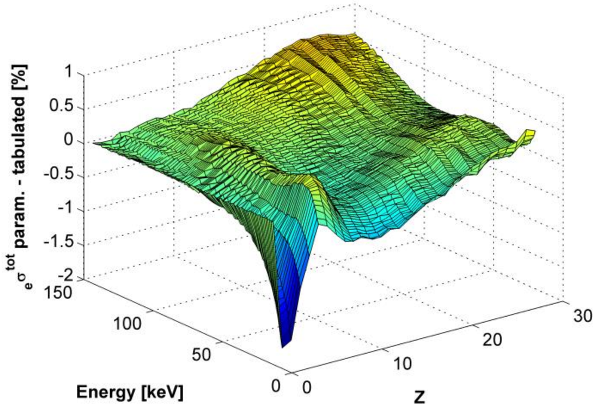

Figure 2.2. Relative difference between the model parameterization of the total electronic cross section and tabulated values[44] at energies of 20 to 150 keV for *Z* between 1 and 30.

2.3 Experimental methods

The experimental data for our DECT analysis has been acquired at tube potentials of 100 kV and 140 kV with additional 0.4 mm tin filtration (140 kV Sn) on a DSCT system (SOMATOM Definition Flash, Siemens Medical Solutions, Forchheim, Germany). The low kV setting was set to 100 kV in order to reduce beam hardening artefacts due to an aluminium insert in the phantom, which would be more pronounced at 80 kV images and degrade the DECT material characterization accuracy and image quality.

2.3.1 System weighting functions for 100 kV and 140 kV Sn DECT

In figure 2.3 system weighting functions for 100 kV ($j = 2$) and 140 kV Sn ($j = 1$) are shown, calculated with eq. (2) using the tube output spectra and detector responsivity provided by the manufacturer (Siemens Medical Solutions, Forchheim, Germany). These tube output spectra have been measured by the manufacturer using a scintillator crystal. The broadening in the characteristic x-ray peaks is due to the limited energy resolution of the crystal. The tube filtration present in the SOMATOM Definition Flash is 3 mm aluminium and 0.9 mm titanium. Using a Compton spectrometer, the spectra of the DSCT system employed for this study have been measured showing a good correspondence with the spectra provided by the manufacturer[46]. Notice that in the real CT spectrum the characteristic x-ray peaks are sharp lines. The edge in the SWF around 50 keV (figure 2.3) corresponds to the *K*-edge of gadolinium in the Gd_2O_2S scintillator CT detector.

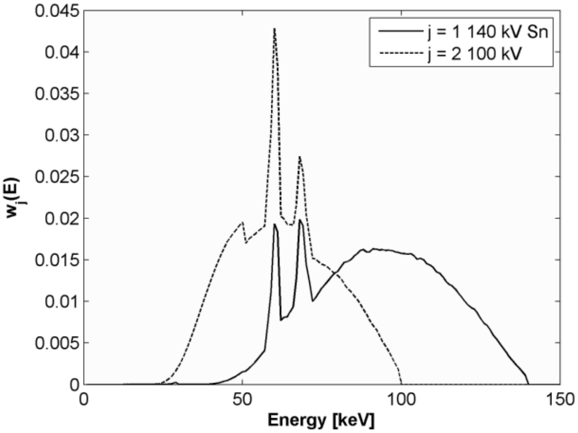

Figure 2.3. System weighting functions $w_j(E)$ per energy bin of 1 keV.

The spectral weighted accuracies of the final parameterization of the total electronic cross section in eq. (9) have been calculated for the 100 kV and 140 kV Sn setting. For atomic numbers *Z* between 1 and 30 and averaged over both the SWFs of 100 kV and 140 kV Sn, the relative difference between the model parameterization of the total electronic cross section and the tabulated data[44] is less than 0.3%.

2.3.2 Ratio function for solving the effective atomic number

In the iterative solution of eq. (8) for the effective atomic number Z', the *Z*-values are restricted between 1 and 30, the region for which the total cross section has been parameterized. As illustrated in figure 2.4, a particular ratio μ_1/μ_2 can be linked to a value for Z'. If a measured ratio exceeds the boundaries for which a value of Z' exists within the function, Z' was set to zero. These zeros are considered to be empty voxels in the image, and are mainly caused by noise and artefacts.

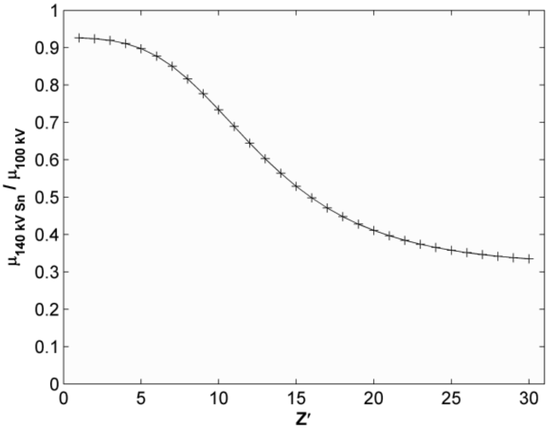

Figure 2.4. Ratio of the model calculated SWF weighted μ_j values versus the effective atomic number Z' in the model range of 1 to 30.

2.3.3 Phantom configuration

The accuracy of the results of the DECT method has been assessed with a 33 cm diameter Gammex 467 tissue characterization phantom (Gammex Inc., Middleton, WI, USA) (figure 2.5) using specifications of the materials listed in table 2.3. In addition to the standard phantom configuration with tissue substitutes, inserts made of certified therapy grade solid water (Gammex 457-CTG) and aluminium (AlMgSi1) have been measured. This, as a first order approximation to a more complex geometry with a metal implant where the influence of beam hardening and scatter are more pronounced due to the high *Z* and density of the metal.

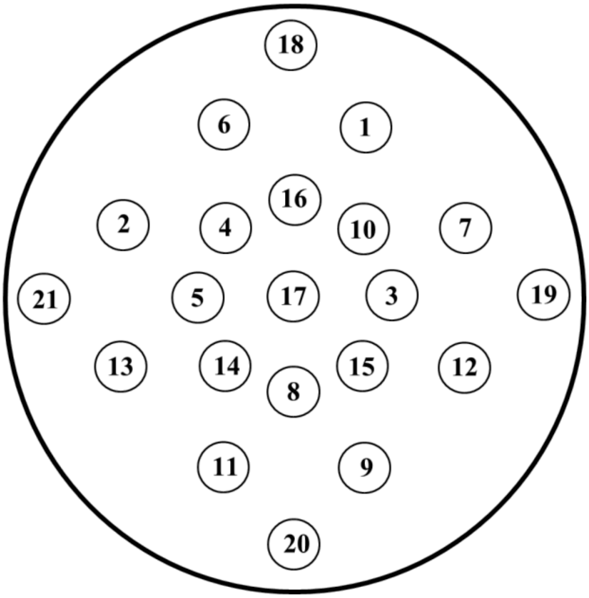

Figure 2.5. Configuration of the Gammex 467 tissue characterization phantom (Gammex Inc., Middleton, WI, USA). The numbered circles represent the regions of interest (ROIs) drawn in the inserts and phantom to assess the DECT method. The corresponding elemental compositions and relative electron densities of the materials are listed in table 2.3.

2.3.4 DECT measurement and analysis

The Gammex 467 tissue characterization phantom has been scanned in 100 kV / 140 kV Sn DECT spiral mode with a collimation of 32x0.6 mm. A clinical virtual noncontrast (VNC) abdomen liver protocol has been used with 230 mAs at 100 kV and 178 mAs at 140 kV Sn ($CTDI_{vol}$ = 17.9 mGy) to resemble clinical application. The data has been reconstructed in a 512x512 image matrix with a slice thickness of 1.0, 1.5, 3.0 and 5.0 mm with D20f (smooth) and D24f (bone beam hardening correction) filtered back projection (FBP) and Q30f strength 5 sinogram affirmed iterative reconstruction (SAFIRE) kernels for a field of view (FOV) of 35 cm. The variation in slice thickness enables examining the influence of quantum noise. For the conventional FBP reconstructed data a smooth D20f kernel has been applied which reduces the influence of noise with respect to sharp kernels. The ability of the D24f kernel to correct for beam hardening can be assessed from the data reconstructed accordingly. The more recently developed Q30f SAFIRE kernel provides noise reduction with respect to the FBP kernels.

Table 2.3. Elemental compositions (weight percentages) of the materials listed by their ROI number from figure 2.5 with corresponding calculated effective atomic numbers Z'_c, mass densities ρ and relative electron densities ρ_e^l/ρ_e^w.

ROI No.	Material	Z	1	6	7	8	12	13	14	15	17	20	25	Z'_c	ρ	$\rho_{e,l}/\rho_{e,w}$
		A	1.008	12.011	14.007	15.999	24.305	26.982	28.086	30.974	35.453	40.078	54.938		[gcm^{-3}]	
1	LN-300 lung		8.46	59.37	1.96	18.14	11.19	0	0.78	0	0.10	0	0	7.60	0.29	0.283
2	LN-450 lung		8.47	59.56	1.97	18.11	11.21	0	0.58	0	0.10	0	0	7.57	0.428	0.418
3	AP6 adipose		9.06	72.29	2.25	16.27	0	0	0	0	0.13	0	0	6.19	0.946	0.929
4	BR-12 breast		8.59	70.10	2.33	17.90	0	0	0	0	0.13	0.95	0	6.91	0.981	0.960
5	Water insert		11.19	0	0	88.81	0	0	0	0	0	0	0	7.47	0.998	1.000
6,8,17-21	CT solid water		8.00	67.29	2.39	19.87	0	0	0	0	0.14	2.31	0	7.72	1.014	0.987
7	Solid water M457		8.02	67.22	2.41	19.91	0	0	0	0	0.14	2.31	0	7.72	1.045	1.017
9	Aluminium AlMgSi1		0	0	0	0	1.0	97.2	1.0	0	0	0	0.8	13.25	2.691	2.341
10	BRN-SR2 brain		10.83	72.54	1.69	14.86	0	0	0	0	0.08	0	0	6.07	1.051	1.049
11	LV1 liver		8.06	67.01	2.47	20.01	0	0	0	0	0.14	2.31	0	7.72	1.095	1.066
12	IB3 inner bone		6.67	55.65	1.96	23.52	0	0	0	3.23	0.11	8.86	0	10.39	1.153	1.107
13	B200 bone mineral		6.65	55.51	1.98	23.64	0	0	0	3.24	0.11	8.87	0	10.40	1.159	1.113
14	CB2-30% $CaCO_3$		6.68	53.47	2.12	25.61	0	0	0	0	0.11	12.01	0	10.86	1.330	1.278
15	CB2-50% $CaCO_3$		4.77	41.62	1.52	31.99	0	0	0	0	0.08	20.02	0	12.49	1.560	1.473
16	SB3 cortical bone		3.41	31.41	1.84	36.50	0	0	0	0	0.04	26.81	0	13.59	1.823	1.699

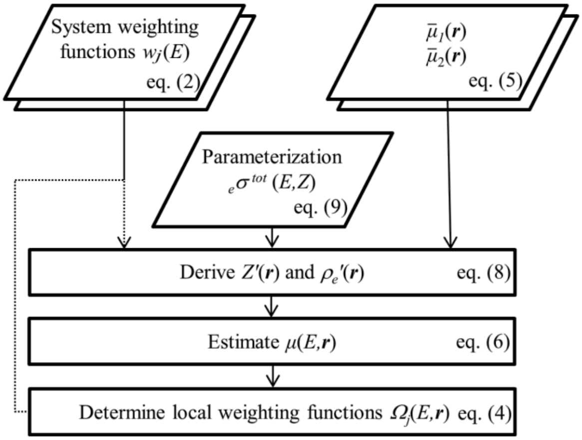

Figure 2.6. Iterative process to model the change in spectral energy distribution in the object. Initially, the parameterization of the total electronic cross section ${}_e\sigma^{tot}(E,Z)$ is weighted with the SWF to obtain values for $Z'(\boldsymbol{r})$ and $\rho_e'(\boldsymbol{r})$ using $\bar{\mu}_1(\boldsymbol{r})$ and $\bar{\mu}_2(\boldsymbol{r})$. A normalized LWF $\Omega_j(E,\boldsymbol{r})$ is determined from measured values $\bar{\mu}_j(\boldsymbol{r})$ and an estimation of $\mu(E,\boldsymbol{r})$ based on the parameterization of ${}_e\sigma^{tot}(E,Z)$ and determined values for $Z'(\boldsymbol{r})$ and $\rho_e'(\boldsymbol{r})$. This LWF replaces the SWF in the iterative process (dotted line) except for calculation of a new LWF.

The central slices of the reconstructed data sets of the phantom have been analysed using a commercially available software package (MATLAB 8.3, The MathWorks Inc., Natick, MA, USA). For the analysis, $\bar{\mu}_j$-images have been calculated from the CT images using eq. (5) and values for μ_w calculated from tabulated mass attenuation coefficients[44] multiplied with ρ_w = 0.998 [g cm^{-3}] (at 20°C) and weighted by the SWFs of 100 kV and 140 kV Sn, respectively. The two $\bar{\mu}_j$-images have been used as input for eq. (8) which has been numerically solved for Z' using the *fzero* function in MATLAB. Subsequently, the relative electron densities ρ_e'/ρ_e^w have been derived using the 140 kV Sn $\bar{\mu}_1$-image which is least sensitive to the error in Z' and suffers less from beam hardening and artefacts.

For the accuracy analysis of the method, regions of interest (ROIs) have been drawn at the locations indicated in figure 2.5 to calculate the mean and the standard deviation of the relevant parameters. Zero values have been excluded from the analysis to remove the ratios $\bar{\mu}_1(\boldsymbol{r})/\bar{\mu}_2(\boldsymbol{r})$ exceeding the boundaries of the model function. We define calculated values Z'_c by solving eq. (8) for Z' using calculated values for μ_1 and μ_2 based on the chemical composition and density of the respective material. For purpose of calculating μ_1 and μ_2, the electronic cross sections will be spectrally weighted by the SWFs for the initial analysis and the normalized LWFs in the iterative process.

2.3.5 Accounting for beam hardening using a local weighting function

An iterative process employing a voxel-based normalized LWF (eq. (4)) has been developed as illustrated in figure 2.6.

The LWF accounts for the energy distribution at position $\boldsymbol{r}$ in the image (figure 2.7). This affects the estimate of the calculated effective atomic number $Z'_c(\boldsymbol{r})$, which is used to compare with the $Z'(\boldsymbol{r})$ values derived from the data. To reduce the calculation time for Z'_c in the iterative process, eq. (8) was solved for Z'_c with LWFs and calculated values for μ_1 and μ_2 averaged over the ROI. The calculated effective atomic number Z'_c is recalculated with each iteration of the LWF as explained in section 2.3.4.

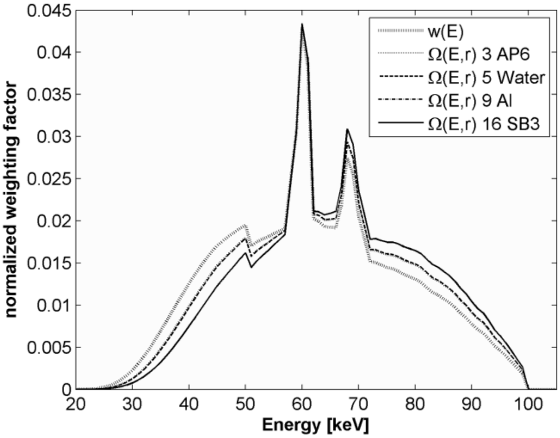

Figure 2.7. SWF $w_2(E)$ and normalized LWFs $\Omega_2(E,\boldsymbol{r})$ in the central voxel of sample materials within the phantom after the initial results for Z' and ρ'_e. Enhanced spectral hardening is visible for the aluminium and SB3 cortical bone insert (curves overlap) and for the AP6 adipose and water inserts (curves nearly overlap).

2.4 Results and discussion

2.4.1 Determination of effective atomic numbers and relative electron densities

2.4.1.1 Number of iterations LWF

The iteratively reconstructed DECT data with a slice thickness of 5.0 mm has been used for testing the DECT method employing the LWF to determine an estimate of the optimal number of iterations. This estimate has been verified throughout the analysis of all data. Relative differences between measured linear attenuation coefficients $\bar{\mu}_2$ and energy weighted (SWF and LWF) values calculated from tabulated data[44] are presented in figure 2.8. The results for $\bar{\mu}_1$ show a similar tendency but the relative differences are smaller (3 to -10%). After three iterations the values have converged within 0.05%. The values for strong absorbers like the bone substitutes and aluminium change only slightly with a fourth iteration. In figure 2.9a results for the measured effective atomic numbers Z' are presented. These results of Z' reflect the deviations in $\bar{\mu}_1$ and $\bar{\mu}_2$. The differences between the measured relative electron densities ρ_e'/ρ_e^w and the calculated values are represented in table 2.4 and figure 2.9b. After three iterations of the LWF the measured values deviate -1.3 to 1.0% from the calculated values except for aluminium, for which a relative difference of 2.3% has been found. Note that the standard deviation in the measured data is practically constant with increasing number of iterations, indicating that noise amplification by the iteration process is negligible.

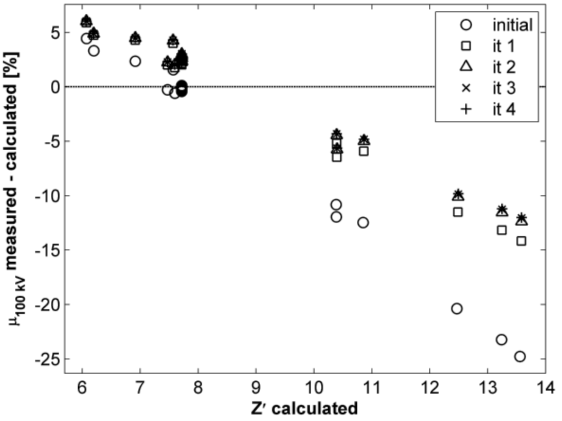

Figure 2.8. Relative difference between the linear attenuation coefficients $\bar{\mu}_2$ (100 kV) measured from iteratively reconstructed DECT at 5.0 mm and the calculated values μ_2. The differences are given for the initial analysis and after iteration one to four of the LWF.

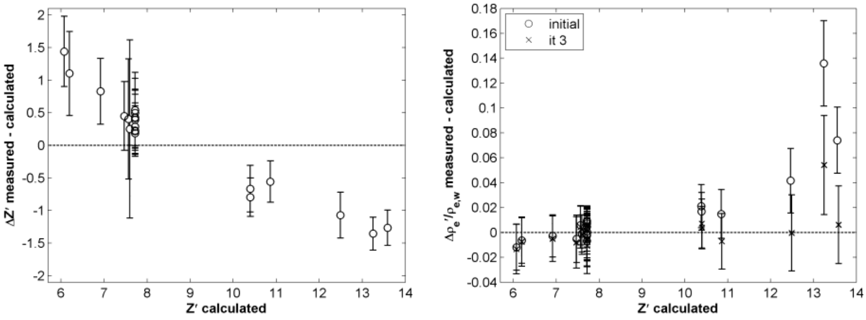

(a) (b)

Figure 2.9. Difference between (a) the effective atomic numbers Z' and the calculated values Z'_c and (b) the relative electron densities ρ_e'/ρ_e^w and the calculated values ρ_e^l/ρ_e^w. Values for Z' and ρ_e'/ρ_e^w have been determined from iteratively reconstructed DECT at 5.0 mm. The differences for Z' are given after three iterations of the LWF and the differences for ρ_e'/ρ_e^w are given for the initial analysis and after three iterations of the LWF. The error bars represent the standard deviation in the measured values.

2.4.1.2 Slice thickness

We examined the influence of the slice thickness on the accuracy and precision in the results of the DECT method using three iterations of the LWF. For this, iteratively reconstructed DECT data with slice thicknesses of 1.0, 1.5, 3.0 and 5.0 mm has been analysed. Figure 2.10 shows the effective atomic number Z' images determined at slice thicknesses of 1.0 and 5.0 mm. In figure 2.11, the relative electron density ρ_e'/ρ_e^w images for the different slice thicknesses are displayed. The analysis of the results is shown in figure 2.12 and table 2.4. The standard deviation in the measured relative electron density data increases on average by a factor of 1.8 by reducing the slice thickness from 5.0 to 1.0 mm. The accuracy in the measured relative electron density data for 1.0 mm slice thickness is better than 1.0% except for aluminium and LN-300. The aluminium insert causes beam hardening, scatter and associated artefacts which explain its different behaviour as compared to the other materials. LN-300 (top right insert) is an inhomogeneous porous material, which encloses air in the material structure. The measured linear attenuation coefficients $\bar{\mu}_j$ of air are very small for both kV settings, restricting these ratios $\bar{\mu}_1/\bar{\mu}_2$ to solve for an effective atomic number Z' and electron density ρ_e'. Comparing figures 2.10a and 2.10b shows that in the data for the LN-300 insert more empty voxels are present at 1.0 mm slice thickness than at 5.0 mm slice thickness. For 5.0 mm slices, the measured attenuation values are averaged over a larger volume. Consequently, the deviation for LN-300 is smaller than 1.0% as shown in table 2.4. Moreover, noise decreases when reconstructing at a larger slice thickness. This reduces the number of empty voxels in the image due to ratios $\bar{\mu}_1/\bar{\mu}_2$ exceeding the boundaries of the model function, as visible in figure 2.11.

Table 2.4. Relative difference between the relative electron densities ρ_e'/ρ_e^w measured from iteratively reconstructed DECT and the calculated values ρ_e^l/ρ_e^w. The differences are given as a function of slice thickness after three iterations of the LWF.

ROI No.	Material	$\rho_e'/\rho_{e,w\ \mathrm{it3,1.0mm}}$ difference [%]	$\rho_e'/\rho_{e,w\ \mathrm{it3,1.5mm}}$ difference [%]	$\rho_e'/\rho_{e,w\ \mathrm{it3,3.0mm}}$ difference [%]	$\rho_e'/\rho_{e,w\ \mathrm{it3,5.0mm}}$ difference [%]
1	LN-300 lung	-2.69	-1.63	-1.68	-0.65
2	LN-450 lung	0.50	1.05	0.66	1.03
3	AP6 adipose	-0.35	-0.23	-0.47	-0.80
4	BR-12 breast	-0.53	-0.47	-0.46	-0.53
5	Water insert	-0.48	-0.30	-0.44	-0.81
6	CT solid water	-0.48	-0.55	-0.31	-0.29
7	Solid water M457	-0.62	-0.72	-0.65	-0.52
8	CT solid water	-0.24	-0.37	-0.40	-0.64
9	Aluminium AlMgSi1	3.16	3.28	2.98	2.31
10	BRN-SR2 brain	-0.99	-1.04	-1.12	-1.28
11	LV1 liver	-0.33	-0.18	-0.41	-0.46
12	IB3 inner bone	0.54	0.62	0.56	0.64
13	B200 bone mineral	0.66	0.58	0.40	0.35
14	CB2-30% $CaCO_3$	-0.28	-0.28	-0.41	-0.56
15	CB2-50% $CaCO_3$	0.16	0.15	0.19	-0.03
16	SB3 cortical bone	0.58	0.67	0.72	0.36
17	CT solid water phantom	-0.96	-1.18	-1.10	-1.11
18	CT solid water phantom	-0.14	-0.14	0.11	0.16
19	CT solid water phantom	0.82	0.89	0.87	0.67
20	CT solid water phantom	0.57	0.51	0.54	0.57
21	CT solid water phantom	0.46	0.51	0.51	0.44

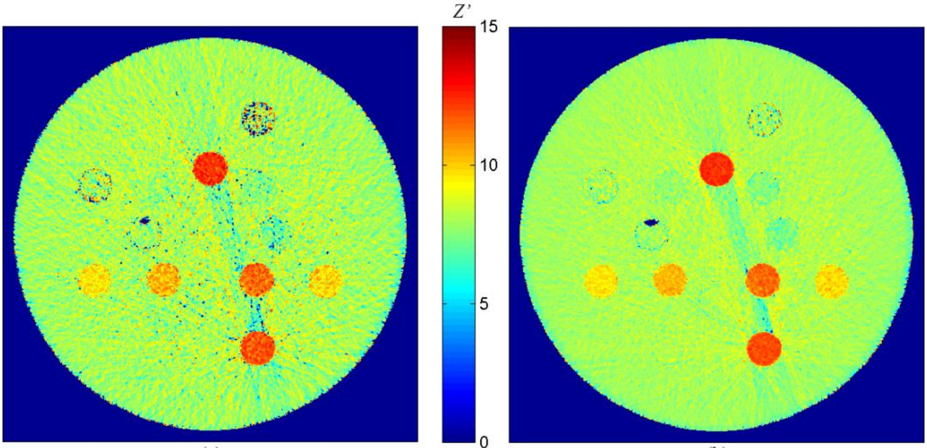

(a) (b)

Figure 2.10. Effective atomic numbers Z' determined from iteratively reconstructed DECT with a slice thickness of (a) 1.0 mm and (b) 5.0 mm.

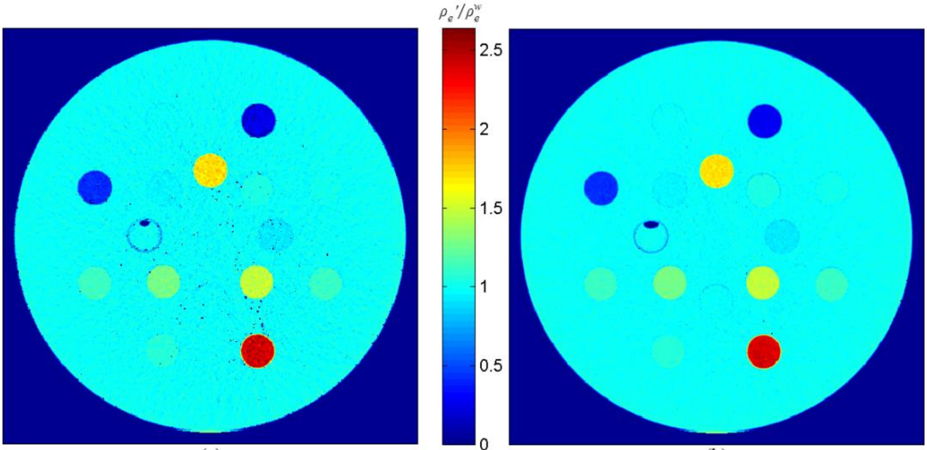

(a) (b)

Figure 2.11. Relative electron densities $\rho_e{}'/\rho_e^w$ determined from iteratively reconstructed DECT with a slice thickness of (a) 1.0 mm and (b) 5.0 mm.

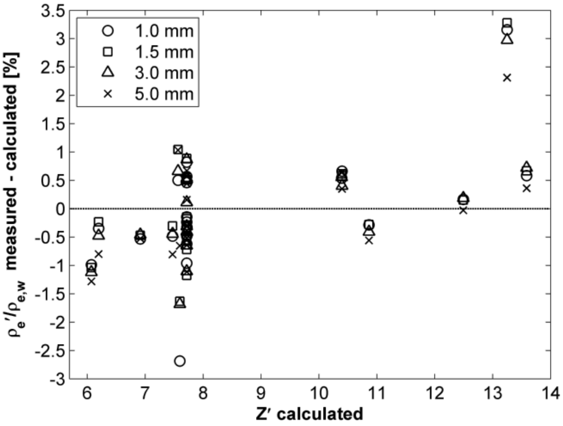

Figure 2.12. Relative difference between the relative electron densities ρ_e'/ρ_e^w measured from iteratively reconstructed DECT and the calculated values ρ_e^l/ρ_e^w. The differences are given as a function of slice thickness after three iterations of the LWF.

2.4.1.3 Reconstruction kernel

The iteratively reconstructed DECT data using a Q30f strength 5 SAFIRE kernel has been compared with D20f and D24f FBP kernels for a slice thickness of 1.0 mm. The standard deviation in the measured CT numbers increases for the FBP kernels, with on average 13 HU for the D20f kernel. In the data reconstructed with a D24f kernel, the measured CT numbers as well as the standard deviations are altered. The D24f kernel applies a bone beam hardening correction increasing the CT numbers of e.g. SB3 cortical bone and aluminium by 120 HU and 238 HU, respectively at 100 kV. Consequently, the relative difference between the measured linear attenuation coefficients and the calculated values reduces from -12 to -7% for SB3 cortical bone and from -11 to -4% for aluminium, after three iterations of the LWF. Correspondingly, the deviation for the measured effective atomic numbers Z' reduces from -1.3 to -0.7 and from -1.5 to -0.6 in units of Z'. The results for the accuracy of the measured relative electron densities ρ_e'/ρ_e^w after three iterations of the LWF are presented in figure 2.13. For most materials, FBP reconstructed data have a lower accuracy than SAFIRE data with the extreme case of LN-300 (relative difference of 7.4% for D24f). The values for SB3 cortical bone and aluminium become slightly more accurate when using a D24f kernel due to the additional beam hardening correction. The standard deviation in the measured relative electron densities ρ_e'/ρ_e^w increases on average by a factor of 1.7 when reconstructing with FBP. This corresponds to the increase in standard deviation in the measured CT numbers. Evaluation of the relative electron density images shows that the image quality is degraded for FBP reconstructed data with more empty voxels, mainly due to the increase in noise level.

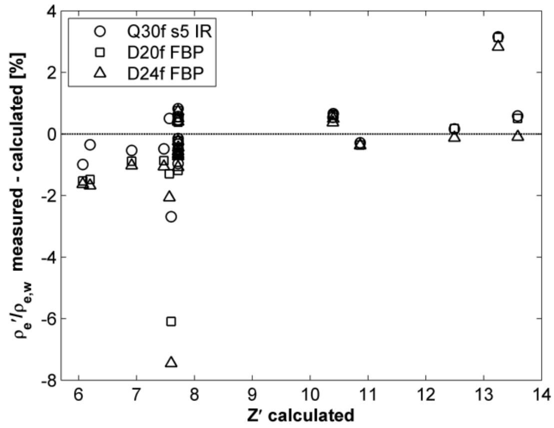

Figure 2.13. Relative difference between the relative electron densities ρ_e'/ρ_e^w measured from data reconstructed with Q30f strength 5 SAFIRE, D20f and D24f FBP and the calculated values ρ_e^l/ρ_e^w. The data is reconstructed with a slice thickness of 1.0 mm and compared for three iterations of the LWF.

2.4.2 Spectral weighting and beam hardening

The lowest energies in the spectral distribution and elements with high atomic numbers show a large Z dependence in photon interactions because of the dominant photoelectric effect. This implies that the low energy part of the spectrum contributes more to the effective atomic number Z', where high Z elements primarily determine its value. In the high energy part, incoherent scattering dominates and the high kV spectrum therefore has a smaller impact on the effective atomic number than the low kV spectrum. For materials with a Z'_c smaller than water (adipose, breast and brain), positive deviations are found for $\bar{\mu}_2$ as well as Z' (figure 2.8, figure 2.9a). The materials with a Z'_c larger than solid water exhibit negative deviations from calculated values of $\bar{\mu}_1$, $\bar{\mu}_2$ and Z'. Analysis of the measured values for $\bar{\mu}_j$ suggests that the source of this deviation lies in the reconstructed CT images. The water beam hardening correction applied for Q30f reconstructed data includes an artificial correction of all raw attenuation data, producing a flat CT number profile in a homogeneous water phantom. If water is partly replaced by bone, more low energy photons are absorbed and the average photon energy increases thereby decreasing the measured attenuation coefficient of bone. To adequately compensate for this increase in average photon energy, the measured attenuation coefficients and corresponding CT numbers should be increased. For materials with a Z'_c smaller than water the average photon energy decreases and the measured attenuation coefficients should be reduced. However these corrections are not applied in the reconstruction process and may explain the deviations found. This implementation of the LWF can only correct for the energy distribution as far as it can be deduced from the measured CT numbers in the reconstructed image.

The tendency in the relative differences found for the effective atomic numbers appears in a weakened form and in reverse in the measured relative electron densities. The electron density is derived from the ratio of the measured linear attenuation coefficient at 140 kV Sn, $\bar{\mu}_1$ and the total electronic cross section as a function of the determined effective atomic number Z'. The relative differences of both quantities $\bar{\mu}_1$ and Z' mainly average out in this operation.

An accurate parameterization of the total electronic cross section is required to determine the electron density and effective atomic number at sub percent level. Where a systematic error of 1% of the total electronic cross section in the nominator and denominator of eq. (8) divides out by solving for Z', it gives rise to a -1% error in the determined electron density and vice-versa. However, since the spectrally weighted errors of the total electronic cross section are different in the nominator and denominator of eq. (8) they will also affect the accuracy of Z'. In this study, the spectrally weighted errors have been determined to be less than 0.3% and are therefore expected to account for less than 0.3% in the error of the determined electron density.

2.4.3 Considerations for clinical application

We have assessed a complex geometry with a metal insert where some empty voxels were created in the relative electron density images due to noise, scatter and beam hardening artefacts. In addition to this, we have also measured the default configuration of the Gammex 467 phantom with exclusively tissue substitutes. The relative electron density images for this geometry show considerably less empty voxels in the phantom at a high resolution of 1.0 mm slice thickness than the analysis with aluminium. This indicates that a significant improvement of image quality can be achieved in clinical cases without metals involved. The influence of noise can be restricted by increasing the mAs, at the expense of higher patient dose, to improve counting statistics. In case empty voxels appear, interpolation techniques can be applied to assign the most probable value. The relative electron density of air can be assigned to empty voxels due to air using a certain threshold for $\bar{\mu}_j$. When increasing the slice thickness from 1.0 mm to 5.0 mm, the standard deviation in the measured relative electron densities reduces on average by a factor of about 1.8. The accuracy of the measured values however is hardly affected by the slice thickness used for reconstruction. The choice for a particular slice thickness is a trade-off between resolution and precision of the relative electron densities. Imaging for treatment planning of cranial and lung tumours can require 1.0 mm slice thickness in order to provide sufficient resolution at air-bone interfaces. It might also be possible to rebin the data to smaller slices after deriving relative electron density images from a higher reconstructed slice thickness.

Rayleigh and Compton scattering in a phantom deflect the incident photons from the beam and are included in the parameterization of the total cross section. Small angle deflected photons are assumed to be absorbed in the anti-scatter grids. A DSCT system gives rise to phantom scattered photons which can be detected in the detector about 90 degrees offset from the tube. This scattered radiation is corrected by the manufacturer using dedicated correction algorithms[47].

For DECT with tube potentials of 80 kV combined with 140 kV Sn, the ratio function of model calculated μ_j values versus effective atomic numbers Z' (as in figure 2.4) is steeper. Consequently, the value for Z' is less sensitive to small variations in the ratio of measured values for $\bar{\mu}_j$. On the other hand, 80 kV data is more sensitive to beam hardening and induced artefacts. In geometries where the influence of beam hardening is expected to be limited, 80 kV / 140 kV Sn DECT can potentially provide improved accuracy and image quality with respect to 100 kV / 140 kV Sn DECT.

2.4.4 Modification of the method for high Z materials and different tube potentials

Besides our implementation, the described method can be optimized for a high atomic number *Z* e.g. iodine, to enable analysis of patient imaging data using iodine contrast agent. In CT imaging for dose calculation in radiotherapy treatment planning, contrast agents are generally avoided unless incorporated during treatment. To account for the use of implant materials like gold markers it would be more convenient to assign known electron density information from specifications to the voxels involved using a threshold method. If the DECT method described will be optimized for a high *Z*, a more accurate description of the electron binding energy should be implemented to correctly position the *K*-edges which are then included in the relevant energy range. The method can easily be extended for higher energies e.g. 200 kV if DECT with a larger energy separation becomes available.

2.4.5 Other studies

Using monochromatic dual energy x-ray CT in an experimental setup, Torikoshi *et al.*[21] measured electron densities with accuracy better than 2.7% in a small phantom for a set of tissue substitutes and K_2HPO_4 solutions. Bazalova *et al.*[37] modified the method from Torikoshi *et al.* for polychromatic x-ray CT and assessed it on a single slice CT scanner using a Gammex electron density phantom. Initially they accounted for beam hardening in the phantom by filtering the spectra for the algorithm with the amount of solid water corresponding to the radius of the phantom. After they obtained the measured relative electron densities, they corrected their data for additional beam hardening using a semi-empirical fit. Using this method, relative electron densities were derived with accuracy better than 6%. From a simulation study, Landry *et al.*[48] reported an algorithmic accuracy of the relative electron densities better than 8% on a similar phantom. Later on, Landry *et al.*[49] measured a Gammex 465 phantom on a dual source CT scanner at 80 / 140 kV Sn tube potentials with exposures of 900 and 348 mAs. Thereafter they averaged three slices (each reconstructed with a slice thickness of 3 mm) and resampled the 512x512 image matrices to 256x256 to reduce image noise. With this approach they reported relative electron densities with accuracy within 2.5% except for AP6 adipose for which a deviation of almost 6% was found. Saito[41] presented a linear relationship between the energy-subtracted CT number and the relative electron density using a fitting procedure to determine a scanner specific weighting factor. Using this calibration method and the DECT data measured by Landry *et al.*[49] they determined relative electron densities differing up to 7.6% from calculated values.

We have determined relative electron densities within an accuracy of 1% for all tissue substitutes inside a Gammex tissue characterization phantom which included a metal insert. With these results we provide a bridge towards clinical application of DECT for radiotherapy and particle therapy treatment planning.

2.4.6 Applicability

Apart from fitting fundamental quantities like the normalization coefficients $UN(Z)$ and the atomic cross section for coherent scattering ${}_{a}\sigma^{coh}(E_s, Z_s)$, our method is based on the fundamental physics of photon interactions with matter and requires neither a phantom nor a system specific calibration method. The method described in this paper does not require an empirical beam hardening correction on the determined relative electron densities because the beam hardening as included in the CT reconstruction process is well modelled in the iteration process. Only information on x-ray spectra and detector efficiency are necessary, which are available from the manufacturer. The x-ray spectra for a particular CT system can be measured using a Compton spectrometer[46] in order to include system specific spectra in the SWF and assure the quality of the CT system used for treatment planning. The calculation time for a 512x512 image matrix in MATLAB including an initial determination of the effective atomic numbers and electron densities, calculation of the LWFs and iterations 1 to 4 of previous processes is approximately 15 hours on a regular PC. The most computational intensive procedure in this method is iteratively solving for Z' which requires about 2 hours per iteration step.

2.4.7 Effective atomic number and mean excitation energy

To calculate stopping powers from the Bethe-Bloch equation the relative electron density and the mean excitation energy are needed as input. Schneider *et al.*[34] showed for some tissue substitutes that a variation of 10% in the mean excitation energy alters the relative proton stopping power with less than 1.5%. In a study of Yang *et al.*[30] this is confirmed for calculated relative proton stopping powers of human tissues. Yang *et al.*[23] proposed a relation between the effective atomic number and the logarithm of the mean excitation energy based on calculations. This relation, however, requires a priori knowledge of the type of tissue. The experimental results on the effective atomic number we present in this study suffer from a systematic deviation, which we think is due to the beam hardening correction in the CT reconstruction process. Future research will focus on deriving an accurate relation between the effective atomic number and the mean excitation energy needed for dose calculations in proton therapy.

2.5 Conclusion

We have developed, described and assessed a DECT method which is based on an accurate parameterization of the total cross section proposed by Jackson and Hawkes[43]. Using this parameterization which we extended for practical application and our implementation of a local weighting function proposed by Heismann and Balda[32], we derived relative electron densities with accuracy better than 1% for all tissue substitutes in a large tissue characterization phantom. Based on this accuracy we conclude that the proposed method is suitable for accurate electron density determination for radiotherapy and especially particle therapy treatment planning.

Patient specific proton stopping powers from dual energy CT: analysis method and experimental validation

Abstract

The advantage of the high conformity that can be achieved with protons is among other effects limited by range uncertainties. These partly arise from the translation of CT data to proton stopping powers. In this study we describe and validate a method to calculate relative stopping powers (RSPs) through the electron densities and effective atomic numbers, determined from dual energy computed tomography (DECT) images.

A relation between the effective atomic number and logarithm of the mean excitation energy has been established based on various materials and the average tissues described by Woodard and White. Using the electron density and mean excitation energy derived from the DECT data, energy dependent RSPs have been calculated. Geant4 depth dose simulations have been performed to obtain simulated RSPs. The DECT predicted and Geant4 simulated RSPs have been compared to experimental RSPs for 32 materials. The experimental RSPs have been measured at a proton energy of 149 MeV and for selected materials also at 89 and 62 MeV.

With DECT electron densities have been determined with accuracy better than 1% for 29 of the 32 materials. Depth dose profiles of 190 MeV (initial energy) protons in water have been measured with reproducibility < 0.03 mm. Experimental RSPs have been determined with an uncertainty < 0.4%. The DECT predicted RSPs are for most materials within 2% of the experimental RSPs. Geant4 simulations show comparable deviations from the experimental values.

The presented method provides patient specific tissue RSPs and can potentially reduce the range uncertainty in proton therapy treatment planning.

3.1 Introduction

More accurate proton stopping power estimation can reduce the uncertainty in proton dose distributions in clinical practice. For dose calculation, relative proton stopping powers (RSPs) are derived from computed tomography (CT) data of a patient. Currently applied single energy CT (SECT) methods estimate the RSP based on a calibration measurement with tissue substitutes or a stoichiometric calibration using average tissue compositions and densities[17,18,34,39]. The range uncertainty in using the stoichiometric calibration method is estimated by Schaffner and Pedroni[18] at 1.8% for bone and 1.1% for soft tissue. However, the variety in tissue compositions and densities between individuals[17] imposes an important restriction on the patient specificity of the stoichiometric calibration method. In a theoretical study, Yang *et al.*[23] described a dual energy CT (DECT) based prediction of RSPs with a better robustness for variations in tissue compositions and densities.

Prediction of proton stopping powers using the Bethe-Bloch formalism requires accurate estimates of the electron density and mean excitation energy of the tissues in the beam path. High accuracy (in the order of 1%) electron densities can be derived from DECT images[50-52]. The mean excitation energy $\langle I \rangle$ is often obtained by relating the DECT parameter effective atomic number (Z') to $\ln\langle I \rangle$. Yang *et al.*[23] derived linear parameterizations for $\ln\langle I \rangle$ in Z' based on the average tissues described by ICRU report 44[53] and White *et al.*[39]. Bourque *et al.*[54] derived a three segment high order polynomial relation in Z' based only on the average tissues. The method of Yang *et al.*[23] has been adopted by Hünemohr *et al.*[52]. However, in their following work Hünemohr *et al.*[55] showed that this method is less accurate when applied to materials that differ from the average tissues. Therefore a more general valid method is desired which is accurate for arbitrary materials.

The RSP is energy dependent; some analytical dose calculation algorithms use a direct translation from a CT image to a RSP image independent of the beam energy at the position of the tissue. Moyers *et al.*[56] measured proton RSPs for 22 materials at energies of 135, 175 and 225 MeV and compared the RSPs with literature values and calculations. From these measurements they estimated the energy dependence of the RSP for energies between 135 and 225 MeV to be < 1.2% for soft tissues.

In this work we propose a new relation between Z' determined from DECT and the logarithm of the mean excitation energy $\ln\langle I \rangle$. Combined with the DECT determined electron density, this relation enables calculation of RSPs from patient CT imaging. Since there is increasing interest in the use of TOPAS (a Geant4 based package)[57] for treatment planning and quality assurance in proton therapy[16] RSPs have also been predicted with Geant4[58] Monte Carlo depth dose simulations. To assess the accuracy of both the proposed DECT method and Geant4 Monte Carlo simulations for RSP prediction, the results obtained from DECT and Geant4 simulations have been verified experimentally for 32 materials. In addition, the energy dependence of the RSP has been experimentally explored.

3.2 Theory

3.2.1 Relative stopping power and water equivalent thickness

The electronic stopping power of a material can be approximated with an estimated accuracy of 1-1.5%[59,60] for clinically relevant energies and materials by

$$S = -\frac{\mathrm{d}E}{\mathrm{d}x} = \frac{4\pi r_e^2 m_e c^2}{\beta^2}\rho_e\left(f(\beta) - \ln\langle I\rangle\right) \tag{1}$$

where r_e is the classical electron radius, $m_e c^2$ is the electron rest mass with c the speed of light in vacuum and $\beta = v/c$ with v the proton velocity. The electron density of the target material ρ_e equals $N_A \rho\, Z/A$ with mass density ρ, Avogadro's number N_A, atomic number Z and atomic weight A. $f(\beta)$ is defined as

$$f(\beta) = \ln\left(\frac{2m_e c^2\beta^2}{1-\beta^2}\right) - \beta^2 \tag{2}$$

The Bragg additivity rule states that the mass stopping power S/ρ of a mixture or compound can be approximated by the weighted addition of the mass stopping power of the elements[61]. In this approximation the mean excitation energy $\ln\langle I\rangle$ of a compound is given by

$$\ln\langle I\rangle = \frac{\sum_k \omega_k \frac{Z_k}{A_k}\ln\langle I_k\rangle}{\sum_k \omega_k \frac{Z_k}{A_k}} \tag{3}$$

with the mass fraction ω_k and mean excitation energy $\langle I_k\rangle$ of element k in the compound.

The electronic stopping power relative to water (relative stopping power, RSP) follows as

$$\frac{S_m}{S_w} = \frac{\rho_e^m}{\rho_e^w}\left(\frac{f(\beta) - \ln\langle I_m\rangle}{f(\beta) - \ln\langle I_w\rangle}\right) \tag{4}$$

in which the relative electron density, ρ_e^m/ρ_e^w and the mean excitation energy of the material, $\ln\langle I_m\rangle$ are the parameters that depend on the target material.

The water equivalent thickness (WET) of a target material is specified as the thickness of water t_w that results in the same energy loss as that due to the considered material with thickness t_m (figure 3.1) and is defined as[62]

$$t_w = t_m \frac{\bar{S}_m}{\bar{S}_w} \tag{5}$$

where the average linear stopping power $\bar{S}$ between the entrance and exit of the target material is defined as

$$\bar{S} = \frac{\int_E S \,\mathrm{d}E}{\int_E \mathrm{d}E} \tag{6}$$

From WET measurements, water equivalent ratio (WER, t_w/t_m) values can be determined which we consider as the stopping power of a material relative to water (RSP).

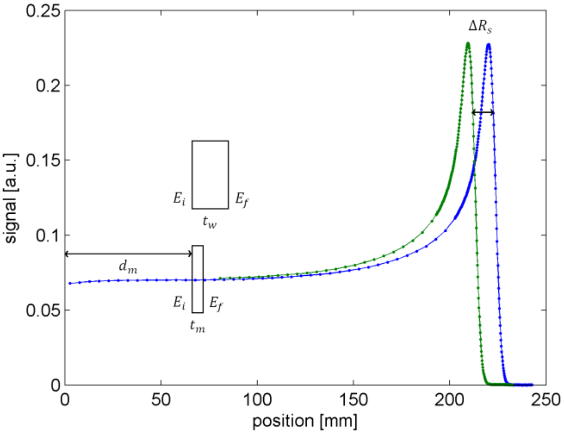

Figure 3.1. Concept of the water equivalent thickness t_w (WET) derived from the measured range difference ΔR_s and the material thickness t_m. ΔR_s is the difference in $R_{80\%}$ (distal 80% of the dose) between the measurement in water only (blue) and the measurement with a material positioned at depth d_m in the water (green). t_w is the thickness of water that results in the same energy loss ($E_f - E_i$) as in the material with thickness t_m.

The range of protons with kinetic energy E_k is equal to

$$R(E_k) = \int_0^{E_k} \left(-\frac{\mathrm{d}E}{\mathrm{d}x}\right)^{-1} \mathrm{d}E \tag{7}$$

The range difference due to the sample in water, ΔR_s, is given by

$$\Delta R_s = t_m - t_w = t_m - \int_{E_f}^{E_i} \left(-\frac{\mathrm{d}E}{\mathrm{d}x}\right)_w^{-1} \mathrm{d}E \tag{8}$$

with E_i the (initial) kinetic energy of the protons at the entrance and E_f the (final) kinetic energy of the protons at the exit of the target material. The thickness of the sample can be expressed as

$$t_m = \int_{E_f}^{E_i} \left(-\frac{\mathrm{d}E}{\mathrm{d}x}\right)_m^{-1} \mathrm{d}E \tag{9}$$

The initial kinetic energy of the protons E_i can be determined from the measured range in water

$$R_w(E_i) = \int_0^{E_i} \left(-\frac{\mathrm{d}E}{\mathrm{d}x}\right)_w^{-1} \mathrm{d}E \tag{10}$$

where $R_w(E_i)$ is the range in water for protons that have an initial kinetic energy E_i and

$$R_w(E_i) = R(E_k) - d_m \tag{11}$$

with d_m the depth at which the material is placed in the water (figure 3.1), and $R(E_k)$ the measured range in water of protons with energy E_k.

3.2.2 Electron densities and effective atomic numbers from DECT

Effective atomic numbers and electron densities have been derived from DECT images using the method described by van Abbema *et al.*[51] (chapter 2). This includes a CT system description in terms of photon spectra and detector efficiency (system weighting function, SWF) which is used to spectrally weigh the physics based parameterization of the electronic cross section. An effective atomic number can be derived using eq. (8) in ref. 51. This equation relates the ratio of the two measured linear attenuation coefficients to the ratio of the spectrally weighted parameterizations of the electronic cross section and can be solved numerically for Z'. Using this effective atomic number Z' and one measured linear attenuation coefficient an electron density $\rho_e{}'$ and relative electron density $\rho_e{}'/\rho_e^w$ can be determined. The electron density is preferably derived from the high kV data because the electronic cross section is then dominated by Compton scattering, which is only weakly dependent on Z and photon energy. A normalized local weighting function (LWF), defined by Heismann and Balda[32], is integrated in the analysis[51] to spectrally weigh the parameterization of the electronic cross section by a spectral distribution specific for each position in the object. In this way, the LWF is included in the determination of the effective atomic number and electron density. This is an image based iterative method which generally converges after 3 iterations of the LWF. The shape of the LWF is determined by the SWF and by the attenuation coefficient of the material (ref. 51 figure 7)[32].

3.3 Materials and Methods

DECT and stopping power measurements have been made for a set of materials covering the clinically relevant range of densities and effective atomic numbers Z'. The characteristics of these materials when irradiated with photons and protons have been measured on a dual source CT system (SOMATOM Force, Siemens Medical Solutions, Forchheim, Germany) and with 190 MeV (nominal) protons at the AGOR Facility for IRradiation of Materials (AGORFIRM)[63]. In addition, Geant4 Monte Carlo simulations[58] of the interactions of protons and proton induced particles with the materials have been performed. A comparison in which the measured RSPs are used as the ground truth values will provide an estimate of the accuracy of stopping power predictions based on the DECT method and Geant4 Monte Carlo simulations, respectively.

3.3.1 Specifications of the selected materials

An overview of the 32 selected sample materials and their composition and density is given in table 3.1. Material numbers 1-6 are ‘tissue equivalent’ Gammex (Gammex Inc., Middleton, WI, USA) materials with specified compositions. The analytical standards (No. 7-15, 17 and 18) have been selected based on their high purity and well specified composition. Silicone oil (No. 19) is a material used as a tamponade after vitrectomy in treatment of ocular tumours. Potassium chloride solutions (No. 20-23) have been prepared to cover the intermediate Z' range. In addition, different polymers (No. 25-30) aluminium and carbon have been selected. Al_2O_3 (No. 32) is a ceramic used in prostheses. DECT samples and proton samples have been produced from the same batch. The thicknesses of the solid proton samples (12 cm diameter disks) have been measured at their centre and at 4 different points over a radius of 30 mm using a Sylvac Z_cal 300 meter (Sylvac SA, Crissier) with an accuracy of 6 μm and precision of 2 μm. The solids have been weighted on a Mettler PM6000 balance (Mettler-Toledo, LLC) with an accuracy of 0.05%. From the determined volume and mass, mass densities have been calculated for the solid samples. The uncertainty in the measured thickness of the solid samples contributes most to the uncertainty in the mass densities, the uncertainty in diameter and mass are negligible. The uncertainty in the calculated densities is < 0.1% (except for PMMA and Teflon 0.3%) (1σ). Mass densities of the liquid samples have been measured as a function of the temperature using a DMA35N density meter with a specified accuracy of 0.001 [g cm^{-3}] (Anton Paar, Austria). For the analysis, the densities at a temperature of 23.8±0.1°C corresponding to the ambient temperature during the DECT experiment have been used. The temperatures of the water and measured samples during the proton experiments of 25.5±0.3 to 25.8±0.2°C

(ρ_w = 0.997 [g cm^{-3}]) yield an average deviation in the density of the liquid samples of -0.001 [g cm^{-3}] which is considered negligible. The densities of the samples n-pentane, n-hexane and n-heptane have been taken from the specifications of the manufacturer.

3.3.2 Dual energy CT imaging

The experimental DECT data for this study has been acquired at tube potentials of 90 kV and 150 kV with additional 0.6 mm tin filtration (150 kV Sn). The system weighting functions (SWFs) for 90 kV (j = 2) and 150 kV Sn (j = 1) have been calculated with eq. (2) from ref. 51 using the tube output spectra and detector responsivity provided by the manufacturer (Siemens Medical Solutions, Forchheim, Germany). In the photon energy range of the DECT measurement (the two SWFs of 90 kV and 150 kV Sn), the parameterization of the total electronic cross section as described by ref. 51 is accurate within 0.3% for atomic numbers Z between 1 and 30 (relative to the tabulated data of Berger *et al.*[44]).

All of the 32 DECT samples (with a diameter of 2.85 cm) have been measured in a 33 cm diameter Gammex 467 tissue characterization phantom (Gammex Inc., Middleton, WI, USA). The phantom has been scanned in different sample configurations with a clinical 90 kV / 150 kV Sn dual energy abdomen virtual noncontrast (VNC) protocol in spiral mode with a collimation of 64x0.6 mm and with 266 mAs (90 kV) and 166 mAs (150 kV Sn) (CTDI_{vol} = 15.5 mGy). The DECT data has been reconstructed with a Qr40 strength 5 advanced modeled iterative reconstruction (ADMIRE) kernel and a slice thickness of 1 mm for a field of view of 35 cm. Because the CT number of sample 32 (Al_2O_3) exceeded the scale at 90 kV it has been measured at 100 kV (230 mAs) and 150 kV Sn (115 mAs). From central slice DECT images, an effective atomic number Z' image has been obtained using the *fzero* function in MATLAB (MATLAB 8.3, The MathWorks Inc., Natick, MA, USA). The electron density ρ_e' image has been derived from the measured 150 kV Sn image and the determined Z' image. Z' and ρ_e' have been determined by averaging over circular regions in the respective images covering the samples but excluding air for which no effective atomic number can be solved. The calculated values Z'_c for the 32 materials have been determined from the specified composition and density as given in table 3.1 by calculating the ratio of linear attenuation coefficients and applying the DECT method to solve for Z'. For this, values for the linear attenuation coefficients have been calculated by spectrally weighing the electronic cross sections by the final normalized LWFs.

Table 3.1. Compositions (weight percentages) and mass densities ρ (at 23.8℃) of the 32 sample materials. Material No. 1-6 and 24-32 are solids and 7-23 are liquids.

No.	Material	Ch. formula	Z	1	6	7	8	9	12	13	14	17	19	20	25	ρ
			A	1.008	12.011	14.007	15.999	18.998	24.305	26.982	28.086	35.453	39.098	40.078	54.938	[g cm^{-3}]
1	LN-450 Lung			8.47	59.56	1.97	18.11	0	11.21	0	0.58	0.10	0	0	0	0.428
2	AP6 Adipose			9.06	72.29	2.25	16.27	0	0	0	0	0.13	0	0	0	0.946
3	BR-12 Breast			8.59	70.10	2.33	17.90	0	0	0	0	0.13	0	0.95	0	0.981
4	Solid Water M457			8.02	67.22	2.41	19.91	0	0	0	0	0.14	0	2.31	0	1.045
5	LV1 Liver			8.06	67.01	2.47	20.01	0	0	0	0	0.14	0	2.31	0	1.095
6	SB3 Cortical Bone			3.41	31.41	1.84	36.50	0	0	0	0	0.04	0	26.81	0	1.823
7	n-Pentane	C_5H_{12}		16.76	83.24	0	0	0	0	0	0	0	0	0	0	0.626
8	n-Hexane	C_6H_{14}		16.37	83.63	0	0	0	0	0	0	0	0	0	0	0.659
9	n-Heptane	C_7H_{16}		16.09	83.91	0	0	0	0	0	0	0	0	0	0	0.683
10	Methanol	CH_4O		12.58	37.48	0	49.93	0	0	0	0	0	0	0	0	0.791
11	Ethanol	C_2H_6O		13.13	52.14	0	34.73	0	0	0	0	0	0	0	0	0.788
12	Propan-1-ol	C_3H_8O		13.42	59.96	0	26.62	0	0	0	0	0	0	0	0	0.805
13	Propan-2-ol	C_3H_8O		13.42	59.96	0	26.62	0	0	0	0	0	0	0	0	0.785
14	Oleic acid	$C_{18}H_{34}O_2$		12.13	76.54	0	11.33	0	0	0	0	0	0	0	0	0.892
15	Ethyl acetoacetate	$C_6H_{10}O_3$		7.74	55.37	0	36.88	0	0	0	0	0	0	0	0	1.026
16	Water	H_2O		11.19	0	0	88.81	0	0	0	0	0	0	0	0	0.998
17	Polyethylene glycol 200	C_2H_4O		9.15	54.53	0	36.32	0	0	0	0	0	0	0	0	1.123
18	Glycerol	$C_3H_8O_3$		8.76	39.13	0	52.12	0	0	0	0	0	0	0	0	1.260
19	Silicone oil Siluron 5000	C_2H_6OSi		8.16	32.39	0	21.58	0	0	0	37.87	0	0	0	0	0.970
20	Potassium Chloride 4.01%	KCl H_2O		10.74	0	0	85.25	0	0	0	0	1.91	2.10	0	0	1.021
21	Potassium Chloride 7.71%	KCl H_2O		10.33	0	0	81.97	0	0	0	0	3.67	4.04	0	0	1.046
22	Potassium Chloride 11.13%	KCl H_2O		9.94	0	0	78.92	0	0	0	0	5.29	5.84	0	0	1.070
23	Potassium Chloride 20.03%	KCl H_2O		8.95	0	0	71.02	0	0	0	0	9.53	10.51	0	0	1.139
24	Carbon graphite	C		0	100	0	0	0	0	0	0	0	0	0	0	1.696
25	UHMWPE	$(C_2H_4)_n$		14.37	85.63	0	0	0	0	0	0	0	0	0	0	0.923

Table 3.1. Continued. Compositions (weight percentages) and mass densities ρ (at 23.8°C) of the 32 sample materials. Material No. 1-6 and 24-32 are solids and 7-23 are liquids.

No.	Material	Ch. formula	Z	1	6	7	8	9	12	13	14	17	19	20	25	ρ
			A	1.008	12.011	14.007	15.999	18.998	24.305	26.982	28.086	35.453	39.098	40.078	54.938	[g cm^{-3}]
26	Polypropylene	$(C_3H_6)_n$		14.37	85.63	0	0	0	0	0	0	0	0	0	0	0.919
27	Nylon 6.6-101	$(C_{12}H_{22}N_2O_2)_n$		9.80	63.68	12.38	14.14	0	0	0	0	0	0	0	0	1.142
28	PMMA	$(C_5H_8O_2)_n$		8.05	59.98	0	31.96	0	0	0	0	0	0	0	0	1.183
29	Polycarbonate	$(C_{16}H_{14}O_3)_n$		5.55	75.57	0	18.88	0	0	0	0	0	0	0	0	1.192
30	Teflon	$(C_2F_4)_n$		0	24.02	0	0	75.98	0	0	0	0	0	0	0	2.205
31	Aluminium $AlMgSi_1$			0	0	0	0	0	1	97.2	1	0	0	0	0.8	2.691
32	Al_2O_3 99.7%	Al_2O_3		0	0	0	47.07	0	0	52.93	0	0	0	0	0	3.892

3.3.3 Proton experiments and Monte Carlo simulations

The proton experiments have been performed using a 190 MeV (nominal) proton pencil beam scattered by a homogeneous 1.44 mm thick Pb scatter foil. The scattered field has been shaped by a sequence of collimators to finally obtain a 50 mm diameter scattered proton field. A water phantom has been developed for high accuracy measurements of depth dose profiles of protons in water. For the measurements a plane-parallel Markus ionization chamber type 23343 (PTW, Freiburg) has been used as recommended by the TRS 398 report[64]. The field shape and flatness have been analysed from images acquired at the position of the entrance window using a scintillation screen (Gd_2O_2S:Tb, Lanex^{TM}, Eastman Kodak Company, Rochester, NY)[65]. The solid proton samples of the materials listed in table 3.1 have been machined with a water equivalent thickness of about 20 mm to minimize the difference in energy loss within the sample between the different samples. The range has been defined as the depth corresponding to 80% of the maximum dose at the distal side of the Bragg peak ($R_{80\%}$). This corresponds for a monoenergetic beam to the mean projected range where 50% of the protons have stopped and is independent of the energy spread of the beam[31]. To determine the $R_{80\%}$, the Bragg peak measured with a step size of 0.2 mm has been interpolated using a cubic spline interpolation after which the signal has been normalized to the local maximum. From the differences in $R_{80\%}$ between the sample measurement and the reference water measurement a range shift and subsequently WET and RSP of the sample have been determined. The samples have been measured at 149 MeV and selected samples also at 89 and 62 MeV.

The geometry of the experimental proton beamline and the water phantom has been implemented in Geant4 (Geant4.9.6.p04). A water density ρ_w of 0.997 [g cm^{-3}] and a value for the mean excitation energy of water $\langle I_w \rangle$ of 78 eV have been used in the Geant4 simulations. The value for $\langle I_w \rangle$ is in accordance with measurements of Kumazaki *et al.*[66] who found 78.4±1.0 eV and with the errata and addenda for ICRU report 73, in which Sigmund *et al.*[67] introduce a value for $\langle I_w \rangle$ of 78 eV based on measurements of Schardt *et al.*[68]. The simulated primary energy of the protons (190 MeV nominal) has been adjusted to 189.3 MeV for which the simulated and measured depth dose profiles in water agree within 0.2 mm for the 4 performed experiments. The settings for the simulations correspond to the default physics settings of TOPAS beta version v1.0b12[57] with a range cut value of 0.05 mm for all particles. Geant4 simulations have been performed at the position of the entrance window and at different depths in the modelled water phantom to provide an indication of the field flatness at the relevant depths for analysis of the sample materials. Geant4 simulated RSPs have been derived from depth dose simulations in the same geometry and using the same analysis method as for the experimental RSPs. In the simulations, dose has been scored in the modelled water phantom in a cylinder with a radius of 10 mm and a bin size of 0.1 mm.

3.3.4 DECT based prediction of proton stopping powers

The measured effective atomic numbers Z' derived from DECT with 3 iterations of the LWF show a systematic deviation from the calculated ones for materials other than water (figure 3.2). The implementation of the LWF optimizes the Z' and $\rho_e{}'$ values in such a way that they are consistent with the CT numbers in the reconstructed image. This approach is different from the approach followed by Heismann and Balda[32] which uses raw CT data. By using the reconstructed CT data the different corrections applied in the reconstruction process influence the results, in particular the applied water correction. This correction leads to a flat calibrated CT number profile in a homogeneous water phantom but reconstructed CT numbers for materials different from water suffer from a systematic error. In materials with a higher Z' than water like bone, a larger amount of low energy photons are absorbed than in water increasing the average photon energy with respect to water. This increase in photon energy is reflected in a decreased value of the CT number and linear attenuation coefficient. For materials with a Z' smaller than water the average photon energy is decreased. The CT numbers for these materials are higher than expected based on their composition and density. To apply a material specific correction, the CT numbers of materials with a Z' higher than water should be increased and the CT numbers of materials with a Z' smaller than water should be reduced. However, these corrections are not applied in the CT reconstruction process and therefore a systematic deviation appears in the DECT determined Z'. This systematic deviation appears also in other spectral based DECT methods and has been confirmed from simulations as presented by Landry *et al.*[42,49]. The measured values for Z' have been calibrated with the calculated values for the materials with known composition and density using a linear relation of the form

$$Z'_{cal} = a\,Z' + b \tag{12}$$

where the values of the coefficients a (1.469) and b (-4.207) are determined from a least squares fit ($R^2 = 0.983$). In figure 3.2 the measured and calibrated values for Z' are presented. In clinical practice this calibration of Z' can be performed with materials of accurately known composition and density covering the clinically relevant Z' range.

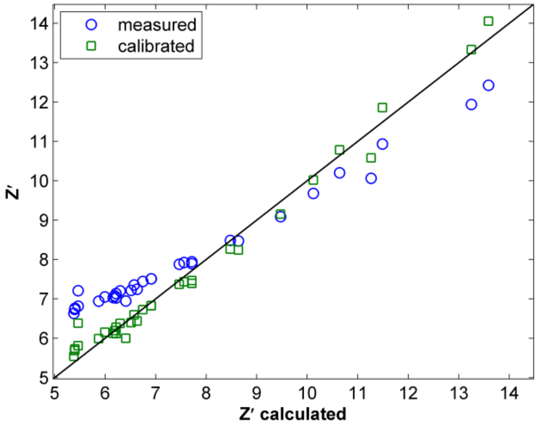

Figure 3.2. DECT measured and calibrated effective atomic numbers Z' for the 32 materials listed in table 3.1, solid line corresponds to a 1 to 1 relation.

To link Z' to the mean excitation energy $\langle I\rangle$ with a relatively smooth function the logarithm of the mean excitation energy has been divided by Z' and $\ln\langle I\rangle/Z'$ has been related to Z' with the following cubic function.

$$\frac{\ln\langle I\rangle}{Z'} = c\,Z'^3 + d\,Z'^2 + f Z' + g \tag{13}$$

The coefficients in this relation depend on the energies used for the DECT acquisition since the effective atomic number depends on the x-ray energies.

The effective atomic numbers Z' for 80 average tissues described by Woodard and White[17,39] have been calculated from the composition, density and SWF. For the 32 measured sample materials the calibrated effective atomic numbers Z'_{cal} have been used which more closely approach the ideally measured effective atomic numbers for each material. Mean excitation energies have been calculated from the composition using eq. (3). Figure 3.3a presents a graph of the ratio $\ln\langle I\rangle/Z'$ versus Z'. A clear relation is visible for the compound samples including the 80 tissues. Sample materials with a high contribution of one element and no hydrogen in their composition (carbon, Teflon, aluminium and Al_2O_3) deviate from the curve of the compounds but lie on a parallel curve with $\ln\langle I\rangle/Z$ versus Z of the elements (not shown in figure 3.3a). For hydrogen, Compton scattering is the only relevant interaction process, while the effective atomic number Z' is to a large extent determined by the Z dependence of photoelectric absorption in the heavier elements. Consequently the effective atomic numbers of the compounds with hydrogen are higher than a weigthed average of their composition. The mean excitation energy of hydrogen is small compared to the mean excitation energy of other elements like carbon and oxygen. This could explain the smaller $\ln\langle I\rangle$ value of compounds with hydrogen. Excluding the 4 materials carbon, Teflon, aluminium and Al_2O_3, the relation between $\ln\langle I\rangle / Z'$ and Z' can be established by the third order polynomial of eq. (13) with c, d, f and g as free parameters. The least squares fitted values of the free parameters are c (-2.655x10^{-4}), d (1.252x10^{-2}), f (-2.103x10^{-1}) and g (1.551) ($R^2 = 0.998$). The relative difference between $\ln\langle I\rangle$ determined from this relation and the values calculated with Bragg's additivity rule (eq. (3)) is within 1% for the 80 average tissues and within 3% for the samples (except for carbon, Teflon, aluminium and Al_2O_3) (figure 3.3b). A positive difference of 3% in $\ln\langle I\rangle$ gives rise to a -1.7% difference in RSP showing the importance of the accuracy of the derived relation. Besides the proposed cubic relation, a power law also provides a reasonable relation but shows slightly higher deviations in $\ln\langle I\rangle$ from calculated values.

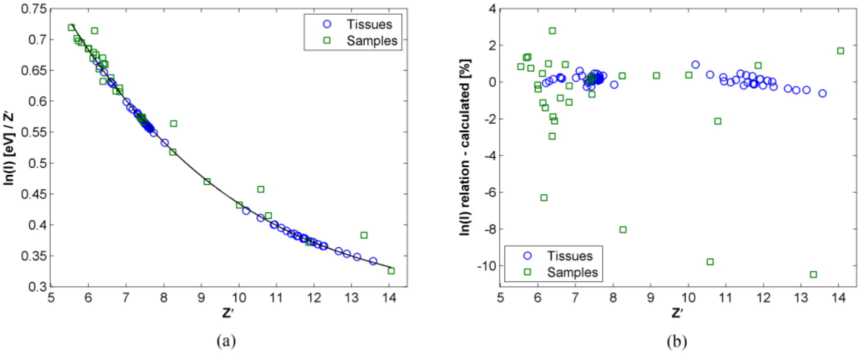

(a) (b)

Figure 3.3. (a) The ratio $\ln\langle I\rangle / Z'$ versus Z' for the 80 average tissues[17,39] and $\ln\langle I\rangle / Z'_{cal}$ versus Z'_{cal} for the 32 sample materials measured with DECT (table 3.1). The relation between $\ln\langle I\rangle / Z'$ and Z' is given by the solid line. (b) The relative difference between $\ln\langle I\rangle$ derived from the relation (eq. (13)) and the values calculated with Bragg's additivity rule (eq. (3)) for the average tissues and the samples.

To determine the RSP at a specific depth in water, first the corrected range in water $R_w(E_i)$ in eq. (11) has been derived from the measured range in water $R(E_k)$ for protons with an initial energy before entering the water (E_k) and the sample depth in water (d_m). Thereafter, eq. (10) has been solved for the initial energy E_i using eq. (1) with a value of the mean excitation energy of water $\langle I_w\rangle$ of 78 eV and an electron density $\rho_{e,w}$ of 3.336x10^{23} [e cm^{-3}]. In the measurements three sample depths d_m have been used corresponding with intial energies E_i of 62, 89 and 149 MeV. Subsequently, eq. (9) has been solved for a final energy E_f using the sample thickness (table 3.2) and eq. (1) with the DECT determined value for ρ_e' and $\ln\langle I\rangle$. By solving the integral in eq. (8) using E_i and E_f, the WET of the material has been derived. From the determined

WET, the RSP has been calculated as the ratio t_w/t_m. In clinical practice the proton energy can be derived from the measured range in water and RSPs can be calculated with eq. (4) using ρ_e^m/ρ_e^w and Z' derived from DECT with the relations described in eqs. (12) and (13).

3.4 Results

3.4.1 Experimental relative stopping powers

The scintillation screen measurement and Geant4 simulations are consistent and show that the flatness of the scattered proton field for a 10 mm radius is within 3% up to a depth of the $R_{80\%}$ in water. This validates the use of the Markus ionization chamber with a 5.3 mm diameter electrode for measurement of depth dose curves. The reproducibility of the experimental $R_{80\%}$ in water before and after each sample measurement was found to be within 31 μm. From the residual range measurements and material thickness RSPs have been derived with an uncertainty < 0.4% assuming one standard deviation in the measured thickness and reproducibility of the $R_{80\%}$. The experimentally derived RSPs at 149 MeV are given in table 3.2. The measured difference of the RSP at 62 MeV relative to 149 MeV for material numbers 7 to 23 is within 0.7%. For SB3 cortical bone (No. 6) the difference in RSP between 89 and 149 MeV is already 0.4%. At lower energies this change in RSP is expected to be even larger. In figure 3.4 RSPs for five materials are presented which have been calculated as a function of proton energy using eq. (4) with calculated relative electron densities ρ_e^m/ρ_e^w and mean excitation energies $\langle I_m \rangle$ based on the composition and density specified in table 3.1. The measured up and downward trends in RSP for these materials at decreasing proton energy are consistent with the calculations presented in figure 3.4.

3.4.2 Relative stopping powers derived from DECT and Geant4 simulations

The relative difference between the electron densities determined with DECT and calculated values based on the specified composition and density is given in table 3.2. The differences are within 1% except for LN-450, Teflon and aluminium. Figure 3.5 and table 3.2 present relative differences between the RSPs determined from Geant4 simulations and DECT with respect to experimentally measured RSPs at an initial proton energy E_i of 149 MeV. The difference in RSPs of almost all materials (except for LN-450, carbon, Teflon, aluminium and Al_2O_3) is within 2.1% for Geant4 simulations and within 1.9% for DECT.

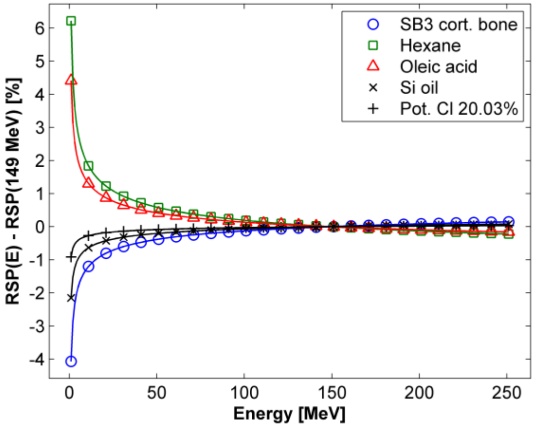

Figure 3.4. Relative difference between calculated relative stopping powers (RSPs) as a function of proton energy E and RSPs at 149 MeV for 5 materials from which the experimental RSPs are listed in table 3.2.

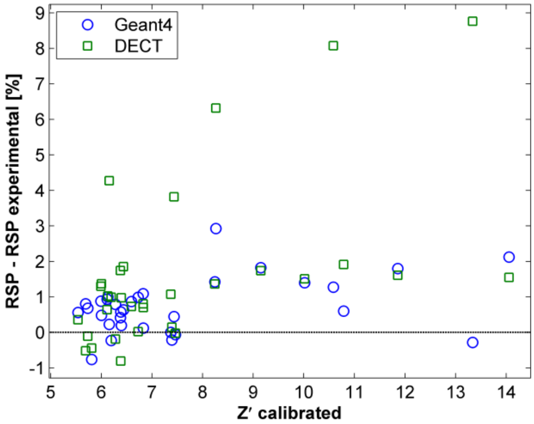

Figure 3.5. Relative differences between relative stopping powers (RSPs) predicted by Geant4 simulations or DECT and experimentally determined RSPs at an initial proton energy E_i of 149 MeV.

Table 3.2. The measured thickness ± 1 standard deviation of the 32 sample materials. Electron densities determined from DECT with 3 iterations of the LWF and relative differences with calculated values. Calibrated effective atomic numbers Z'_{cal} from DECT determined values for Z'. Relative stopping powers (RSPs) derived from Geant4 simulations (composition and density from table 3.1) and DECT compared to experimental RSPs determined with an uncertainty < 0.4% at an initial proton energy E_i of 149 MeV.

No.	Material	Thickness [mm]	ρ_e' meas x10^{23}[e cm^{-3}]	ρ_e' meas-calc [%]	Z' cal	RSP Geant4	RSP DECT	RSP Exp	RSP Geant4-Exp [%]	RSP DECT-Exp [%]
1	LN-450 Lung	46.977 ± 0.007	1.437	3.1	7.44	0.423	0.437	0.421	0.5	3.8
2	AP6 Adipose	22.017 ± 0.009	3.114	0.5	6.19	0.949	0.961	0.951	-0.2	1.1
3	BR-12 Breast	21.033 ± 0.008	3.224	0.7	6.83	0.980	0.986	0.979	0.1	0.7
4	Solid Water M457	19.99 ± 0.01	3.398	0.1	7.46	1.032	1.033	1.033	-0.1	0.0
5	LV1 Liver	20.014 ± 0.009	3.571	0.4	7.39	1.082	1.086	1.084	-0.2	0.2
6	SB3 Cortical Bone	12.94 ± 0.01	5.704	0.6	14.06	1.656	1.647	1.622	2.1	1.5
7	n-Pentane	20.31 ± 0.10	2.197	0.1	5.54	0.687	0.686	0.684	0.4	0.3
8	n-Hexane	20.31 ± 0.10	2.291	-0.5	5.69	0.723	0.713	0.717	0.8	-0.6
9	n-Heptane	20.31 ± 0.10	2.377	-0.2	5.73	0.745	0.739	0.740	0.7	-0.1
10	Methanol	20.32 ± 0.09	2.665	-0.4	6.73	0.824	0.816	0.816	1.0	0.0
11	Ethanol	20.32 ± 0.09	2.693	0.6	6.00	0.826	0.833	0.822	0.5	1.3
12	Propan-1-ol	20.32 ± 0.09	2.725	-0.7	6.28	0.847	0.839	0.841	0.7	-0.2
13	Propan-2-ol	20.32 ± 0.09	2.678	0.1	6.12	0.829	0.827	0.822	0.9	0.6
14	Oleic acid	20.28 ± 0.09	3.012	0.2	5.99	0.928	0.932	0.920	0.9	1.3
15	Ethyl acetoacetate	20.32 ± 0.09	3.324	0.0	6.44	1.009	1.021	1.003	0.6	1.8
16	Water	20.28 ± 0.09	3.323	-0.4	7.37	1.000	1.011	1.000	0.0	1.1
17	Polyethylene glycol 200	20.28 ± 0.09	3.662	-0.6	6.59	1.124	1.123	1.115	0.8	0.7
18	Glycerol	20.31 ± 0.10	4.082	-0.9	6.83	1.252	1.248	1.238	1.1	0.8
19	Silicone oil Siluron 5000	19.815 ± 0.000	3.159	0.2	10.79	0.932	0.944	0.926	0.6	1.9
20	Potassium Chloride 4.01%	20.28 ± 0.09	3.398	0.1	8.24	1.028	1.028	1.014	1.4	1.4
21	Potassium Chloride 7.71%	20.28 ± 0.09	3.463	0.0	9.15	1.044	1.043	1.025	1.9	1.8
22	Potassium Chloride 11.13%	20.28 ± 0.09	3.529	0.1	10.02	1.058	1.059	1.043	1.4	1.5
23	Potassium Chloride 20.03%	20.28 ± 0.09	3.717	0.2	11.86	1.104	1.102	1.084	1.8	1.7
24	Carbon graphite	12.03 ± 0.01	5.129	0.5	6.15	1.521	1.583	1.518	0.2	4.3
25	UHMWPE	18.18 ± 0.02	3.188	0.6	5.81	0.987	0.990	0.994	-0.7	-0.4

Table 3.2. Continued. The measured thickness ± 1 standard deviation of the 32 sample materials. Electron densities determined from DECT with 3 iterations of the LWF and relative differences with calculated values. Calibrated effective atomic numbers Z'_{cal} from DECT determined values for Z'. Relative stopping powers (RSPs) derived from Geant4 simulations (composition and density from table 3.1) and DECT compared to experimental RSPs determined with an uncertainty < 0.4% at an initial proton energy E_i of 149 MeV.

No.	Material	Thickness [mm]	ρ_e' meas x10^{23}[e cm^{-3}]	ρ_e' meas-calc [%]	Z' cal	RSP Geant4	RSP DECT	RSP Exp	RSP Geant4-Exp [%]	RSP DECT-Exp [%]
26	Polypropylene	18.962 ± 0.007	3.157	0.0	6.38	0.984	0.971	0.979	0.5	-0.8
27	Nylon 6.6-101	15.96 ± 0.02	3.757	-0.3	6.13	1.160	1.160	1.148	1.0	1.0
28	PMMA	15.94 ± 0.04	3.835	-0.2	6.40	1.170	1.179	1.168	0.2	0.9
29	Polycarbonate	15.93 ± 0.02	3.772	-0.3	6.38	1.145	1.160	1.140	0.4	1.8
30	Teflon	10.59 ± 0.03	6.286	-1.4	8.26	1.841	1.901	1.788	3.0	6.3
31	Aluminium $AlMgSi_1$	8.96 ± 0.01	7.942	1.7	13.34	2.123	2.315	2.129	-0.3	8.7
32	Al_2O_3 99.7%	7.089 ± 0.001	11.548	0.5	10.58	3.238	3.456	3.198	1.3	8.1

3.5 Discussion

3.5.1 Electron densities and relative stopping powers

The relatively large deviation of 3.1% in the DECT determined electron density of the inhomogeneous LN-450 material is most likely due to reduced statistics and the partial volume effect since the material encloses air in its structure. The materials carbon, Teflon, aluminium and Al_2O_3 show a different systematic in the relation between the effective atomic number and mean excitation energy than the other examined materials. Consequently, the deviations in the DECT derived RSPs for these materials are larger. This is possibly due to the absence of hydrogen in their composition. Teflon yields a large deviation in the predicted RSP both with DECT (6.3%) and simulation (3.0%).

In the simulations a mean excitation energy of water $\langle I_w \rangle$ of 78 eV has been used. The DECT predicted value for $\langle I_w \rangle$ is based on Bragg's additivity rule which gives a value of 69 eV. This explains the positive deviation of 1.1% for water with DECT (table 3.2) because an underestimation of the $\langle I \rangle$ value leads to an overestimation of the RSP. The RSP of silicone oil (table 3.2 No. 19) at 51.2 MeV (average in sample) has been predicted from DECT with a difference of 2.1% relative to the experimentally determined RSP. Weber *et al.*[69,70] noticed that the SECT based stoichiometric calibration curve assigns a density of 1.06 [g cm^{-3}] to silicone oil instead of the specified 0.97 [g cm^{-3}] which translates into a 9.3% difference in stopping power. This leads to a clinically important range difference of 2 mm at 61 MeV.

3.5.2 Uncertainty discussion

The uncertainty in the experimental RSPs (< 0.4%) is dominated by the uncertainty in the measured thickness of the samples. The predominantly positive differences between simulations and DECT with respect to the experimental RSPs indicates an overestimation of the RSP by DECT and simulation. For DECT these deviations can be due to the limited accuracy of the relation between the effective atomic number and mean excitation energy and the approximation of the Bethe-Bloch formula given in eq. (1). However, Geant4 simulations do include shell and higher order corrections in the Bethe-Bloch formula but also show deviations from the experimental values. Both, DECT and simulations use Bragg's additivity rule and elemental $\langle I \rangle$ values from ICRU report 37[71] for determining the $\ln\langle I \rangle$ value of compounds except for reference water. Deviations from Bragg's additivity rule seem to be restricted to the low energy region (below 4 MeV) and therefore its impact on the calculated range is very limited[72]. The selection of elemental $\langle I \rangle$ values might be a factor influencing the DECT and Geant4 predicted stopping powers. Bichsel and Hiraoka[73] measured stopping powers of 70 MeV protons in elements relative to aluminium and determined elemental $\langle I \rangle$ values which are predominantly higher than the values given in the ICRU report 37[71]. Hiraoka *et al.*[74] derived experimental $\langle I \rangle$ values for organic compounds which are higher than the $\langle I \rangle$ values calculated with Bragg's additivity rule using elemental $\langle I \rangle$ values from ICRU report 49[75]. The experimental $\langle I \rangle$ value of water of 78 eV is also higher than the 69 eV calculated with Bragg's additivity rule. If there is an underestimation of the elemental $\langle I \rangle$ values given in ICRU report 37[71] and ICRU report 49[75] this might explain the positive deviations in RSPs found in this study. Besemer *et al.*[76] studied the clinical impact of varying the tissue $\langle I \rangle$ values with 5 and 10% and found this to cause range shifts up to 7.7 mm and mean dose differences up to 3.5%. This emphasises the clinical relevance of the uncertainty in the mean excitation energy when using the Bethe-Bloch formula for calculation of stopping power and range. In addition to the uncertainty in mean excitation energy it might be possible that the correction factors to the Bethe-Bloch equation are not known accurately enough to achieve sub-percent accuracy in calculation of relative stopping powers. For assessing the accuracy of different methods (DECT or proton CT) to predict RSPs on a sub percent level both the calculation and measurement accuracy of RSPs are limiting factors. Measurement of RSPs with an accuracy $< 0.1\%$ requires a higher energy stability of the proton beam and micrometer accuracy in the measured thickness of samples with a water equivalent thickness of 2 cm.

3.5.3 **Comparison with other work**

Different DECT based methods for effective atomic number, electron density as well as stopping power prediction based on phantom calibration measurements have been presented in the literature[41,42,50,52,54]. These calibration methods use a dual energy CT scan of one calibration material[52] or a set of tissue substitutes[41,42,50,54] to determine method specific parameters to derive effective atomic numbers and electron densities.

In the determination of the accuracy of their method Hünemohr *et al.*[52] measured Gammex materials, polymers and metals with DECT in the centre of a small PMMA phantom reducing the influence of beam hardening. Carbon ion RSPs have been predicted by their DECT method within 1.4% for tissue surrogates and up to 3.5% for polymers compared to the experimental values. To explicitly compare the method of Hünemohr *et al.*[52] as implemented in *syncho.via* DE Rho/Z maps (Siemens Medical Solutions, Forchheim, Germany) with our proposed method, our DECT images have been analysed with their method. The results show that the calibrated effective atomic numbers presented in this study are comparable with their effective atomic numbers but the systematic deviation visible in our Z' appears in their relative electron densities with deviations up to -3% for SB3 cortical bone.

Bourque *et al.*[54] proposed a three segment high order polynomial relation between Z' and $\ln\langle I\rangle$. In this work we propose a single polynomial relation where a power law relation is also possible to relate $\ln\langle I\rangle/Z'$ and Z'. Hudobivnik *et al.*[77] used the method proposed by Landry *et al.*[42] to derive the effective atomic number using a fitting procedure with calibration inserts. The electron density was derived using the method of Saito *et al.*[41,50] with a fit to the electron density of the calibration inserts. The relation between Z' and $\ln\langle I\rangle$ has been adopted from Yang *et al.*[23] and Bourque *et al.*[54]. With this approach Hudobivnik *et al.*[77] determined RSPs within 2.5% of experimental RSPs for 12 Gammex and 6 CIRS tissue substitutes measured with DECT in a 15 cm diameter phantom with restricted influence of beam hardening.

All methods described so far use dual energy CT scans of one or more sample materials as a calibration to derive the effective atomic number and electron density. The calibration measurements performed in these methods are influenced by the limited accuracy of the reconstructed CT numbers. The method described in this work includes a CT system description and a physics based parameterization of the electronic cross section. In contrast to the calibration methods, this method includes a local energy weighting which accounts for a material specific energy weighting of the model to correspond with the measured CT numbers. In this process, the influence of object size on the beam hardening is quantitatively included. Because of the systematic error caused by the beam hardening correction applied in the reconstruction process a calibration of the effective atomic number is needed. This calibration does not affect the electron density which is directly related to the stopping power and has been determined with high accuracy (~1%). We have validated our method on a large variety of materials extending the standard tissue substitutes. For most materials the RSPs obtained from our DECT analysis method are within 2% of experimental values. Our DECT predicted RSPs show predominantly positive differences with respect to the experimental RSPs which are consistent with the positive differences found from Geant4 simulations. These positive differences could perhaps be explained by an underestimation of tabulated elemental mean excitation energies.

3.5.4 SECT and DECT for dose calculation

For Monte Carlo based dose calculations the DECT derived effective atomic number and electron density can be related to a mass density and composition. Hünemohr *et al.*[78] implemented a linear fit in the electron density to derive the mass density as reported by Beaulieu *et al.*[79]. For the average tissues such a relation can predict mass densities within 1% but for the samples as given in table 3.1 the relative differences are up to 6% (LN-450: -27%). In deriving the elemental mass fractions large uncertainties in the carbon and oxygen contributions have been presented by Hünemohr *et al.*[78]. In our opinion, DECT does not provide sufficient information to allow accurate quantification of elemental mass fractions. Schneider *et al.*[19] presented a SECT based method to determine the mass density and elemental mass fractions. Since different materials can exhibit the same CT numbers at one kV setting such a method is not specific. SECT combined with a model based on average tissue compositions and densities can only provide generic, model dependent tissue RSPs. The described DECT method can provide patient specific tissue RSPs.

3.6 Conclusions

In this study we have described and assessed a method to derive relative proton stopping powers from DECT images by means of the electron density and relating the effective atomic number to the mean excitation energy in the Bethe-Bloch equation. With this DECT method electron densities have been determined for 29 of the 32 materials within 1% accuracy. Relative stopping powers derived from DECT are for most materials within 2% of the experimental values. This is comparable with the accuracy in relative stopping powers found in the Geant4 simulations. The proposed DECT based method provides patient specific tissue relative stopping powers and is a promising technique to reduce the uncertainty in proton range calculations in proton therapy treatment planning.

Chapter 4

High accuracy proton relative stopping power measurement

Abstract

Proton therapy is a fast growing treatment modality for cancer and is in selected cases preferred over conventional radiotherapy with photons because of the highly conformal dose distribution to the tumour that can be achieved with protons due to their dose deposition properties. The steep dose gradients of protons make proton therapy sensitive to range uncertainties.

To reduce range uncertainties from the translation of patient computed tomography (CT) data to tissue proton stopping powers relative to that in water (RSPs), dual energy CT (DECT) based RSP estimation methods have been proposed. High accuracy measurement of RSPs is required to assess the accuracy of these DECT analysis methods. Most DECT based RSP estimation methods use an approximate model of the proton stopping power. In this work we provide a literature study on proton stopping theory and estimate the accuracy of this approximation.

A water phantom has been developed to enable accurate measurement of depth dose profiles in water. Experimental RSPs can be derived from measured depth dose distributions with and without a sample positioned in the water. To determine the accuracy of Geant4 Monte Carlo simulations for RSP prediction, a simulated depth dose distribution and simulated RSPs have been compared to the experimental data.

From the literature study the accuracy of the approximate model of the proton stopping power is estimated at 1-1.5% for clinically relevant energies while the impact on the RSP is < 0.3%. Experiments with 190 MeV protons showed that depth dose profiles in water can be measured with a reproducibility better than 0.03 mm. The Geant4 Monte Carlo simulated depth dose profile is in good agreement with the experimental depth dose profiles. With the experimental setup, RSPs can be determined with a total uncertainty smaller than 0.4% for samples with a water equivalent thickness of about 2 cm. The accuracy of the measured RSPs is such that they can be used to test the validity of RSPs derived from DECT imaging and Monte Carlo simulations.

4.1 Introduction

The potential advantage of protons over conventional radiation modalities (photons, electrons) for radiotherapy of cancer was first mentioned by Wilson in 1946[5]. Protons have a finite range and local high dose region which facilitate a higher conformity to the tumour and less dose to the surrounding healthy tissues as compared to conventional irradiation with photons. Accurate positioning of the local high dose region is critical for exploiting the benefit of protons over photons. Each tissue is characterized by a proton stopping power relative to water (relative stopping power, RSP) that is derived from x-ray computed tomography (CT) data of the patient. Uncertainties in these RSPs introduce range uncertainties which have to be taken into account in treatment planning by using safety margins. These safety margins reduce the possibility to fully exploit the advantage of proton irradiations by limiting beam angles and increasing dose to healthy and sometimes critical tissues surrounding the tumour. Different methods have been proposed to derive RSPs from CT data of the patient. Single energy CT (SECT) methods typically correlate measured CT numbers to RSPs based on calculated CT numbers and RSPs for tissue substitutes or average tissue compositions[18,34]. Dual energy CT (DECT) provides measured CT numbers for two different spectral photon distributions and allows determination of the relative electron density and an effective atomic number[21,37,41,42,50-52]. RSPs can be calculated from the measured relative electron density and a relation between this effective atomic number and the mean excitation energy in the Bethe-Bloch formalism for calculation of stopping powers[52,54]. To assess the validity of the different CT-based methods for calculation of RSPs an accurate method for measurement of RSPs is needed.

We first assess the uncertainty in the approximation of the proton stopping power (Bethe-Bloch formula without higher order corrections) used for the CT based RSP estimates on basis of the available literature. Thereafter, the experimental determination of RSPs by measuring depth dose distributions using a water phantom in a proton beamline is described. The differences between Geant4 Monte Carlo simulated and experimental depth dose distributions of protons in water are assessed. The uncertainty in deriving RSPs from residual range measurements with the water phantom is estimated and compared to other experimental methods. RSPs calculated using the approximation of the proton stopping power are compared to Geant4 simulated RSPs which include the correction terms to the stopping power. This provides an estimate of the impact of neglecting the correction terms in the Bethe-Bloch formalism on the derived RSP.

4.2 Materials and methods

4.2.1 Accuracy of proton stopping theory

The total proton stopping power is due to energy transfer of the proton to the electrons (electronic stopping) and to the nuclei (nuclear stopping) of the target material. Electronic stopping causes ionization and excitation of target atoms and energy loss of the proton. Nuclear stopping changes the direction of the proton and the intensity of the incoming proton beam and contributes less than 0.1% to the total stopping power above 0.4 MeV[60]. The Bethe-Bloch formula that describes the electronic stopping power of protons can be expressed as[59,72]

$$S = -\frac{\mathrm{d}E}{\mathrm{d}x} = \frac{4\pi r_e^2 m_e c^2}{\beta^2} N_A \rho \frac{Z}{A} L(\beta) \tag{1}$$

with r_e the classical electron radius and $m_e c^2$ the electron rest mass with c the speed of light in vacuum. The electronic stopping power depends on the electron density of the target material ρ_e which equals $N_A \rho\, Z/A$ with mass density ρ, Avogadro's number N_A, atomic number Z and atomic weight A. The energy loss is proportional to $1/\beta^2$ with $\beta = v/c$ with v the proton velocity. The stopping number $L(\beta)$ is the sum of the primary stopping number L_0, the Barkas correction L_1, the Bloch correction L_2 and higher order corrections which are negligible compared to L_1 and L_2.

$$L(\beta) = L_0(\beta) + L_1(\beta) + L_2(\beta) + \cdots \tag{2}$$

The primary stopping number L_0 can be expressed as

$$L_0(\beta) = f(\beta) - \ln\langle I\rangle - \frac{C}{Z} - \frac{\delta}{2} \tag{3}$$

where $f(\beta)$ is defined as

$$f(\beta) = \ln\left(\frac{2m_e c^2 \beta^2}{1-\beta^2}\right) - \beta^2 \tag{4}$$

The mean ionization energy term $\ln\langle I\rangle$ takes into account the electronic structure of the target material. The mean excitation energy $\langle I\rangle$ is defined as the effective value (averaged over all possible electron states (ionization, vibration and excitation)) of the minimum energy transfer in a collision. The shell correction term C/Z addresses the fact that when the proton velocity decreases from relativistic energies the proton velocity is no longer much larger than the bound electron velocity as required for the Bethe-Bloch theory to be valid. The density effect term $\delta/2$ corrects for polarization effects in the target material, reducing the stopping power by a decrease of the assumed free-space electromagnetic field of the proton by the dielectric constant of the target material[72].

We have estimated from information in the literature the relative importance of the different correction terms with respect to the term $f(\beta) - \ln\langle I \rangle$. Shell corrections become especially important for the inner shell electrons of the heavier elements. They have been calculated using hydrogenic wave functions[80] or the local density approximation[72]. Both methods seem to give consistent results. Low Z elements have the smallest correction. For elements most relevant for proton therapy ($Z < 20$) the absolute value of the correction term is around 0.15 between 1 and 10 MeV and decreases to < 0.1 between 10 and 40 MeV and < 0.05 between 40 and 250 MeV. This corresponds to a relative decrease of the stopping power of 3-4% for energies between 1 and 10 MeV and approximately 1-1.5% between 10 and 40 MeV and < 1% for energies between 40 and 250 MeV. The density effect only becomes relevant if the kinetic energy of the proton exceeds its rest mass and is therefore of limited importance in the proton energy range used clinically (up to 250 MeV)[59]. The absolute contribution of the density effect is estimated to be smaller than 0.01 for all elements and energies below 200 MeV. Because $f(\beta) - \ln\langle I \rangle$ is larger than 5 for Z between 1 and 20 and energies larger than 10 MeV this implies a correction < 0.2%.

The Barkas correction corrects for the higher density of target electrons in the vicinity of the positively charged proton. For low energy protons this effect becomes important because the target electrons have time to move towards the stopping protons. Ashley *et al.*[81] derived an empirical formula to approximate this effect. Bichsel[60] derived an expression valid for energies between 0.8 and 5.6 MeV. From the empirical approach of Ziegler (ref. 59, eq. 35) we estimate that the Barkas correction may amount to 6% for 1 MeV but is smaller than 1% for energies above 10 MeV for aluminium. The Bloch correction originates from close collisions of protons with target electrons and mostly depends on the proton energy and little on the target material. Using eq. 5 from Bichsel[60] we conclude that the Bloch correction is smaller than 0.2% for energies between 5 and 10 MeV and < 0.1% above 10 MeV.

Bragg and Kleeman[61] proposed an additivity rule for mass stopping powers S/ρ of elements to determine the mass stopping power of a mixture or compound. Following this Bragg additivity rule the mean excitation energy $\ln\langle I \rangle$ of a compound can be approximated by

$$\ln\langle I \rangle = \frac{\sum_k \omega_k \frac{Z_k}{A_k} \ln\langle I_k \rangle}{\sum_k \omega_k \frac{Z_k}{A_k}} \tag{5}$$

with the mass fraction ω_k and mean excitation energy $\langle I_k \rangle$ of element k in the compound. The validity domain and the accuracy of the Bragg additivity rule have not been well established. The Bragg additivity rule does not account for different states of aggregation and chemical binding between atoms in a molecule. The effect of the state of aggregation is for water (vapor, liquid or ice) the largest for proton energies of 50-100 keV[82]. From core and bond corrections applied in the software package SRIM[72] to account for chemical binding we conclude that the corrections may amount to 6-7% in the stopping region (up to 1 MeV) and are applied as a constant (energy independent) scaling factor. For energies above 3-4 MeV no corrections are applied in SRIM. The uncertainty in the $\langle I \rangle$ values of the elements is difficult to estimate but experiments suggest that tabulated elemental $\langle I \rangle$ values[71,75] are too low[73,74].

The range of a 10 MeV proton in water in the continuous slowing down approximation (CSDA) is 1.23 mm and this decreases rapidly for lower energies: for 5 MeV protons it has already decreased to 0.36 mm[83]. Consequently, for energies below 10 MeV, correction terms which contribute less than 10% are not relevant for the total range prediction with the Bethe-Bloch formula. However, these corrections are important for dose calculation in the distal part (last mm) of the Bragg curve. The overall contribution of the correction terms is dominated by the shell correction which amounts -1.5 to -1% for energies between 10 and 40 MeV and -1 to 0% between 40 and 250 MeV. The Barkas correction contributes < 1% above 10 MeV. These corrections partly cancel out due to their respectively negative and positive sign. As the higher energies contribute most to the range (40 MeV protons have a CSDA range of only 1.49 cm[83]), the total effect on the range of all correction terms is estimated to be less than 1-1.5% for protons with clinically relevant energies.

The electronic stopping power of a material can be approximated within this estimated accuracy of 1-1.5% by

$$S = -\frac{\mathrm{d}E}{\mathrm{d}x} = \frac{4\pi r_e^2 m_e c^2}{\beta^2} \rho_e \left(f(\beta) - \ln\langle I \rangle\right) \tag{6}$$

The electronic stopping power relative to water (relative stopping power, RSP) can then be approximated by

$$\frac{S_m}{S_w} = \frac{\rho_e^m}{\rho_e^w} \left(\frac{f(\beta) - \ln\langle I_m \rangle}{f(\beta) - \ln\langle I_w \rangle} \right) \tag{7}$$

with the relative electron density ρ_e^m / ρ_e^w and mean excitation energy $\langle I_m \rangle$ of the material.

4.2.2 Experimental depth dose distributions

4.2.2.1 Water phantom design

The water phantom (figure 4.1) is equipped with two parallel TSL 120 translation stages with a stroke length of 500 mm (IKO Japan, Nippon Thompson Europe BV). The stages, including a 5 phase stepping motor (VEXTA-PK566, Oriental Motors), have a positioning accuracy of 0.045 mm, a precision of 0.002 mm and a backlash of 0.003 mm. An ionization chamber holder made from polycarbonate has been mounted to one of the stages to accurately move an ionization chamber along the beam for scanning a depth dose profile. A plane-parallel Markus ionization chamber type 23343 (PTW, Freiburg) has been used as recommended by the TRS 398 report[64]. A sample can be positioned in a holder which is mounted on the other stage. The Markus chamber is positioned downstream of the sample such that a depth dose profile can be measured. The absolute positions of the ionization chamber and sample have been determined using MY-COM A30/80 limit switches (Baumer) with a precision < 1 μm. On the downstream side of the water phantom a PT100 temperature sensor has been mounted to measure the water temperature during the measurements. The readout of the PT100 is connected to a LabVIEW (National Instruments) program which also controls the operation of the stages and the beam and writes the measured data to output files. The entrance window of the water phantom is a 2.90 mm thick circular impression with a radius of 55 mm milled in a 14.86 mm thick polycarbonate plate. For the experiments, the water phantom has been filled with demineralized water. The water temperature was stabilized to 25.5±0.3°C by circulating the water through a temperature regulated thermal buffer.

Figure 4.1. Experimental setup of the water phantom with its entrance window placed at the device under test (DUT) position. An ionization chamber is positioned in the water phantom on a translation stage to enable measurement of depth dose profiles.

4.2.2.2 Proton beamline and experimental setup

The AGOR cyclotron produces a 190 MeV (nominal) proton pencil beam with a full width at half maximum (FWHM) of 4 mm. The beam has an energy spread of

0.25% FWHM. The protons exit the vacuum of the beam pipe through a 70 μm thick aramica foil and then are incident on a homogeneous 1.44 mm thick Pb scatter foil. Two collimators (diameters 2.4 cm and 4.5 cm) shape the scattered field. Thereafter the beam intensity is measured with a parallel plate air ionization monitor (BIM: beam intensity monitor). A third collimator removes the halo from the proton field after which a collimator with an inner diameter of 50 mm determines the final shape of the field. The proton field at the device under test (DUT) position (at 329.6 cm distance from the exit foil) has been imaged using a scintillation screen (Gd_2O_2S:Tb, Lanex^{TM}, Eastman Kodak Company, Rochester, NY). This scintillation screen is placed perpendicular to the beam direction and is imaged via a mirror reflecting light at a 90° angle to a CCD camera[65]. For measurement of depth dose profiles, the entrance window of the water phantom has been placed at the DUT position.

4.2.2.3 Measurement and analysis of depth dose distributions

Four different experiments have been performed of approximately 18 hours each. In these experiments the field flatness has been verified after which depth dose distributions have been measured in water. The depth dose distributions have been measured with a step size of 5 mm in the plateau region and 0.2 mm in the Bragg peak by administering a dose of 0.5 to 1 Gy per point. For reproducibility measurements only the region starting just before the Bragg peak has been scanned. The measured depth dose distributions have been corrected for background in both the BIM and the Markus chamber reading using the time intervals counted with a fixed frequency pulser. The proton range has been defined as the distal 80% of the maximum dose in the Bragg peak ($R_{80\%}$). At this point, 50% of the protons have stopped independent of the energy spread of the beam[31]. The Bragg peaks measured with a step size of 0.2 mm have been interpolated with a cubic spline interpolation. From the splined Bragg peak, the local maximum has been defined as the position at which the first derivative of the spline equals zero and the signal has been normalized to this local maximum. For a sample measurement a range shift can be determined from the difference in $R_{80\%}$ between the measurement in water with and without the sample positioned in the water. As described in chapter 3, a water equivalent thickness (WET) can be derived from the measured range difference and the material thickness. The water equivalent ratio (WER, t_w/t_m), considered as the relative stopping power (RSP) of the sample, can be determined from the measured WET of the sample (t_w) and the sample thickness (t_m). The data analysis has been implemented in a commercially available software package (MATLAB 8.3, The MathWorks Inc., Natick, MA, USA). This analysis method to determine experimental RSPs has been applied to 32 materials (table 3.1). In this chapter we focus on the accuracy of this method and provide only details relevant for the assessment of this accuracy.

4.2.3 Geant4 simulated depth dose distributions

The flatness of the transverse profile of the radiation field as a function of depth in the phantom has been determined with Geant4 Monte Carlo simulations[58] of the experimental setup. The simulation has been validated by comparing the simulated Bragg curve (depth dose distribution) and the transverse profile of the radiation field at the entrance of the phantom with measurements. The experimental proton beamline from the exit foil to the DUT position has been modelled in Geant4 (Geant4.9.6.p04). At the DUT position the water phantom is represented by a polycarbonate front wall including the entrance window followed by a water column of 25x25x55 cm^3. A proton beam with the specifications listed in the previous section has been simulated starting just upstream of the exit foil. For the mean excitation energy of water $\langle I_w \rangle$ a value of 78 eV has been adopted corresponding to the updated ICRU 73 value[67]. The density of water ρ_w has been set at 0.997 [g cm^{-3}] corresponding to the density of water during the experiments. The physics list as implemented in Geant4 uses the physics settings of TOPAS beta version v1.0b12[57] with a range cut value of 0.05 mm for all particles.

The RSPs of samples with known composition and density derived from Geant4 simulations have been compared to experimental RSPs (chapter 3). The simulations have been checked on consistency with the experiments by determining the difference between a Geant4 simulated depth dose distribution and experimentally measured depth dose distributions in water. For the simulation, dose has been scored with depth in water with a bin size of 0.1 mm over a radius of 10 mm. Because the field is flat within 3% up to a radius of 10 mm, this radius has been selected to improve statistics. The simulated data has been interpolated with a third order spline and normalized using the same method as applied to the experimental data.

4.3 Results and discussion

4.3.1 Experiments and Monte Carlo simulations

The Lanex scintillation screen images and the Geant4 simulation showed that the flatness of the field for a 10 mm radius is within 3% up to a depth of the $R_{80\%}$ in water. This justifies the use of the Markus ionization chamber with a 5.3 mm diameter electrode for measurement of depth dose distributions.

The proton energy in the simulations has been adjusted to 189.3 MeV by minimizing the range difference between the simulation and experiments and is in good correspondence with calculations of the beam dynamics in the cyclotron. Geant4 simulated and measured depth dose distributions in water for the first experiment are presented in figure 4.2 (top). The differences between the Geant4 simulated depth dose distribution and the depth dose distributions measured in the 4 performed experiments are smaller than 3% up to the $R_{80\%}$ (e.g. figure 4.2 bottom). In the distal falloff of the Bragg curve (after the $R_{80\%}$) where the energy of the protons becomes small, the differences between simulation and experiments increase. This could be due to a difference in energy spread between simulation and experiment. However, it should be noted that in the steep distal falloff, small differences in position will already lead to large differences in the ratio between simulation and experiment.

During operation, the cyclotron magnetic field slowly drifts in the order of a hundredth of a percent over a period of around 24 hours due to warming up of the iron poles. Due to this drift there is a slow change in energy of the beam. Figure 4.3 represents the measured ranges ($R_{80\%}$) as a function of time during one of the experiments. The reproducibility of the $R_{80\%}$ in water during the performed experiments was within 0.058 mm, 0.095mm, 0.052 mm and 0.071 mm. The variations in beam energy limit the reproducibility of depth dose distributions in water. This reproducibility is essential for accurate measurement of the range difference between a Bragg curve measured after a sample and a measurement in water only. For these range difference measurements the nearest measured depth dose distribution in water can be used to reduce the variation in the reference water measurement since the energy drifts only slowly between two depth dose measurements in water.

4.3.2 Uncertainties in experimental relative stopping power determination

Experimental determination of proton relative stopping powers of materials is subject to different sources of uncertainty. A first uncertainty is the energy stability of the proton beam in between the reference water measurement and the sample measurement as mentioned in the previous section. A change in energy translates in a measured range difference and restricts the reproducibility of the measured range in water. The mechanical uncertainty in the ionisation chamber measurement is assumed to be negligible since the precision of the stepping motor is specified at 2 μm and the precision of the limit switches < 1 μm. The uncertainty associated with the reproducibility of the measured range in water, σ_R, can be estimated by $a/\sqrt{3}$ [84] with a the maximum difference between the $R_{80\%}$ in the measured Bragg curve in water used as reference for the sample measurement and the $R_{80\%}$ in the previous and following measured Bragg curves in water. The relative stopping power is given by the ratio t_w/t_m which equals $(t_m - \Delta R_s)/t_m$ with t_w the water equivalent thickness of the sample, t_m the material thickness and ΔR_s the measured range difference of the sample

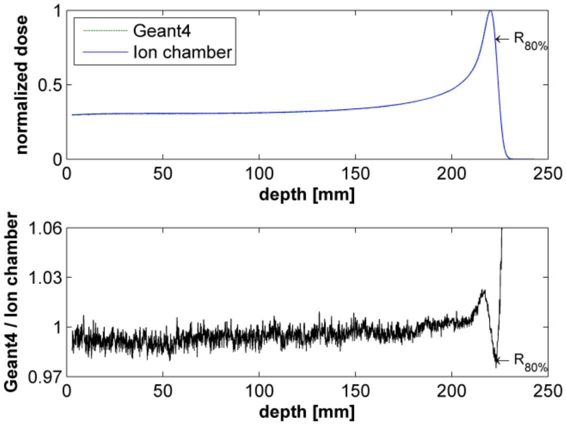

Figure 4.2. Comparison between Geant4 simulated and ionisation chamber measured depth dose distributions in water for experiment 1. The two curves nearly overlap (top figure) and the difference between the Geant4 simulated and the experimentally measured depth dose distribution is within 3% up to a depth corresponding to the range ($R_{80\%}$).

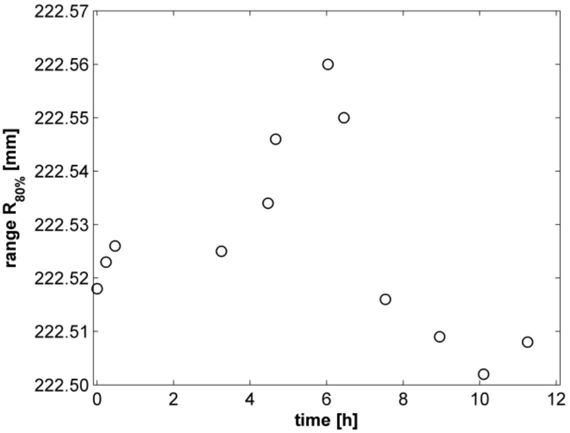

Figure 4.3. The range ($R_{80\%}$) of 189.3 MeV protons in water as a function of time during one of the experiments.

measurement relative to water. The uncertainty in the determined relative stopping powers depends on ΔR_s and t_m and their uncertainties. With the described setup, an uncertainty associated with the reproducibility of the measured range in water $\sigma_R < 31$ μm has been achieved in all four performed experiments, leading to an uncertainty in $\Delta R_s < 43.8$ μm. From thickness measurements with a micro meter, RSPs have been determined with an uncertainty < 0.4% for 32 samples with a water equivalent thickness of about 2 cm as presented in chapter 3. To achieve even lower uncertainty levels, a higher energy stability of the proton beam is needed to reduce the contribution of σ_R and the sample thickness should be known with micrometre accuracy for samples with thicknesses in the order of 1 to 2 cm. Increasing the thickness of the samples would highly contribute to a reduction in the uncertainty in the relative stopping power. This would, however, result in an RSP being averaged over a large energy range and different multiple Coulomb scattering as compared to the situation of water only. For soft tissues with an RSP around 1 these effects might be small but for lung, bone and metals they are pronounced.

4.3.3 Comparison with other experimental setups

Different methods to measure relative stopping powers have been presented in literature. Schaffner and Pedroni[18] measured depth dose profiles using range shifter plates to degrade the proton beam energy. The water equivalent thickness of the range shifter plates was 2.3 mm which limits the spacing of the Bragg curve measurements. With this setup they expected an accuracy of the measured range shift of ±0.1 range shifter plate corresponding to an accuracy of 0.2% in the RSP measurement for 10 cm thick tissue samples. For samples with a thickness of 2 cm this accuracy would amount to about 1%. Witt *et al.*[85] have employed the PTW Peakfinder (PTW, Freiburg, Germany) for residual range measurements with a specified uncertainty in the residual range measurement of 50 μm. For 7 cm thick samples they estimated the uncertainty in the measured RSP to be < 0.3%. Jäkel *et al.*[86] and Hünemohr *et al.*[52] have used a slightly different design of the PTW Peakfinder and reported an accuracy in the measured relative water equivalent shifts of Bragg peak positions for samples between 1 and 3.5%.

The accuracy in determining relative proton stopping powers from residual range measurements achieved with our water phantom (uncertainty < 0.4% for samples with 2 cm water equivalent thickness) is better than the other presented systems. The large sample thicknesses (about 10 cm) used in the studies of Schaffner and Pedroni[18] and Witt *et al.*[85] strongly reduce their uncertainty in the relative stopping power measurements but have disadvantages as described in the preceding section.

4.3.4 Uncertainty in relative stopping power calculation

SECT and DECT methods often use the approximation of the Bethe-Bloch formula given in eq. (7) for calculation of relative stopping powers. In the approximation of the stopping power, the shell correction and higher order corrections have not been taken into account. We estimated the shell contribution -1.5% at maximum and the Barkas correction less than 1% where both errors partially cancel out because of their opposite signs[72]. The accuracy of the approximation of the Bethe-Bloch formula (eq. (6)) has been estimated at 1-1.5%. The influence of the different correction terms is reduced when the stopping power relative to water is used for the calculations. We have estimated the impact of the correction terms on the relative stopping power by comparing the RSPs derived from Geant4 simulations, which include shell and higher order corrections, to RSPs calculated with eq. (7). For RSPs calculated with eq. (7), mean excitation energies have been calculated with Bragg's additivity rule except for $\langle I_w \rangle$ (78 eV). This corresponds to the mean excitation energies used in the Geant4 simulations. The differences in RSPs between Geant4 simulations and calculations with eq. (7) due to the correction terms are less than 0.3% for the 32 materials listed in table 3.1.

The accuracy of the stopping power of the material and that of water is of importance for accurate calculation of RSPs. To verify the calculated stopping power of water, an absolute energy dependent stopping power measurement should be performed. For experimental determination of elemental $\langle I \rangle$ values, preferably experimental data derived at higher energies should be used where the contribution of the shell corrections to the stopping power is small[87].

The differences in RSPs between Geant4 simulations and experimental values are in the order of 1-2% (table 3.2). The largest contributions to these differences are possibly the uncertainties in elemental mean excitation energies and Bragg's additivity rule and an uncertainty in the mean excitation energy of water. In addition, the accuracy of the Bethe-Bloch theory for prediction of proton stopping powers is not precisely known.

4.4 Conclusions

We have developed a water phantom for accurate depth dose measurements. The uncertainty associated with the reproducibility of the measured range in water is determined by the energy stability of the proton beam. The instrument allows relative proton stopping powers to be measured with an accuracy better than 0.4% by measuring range differences in water for samples with a water equivalent thickness of about 2 cm. This achieved accuracy is sufficient for experimental validation of relative stopping powers predicted by computed tomography or Geant4 Monte Carlo simulations for particle therapy.

Chapter 5

Dual energy CT outperforms single energy CT for relative proton stopping power prediction

Abstract

The non-patient specificity of the single energy computed tomography (SECT) stoichiometric calibration method for determination of relative proton stopping powers (RSPs) is a limiting factor for the accuracy that can be achieved in proton therapy treatment planning. In this study we assess the validity of this SECT method and compare its accuracy with dual energy CT (DECT) based prediction of RSPs.

For both SECT and DECT, RSP images have been derived from the measured CT data of 32 materials and 17 bovine tissues. RSPs predicted by SECT and DECT have been compared to RSPs experimentally determined from measurements with 149 MeV protons.

The SECT predicted RSPs for the 32 materials deviate -21 to 16% (difference -3.0±7.8%) from experimental values. The DECT predicted RSPs are predominantly within 3.5% (difference 2.0±2.2%) of the experimental RSPs. The differences between the SECT and DECT predicted RSPs for the 17 bovine tissues are small except for the lung, adipose and bone samples. The differences are within 3.6% (difference 1.3±1.3%) and 3.3% (difference 2.3±0.5%) of experimental values, for SECT and DECT respectively except for bone. The partial volume averaging between air and bone in the two bone samples results in large deviations of 19 and 24% for SECT. The DECT predicted RSPs for the two bone samples deviate 5.4 and 5.3% from experimentally determined RSPs.

The proposed DECT method provides patient specific tissue RSPs while the SECT calibration method provides generic tissue RSPs. The DECT method is more accurate in prediction of RSPs for a wide range of materials and tissues than the SECT calibration method.

5.1 Introduction

In treatment planning for proton therapy, single energy computed tomography (SECT) stoichiometric calibration methods are used to determine stopping powers of tissues relative to that of water (RSPs). In analytical treatment planning systems the RSP is derived from the CT number with a calibration curve based on tissue substitute measurements or calculations for average tissue compositions[18,34]. Monte Carlo dose calculation requires the mass density and elemental mass fractions which can be assigned to CT number bins based on modelling of average tissue compositions and densities[19]. The linear attenuation coefficient measured in CT depends on the electron density and electronic cross section which is dependent on the elemental composition. Due to this twofold dependence, materials with different composition and density can have the same CT number in a single energy CT scan. This shows the main disadvantage of SECT based methods, namely their lack of specificity. In addition, beam hardening affects the measured CT numbers which can cause deviations from the SECT calibration curve. Methods based on dual energy CT (DECT) typically derive the electron density and an effective atomic number using a parameterization of the electronic cross section[21,35,37,42,51,52,54,88]. By iteratively changing the spectral weighting of this parameterization using the obtained effective atomic number and electron density, high accuracy electron densities can be derived[51]. From the relative electron densities and a relation between the effective atomic number and mean excitation energy, relative proton stopping powers can then be determined.

A theoretical comparison between SECT and DECT for prediction of RSPs has been performed by Yang *et al.*[23]. They have shown that the SECT calibration method is more susceptible to variations in composition and density of human tissue. Only a limited number of studies have assessed the accuracy of the SECT calibration method for animal tissue samples. Schaffner and Pedroni[18] measured large animal tissue samples combined in a Perspex box with a proton pencil beam. They estimated the range error due to the calibration curve at 1.8% for bone and 1.1% for soft tissue. For artificial bolus materials range errors up to 3% of the bolus thickness have been estimated[18]. Rietzel *et al.*[89] measured animal tissues with a carbon ion pencil beam. In their study the measured CT numbers as well as the residual ranges have been corrected for air in the tissue sample. With these corrected data differences between SECT predicted and measured water equivalent path lengths up to 2.6% have been reported.

In this study we present a comparison of relative proton stopping power predictions from SECT and DECT with experimental data for a large set of well characterized materials and bovine tissues.

5.2 Methods

The RSPs derived from SECT and DECT have been compared to RSPs measured with 149 MeV protons (at the entrance of the sample) at the AGOR cyclotron[63]. The RSPs have been experimentally determined for 32 materials with known composition and density and for 17 bovine tissues.

5.2.1 Single energy CT calibration for RSP calculation

The SECT based approach described by Schneider *et al.*[19] has been followed to calculate CT numbers for 81 average tissues[17,39]. Values for the scanner and energy specific calibration coefficients k_1 and k_2 have been determined from SECT data of the Gammex 467 tissue characterization phantom (Gammex Inc., Middleton, WI, USA) measured on a dual source CT (DSCT) system (SOMATOM Force, Siemens Medical Solutions, Forchheim, Germany). The SECT data has been acquired at 120 kV (147 mAs) ($\mathrm{CTDI_{vol}}$ = 9.9 mGy) using an abdomen protocol in spiral mode with a collimation of 192x0.6 mm. The data has been reconstructed with a Qr40 strength 5 advanced modeled iterative reconstruction (ADMIRE) kernel with a slice thickness of 1 mm. From the measured average CT numbers of the 16 Gammex materials the coefficients k_1 and k_2 have been determined using the *lsqnonlin* function in MATLAB (MATLAB 8.3, The MathWorks Inc., Natick, MA, USA). A least squares solution has been found where $k_1 = 1.0377\text{x}10^{-5}$ and $k_2 = 2.4736\text{x}10^{-5}$ ($R^2 = 0.9998$). With these coefficients the calculated CT numbers for the 16 Gammex materials were found to be within 13 Hounsfield units (HU) of the measured CT numbers. Subsequently, CT numbers for the average tissues have been calculated using the derived coefficients. Relative proton stopping powers (RSPs) for the average tissues have been calculated using the approximation

$$\frac{S_m}{S_w} = \frac{\rho_e^m}{\rho_e^w}\left\{\frac{\ln\left(\frac{2m_e c^2\beta^2}{1-\beta^2}\right) - \beta^2 - \ln\langle I_m\rangle}{\ln\left(\frac{2m_e c^2\beta^2}{1-\beta^2}\right) - \beta^2 - \ln\langle I_w\rangle}\right\}$$

where ρ_e^m/ρ_e^w is the relative electron density, $m_e c^2$ the electron rest mass with c the speed of light in vacuum, $\beta = v/c$ with v the proton velocity, $\langle I_m\rangle$ the mean excitation energy of the material calculated with Bragg's additivity rule and $\langle I_w\rangle$ the mean excitation energy of water for which a value of 78 eV has been adopted from Sigmund *et al.*[67]. The RSPs of the average tissues have been calculated at a proton energy of 143.5 MeV which corresponds to the average energy in our samples with a water equivalent thickness of about 2 cm at an entrance energy of 149 MeV. Figure 5.1 presents the calibration curve used for the SECT analysis which has been composed of

4 linear fits of the tissue data in HU intervals of [-1024, -200] lung, [-100, -20] adipose, [5, 75] organs and muscle and [135, 3000] bone[18]. The HU intervals have been connected by linear interpolation of the corresponding RSPs. CT images of the samples acquired at 120 kV have been converted to RSP images using this CT number to RSP calibration curve.

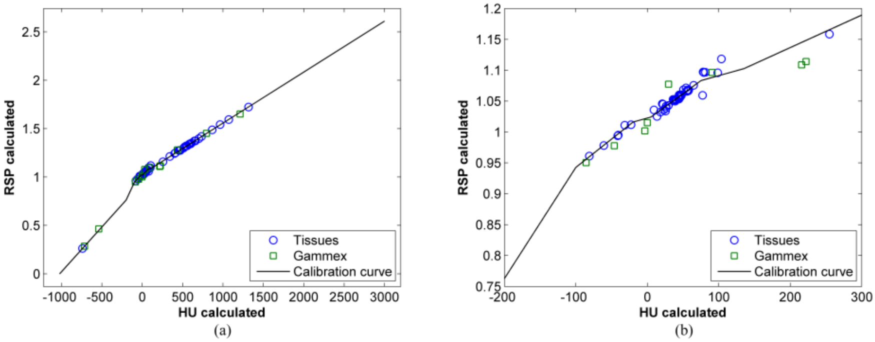

(a) (b)

Figure 5.1. (a) Single energy CT calibration curve based on the average tissues[17,39] which relates calculated CT numbers (HU)[19] to calculated relative stopping powers (RSPs). (b) Enlarged view of the fits to the adipose, organs and muscle and bony tissues.

5.2.2 Dual energy CT for RSP calculation

Dual energy CT provides linear attenuation coefficients derived from measured CT numbers at two different spectral energy distributions (high and low kV setting) for each voxel. Using the method presented by van Abbema *et al.*[51] (chapter 2) effective atomic number and electron density images have been derived from DECT data. The effective atomic number images have been calibrated for not adequately corrected beam hardening in the CT reconstruction process (chapter 3). A relation has been established between this effective atomic number and the logarithm of the mean excitation energy (chapter 3). Relative stopping power images have been determined from the images of the relative electron density and the mean excitation energy derived from the effective atomic number at a proton energy of 143.5 MeV and with an ICRU recommended value for $\langle I_w \rangle$ of 78 eV[67]. Alternatively, a value for $\langle I_w \rangle$ of 69 eV could have been selected which corresponds to the value obtained with Bragg's additivity rule used by the SECT and DECT methods. This would lead to a reduction in the RSPs predicted by SECT and DECT of 1.5%.

5.2.3 Comparison SECT and DECT

The SECT and DECT data of the sample materials and bovine tissues has been acquired on a DSCT system (SOMATOM Force). Inside a Gammex 467 tissue characterization phantom (diameter 33 cm) the different sample materials (diameter 2.85 cm) have been distributed over the phantom in different configurations (figure 5.2a). From a variety of bovine organs and tissues 23 different tissue samples have been prepared. The two bone samples have been obtained from pulverizing a bovine shoulder blade. A cortical bone sample contains the bone cortex fragments while a mixed bone sample includes cortical and cancellous bone. The mass densities of these bone samples are smaller than tabulated densities for bone[39]. The influence of these differences on the predicted RSPs is addressed in the discussion. The tissues have been pressed in cylindrical dishes (diameter 8.7 cm, thickness around 2 cm) after which they were vacuum sealed in microchannel bags to conserve and preserve their thickness and shape. A CT water phantom (diameter 30 cm) has been developed which centrally aligns the tissues (figure 5.2b).

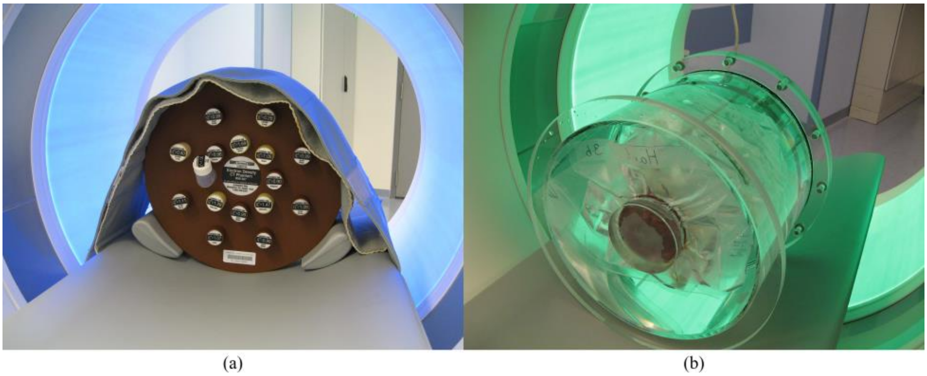
(a) (b)

Figure 5.2. CT scan setup of the (a) Gammex phantom with different insert configurations (shown is the default configuration) and (b) CT water phantom with tissues vacuum sealed in cylindrical dishes and microchannel bags.

The phantoms have been scanned with SECT at 120 kV (147 mAs) using the same settings as applied for the calibration scan. With DECT the phantoms have been scanned using a clinical 90 kV / 150 kV Sn dual energy abdomen virtual noncontrast (VNC) protocol in spiral mode with a collimation of 64x0.6 mm with 266 mAs (90 kV) and 166 mAs (150 kV Sn) ($CTDI_{vol}$ = 15.5 mGy). For reconstruction of both SECT and DECT data, a Qr40 strength 5 ADMIRE kernel and a slice thickness of 1 mm have been used for a field of view of 35 cm.

From the reconstructed SECT and DECT data central slices of the sample materials have been selected for which RSP images have been calculated. The mean and standard deviation in the RSPs have been determined by drawing circular regions of interest (ROIs) in the RSP images derived from SECT and DECT, respectively.

For the bovine tissues, circular ROIs have been selected with a diameter of 5.3 mm at the center of the sample in each slice of the tissue. The diameter of 5.3 mm corresponds to the diameter of the electrode in the Markus ionisation chamber used for the proton measurements. The ROIs of all slices in the tissue have been combined to obtain a cylindrical volume of interest (VOI) with a thickness around 20 mm (depending on the tissue thickness). For each voxel in the VOI, RSPs have been calculated for SECT and DECT after which for each slice the mean and standard deviation have been calculated. The mean RSP of the tissue has been derived from the RSPs in all slices of the tissue. Based on analysis of the CT images and CT number profiles with depth in the tissue, 6 of the 23 bovine tissues have been excluded from further analysis due to their inhomogeneity.

5.2.4 Proton relative stopping power measurements

Experimental RSPs for the sample materials and bovine tissues have been determined from measured residual ranges relative to water and sample thicknesses (chapter 3). The proton measurements of the bovine tissues have been performed within 36 hours of the CT measurements and within 48 hours from slaughter. During the proton and CT experiments the temperature of the water in which the tissue samples have been measured has been stabilized at 21ºC.

5.3 Results and discussion

5.3.1 SECT versus DECT for sample materials

The experimental RSPs of the 32 materials have been derived with a 1σ uncertainty < 0.4% (most materials 0.2%) including an uncertainty < 31 µm in the range $R_{80\%}$.

The RSP images derived from SECT and DECT for a setup of the Gammex phantom including an aluminium insert (figure 2.5 and table 2.3) are shown in figure 5.3. Both SECT and DECT provide RSP images of comparable image quality. Missing voxels which were visible for 100 kV / 140 kV Sn DECT[51] (chapter 2) are not present in figure 5.3b, except for air. The relative differences of SECT and DECT predicted RSPs with respect to the experimentally determined RSPs for the 32 materials are presented in table 5.1 and figure 5.4. The 32 materials consist of tissue substitutes (No. 1-6), analytical standards, silicone oil and potassium chloride solutions (No. 7-23) and carbon, polymers, a metal and a ceramic (No. 24-32). For the tissue substitutes the relative differences between SECT predicted and experimental RSPs are -0.4 to 2.7%. The relative differences for the analytical standards and potassium chloride solutions range from -11 to 10%. The SECT predicted RSP of silicone oil, used in treatment of ocular tumours, deviates 16% from the experimental RSP, slightly larger than the difference measured by Weber *et al.*[70]. For material No. 24-32 the relative differences are between -21 and -1%. With DECT, RSPs have been predicted for the tissue substitutes with relative differences between -0.1 and 1.7% with respect to experimental RSPs (except for the inhomogeneous LN-450). For the analytical standards, silicone oil and potassium chloride solutions the differences are between 0 and 3.5%. The relative differences for the polymers No. 25-29 are -0.2 to 1.7%. Carbon, Teflon, aluminium and Al_2O_3 deviate 4 to 9% due to a systematic deviation from the relation between Z' and $\ln\langle I\rangle$ for these materials (chapter 3). The large differences between the SECT predicted and experimental RSPs are not exclusively seen for materials containing high Z elements (No. 19-23, 31 and 32) but also for materials composed of C, H and C, H, O (No. 7-14, 18 and 28). This demonstrates the sensitivity of the stoichiometric calibration method for variations in density and composition of tissues with respect to the average tissues used for the calibration curve.

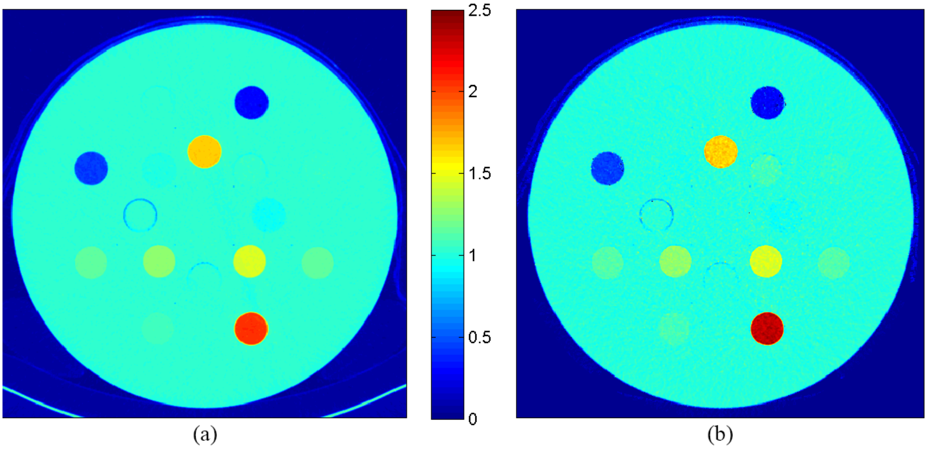

(a) (b)

Figure 5.3. Relative stopping power images at 143.5 MeV derived from (a) single energy CT and (b) dual energy CT with a slice thickness of 1.0 mm for a setup of the Gammex phantom including an aluminium insert. The CT couch is outside the reconstruction field of view of the 150 kV Sn dataset (B-tube) and therefore not visible on the dual energy CT based RSP image.

With the calibration curve (figure 5.1) an RSP of 1 is assigned to a measured CT number of -38 HU as also visible in figure 1 of Schaffner and Pedroni[18]. This will not correctly account for water with an RSP of 1 and a CT number around 0 HU.

Correspondingly, the RSP derived from SECT for water deviates 2.4% from the experimental value. The SECT method performs quite well (within 3%) for the Gammex tissue substitutes which approximate the average tissues used for constructing the calibration curve.

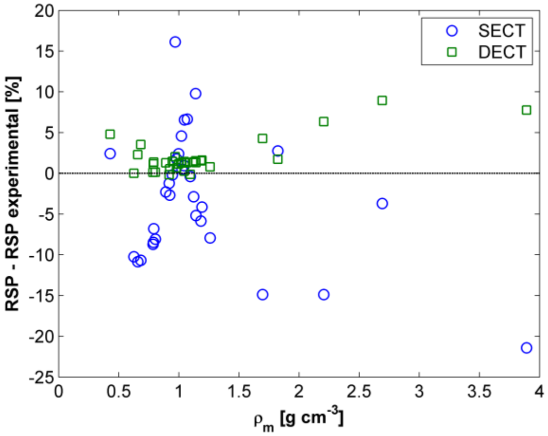

Figure 5.4. Relative difference of relative stopping powers (RSPs) derived from single energy CT (SECT) and dual energy CT (DECT) with respect to experimental RSPs for 143.5 MeV protons (average in sample). The differences are given as a function of the mass density (ρ_m) for the 32 sample materials specified in table 5.1.

Table 5.1. Mass densities ρ_m, relative electron densities $\rho_{e,m}{}'/\rho_{e,w}$ measured with DECT and relative differences with calculated values for 32 materials. Calibrated effective atomic numbers Z'_{cal} from DECT determined values for Z'. Relative stopping powers (RSPs) derived from SECT and DECT compared to the experimental RSPs determined with uncertainty < 0.4% at a proton energy of 143.5 MeV (average in sample).

No.	Material	ρ_m [g cm^{-3}]	$\rho_{e,m}{}'/\rho_{e,w}$ meas	$\rho_{e,m}{}'/\rho_{e,w}$ meas-calc [%]	Z'_{cal}	RSP SECT	RSP DECT	RSP Exp	RSP SECT-Exp [%]	RSP DECT-Exp [%]
1	LN-450 Lung	0.428	0.431	3.2	7.52	0.431	0.441	0.421	2.4	4.8
2	AP6 Adipose	0.946	0.934	0.5	6.23	0.949	0.965	0.951	-0.2	1.5
3	BR-12 Breast	0.981	0.965	0.5	6.96	0.996	0.986	0.979	1.7	0.7
4	Solid Water M457	1.045	1.019	0.2	7.38	1.043	1.036	1.033	1.0	0.3
5	LV1 Liver	1.095	1.067	0.1	7.55	1.080	1.083	1.084	-0.4	-0.1
6	SB3 Cortical Bone	1.823	1.712	0.7	14.01	1.666	1.649	1.622	2.7	1.7
7	n-Pentane	0.626	0.654	-0.6	6.01	0.614	0.684	0.684	-10.2	0.0
8	n-Hexane	0.659	0.689	-0.2	5.67	0.639	0.733	0.717	-10.9	2.2
9	n-Heptane	0.683	0.720	0.8	5.37	0.661	0.766	0.740	-10.7	3.5
10	Methanol	0.791	0.803	0.1	6.54	0.760	0.827	0.816	-6.9	1.3
11	Ethanol	0.788	0.804	0.1	6.24	0.752	0.832	0.822	-8.5	1.2
12	Propan-1-ol	0.805	0.817	-0.6	6.39	0.773	0.842	0.841	-8.1	0.1
13	Propan-2-ol	0.785	0.798	-0.5	6.36	0.750	0.823	0.822	-8.8	0.1
14	Oleic acid	0.892	0.900	-0.1	6.10	0.899	0.932	0.920	-2.3	1.3
15	Ethyl acetoacetate	1.026	0.992	-0.4	6.67	1.008	1.016	1.003	0.5	1.3
16	Water	0.998	0.996	-0.4	7.39	1.024	1.011	1.000	2.4	1.1
17	Polyethylene glycol 200	1.123	1.100	-0.4	6.56	1.082	1.130	1.115	-3.0	1.3
18	Glycerol	1.260	1.221	-1.1	6.80	1.140	1.248	1.238	-7.9	0.8
19	Silicone oil Siluron 5000	0.970	0.948	0.4	10.75	1.076	0.945	0.926	16.2	2.1
20	Potassium Chloride 4.01%	1.021	1.017	-0.1	8.26	1.060	1.027	1.014	4.5	1.3
21	Potassium Chloride 7.71%	1.046	1.036	-0.2	9.31	1.093	1.040	1.025	6.6	1.5
22	Potassium Chloride 11.13%	1.070	1.056	0.0	10.11	1.113	1.057	1.043	6.7	1.3
23	Potassium Chloride 20.03%	1.139	1.114	0.2	11.85	1.191	1.101	1.084	9.9	1.6

Table 5.1. Continued. Mass densities ρ_m, relative electron densities $\rho_{e,m}'/\rho_{e,w}$ measured with DECT and relative differences with calculated values for 32 materials. Calibrated effective atomic numbers Z'_{cal} from DECT determined values for Z'. Relative stopping powers (RSPs) derived from SECT and DECT compared to the experimental RSPs determined with uncertainty < 0.4% at a proton energy of 143.5 MeV (average in sample).

No.	Material	ρ_m [g cm^{-3}]	$\rho_{e,m}'/\rho_{e,w}$ meas	$\rho_{e,m}'/\rho_{e,w}$ meas-calc [%]	Z'_{cal}	RSP SECT	RSP DECT	RSP Exp	RSP SECT-Exp [%]	RSP DECT-Exp [%]
24	Carbon graphite	1.696	1.536	0.4	6.21	1.292	1.583	1.518	-14.9	4.3
25	UHMWPE	0.923	0.958	0.8	5.74	0.968	1.000	0.994	-2.6	0.6
26	Polypropylene	0.919	0.946	0.0	6.37	0.967	0.977	0.979	-1.2	-0.2
27	Nylon 6.6-101	1.142	1.124	-0.4	6.14	1.089	1.163	1.148	-5.1	1.3
28	PMMA	1.183	1.151	0.0	6.42	1.099	1.186	1.168	-5.9	1.5
29	Polycarbonate	1.192	1.128	-0.5	6.50	1.093	1.159	1.140	-4.1	1.7
30	Teflon	2.205	1.885	-1.3	8.30	1.522	1.902	1.788	-14.9	6.4
31	Aluminium AlMgSi$_1$	2.691	2.383	1.8	13.27	2.050	2.319	2.129	-3.7	8.9
32	Al_2O_3 99.7%	3.892	3.452	0.2	10.61	2.513	3.446	3.198	-21.4	7.8

5.3.2 SECT versus DECT for tissues

The relative differences between SECT and DECT predicted and experimentally determined RSPs of the 17 tissues are presented in table 5.2. For most tissues the differences between SECT and DECT are small except for lung, adipose and the bone samples. The relative differences with respect to experimental RSPs are within 3.6% and 3.3% (except for bone) respectively, for SECT and DECT. The SECT and DECT analysis for adipose and mixed bone is visualised in figure 5.5. For the bone samples the differences are 19 and 24% for SECT and 5.4 and 5.3% for DECT. Due to the powderlike structure of the bone segments air is present in the bone samples which affects the measured CT numbers and mass densities. The partial volume averaging between bone and air is equal for both the SECT and DECT images but with DECT a reliable effective atomic number and electron density can be derived from the measured CT numbers. This enables to distinguish materials based on their electron density and effective atomic number (e.g. compare adipose and bone in table 5.2). With the SECT method an RSP has been assigned based on the calibration curve which can introduce errors for tissues with different CT numbers than expected due to a different mass density or composition. Since human tissues can vary in mass density and composition[17] this indicates a main limitation of the SECT method. Yang *et al.*[23] showed from theoretical calculations that their DECT method is insensitive to density variations while the stoichiometric SECT method under these conditions exhibits large differences with respect to calculated RSPs. Besides they found large deviations for SECT when mixing a low density tissue with a high density tissue. They concluded that partial volume averaging has only limited impact on the DECT predicted RSPs. This is also observed in our study in the case of partial volume averaging between air and bone. In DECT, the ratio of linear attenuation coefficients from which the effective atomic number is derived is independent of the mass density. The derived electron density is proportional to the mass density and the stopping power is proportional to the electron density. With DECT the effective atomic number and the electron density can be determined for each material or tissue separately and a specific RSP can be assigned. In the SECT method a change in CT number with respect to the value expected on basis of the calibration curve due to a composition or density change leads to allocation of a different tissue with a different RSP.

The systematic positive differences between DECT predicted and experimental RSPs of the tissues reflect the positive differences found for the sample materials. If consistent with the DECT method Bragg's additivity rule is used for calculation of the mean excitation energy for water, the obtained value of 69 eV leads to a decrease of RSPs by 1.5%. The systematic deviation for DECT then reduces to differences within 2% of experimental values for 27 of the 32 materials and 15 of the 17 tissues.

For the proton experiment with the bovine tissues the uncertainty in the $R_{80\%}$ in water is < 40 µm and is only a minor contribution to the uncertainty in the experimental RSPs of the tissues. This uncertainty is dominated by inhomogeneities in the tissues, in particular small air cavities. A range difference of 0.5 mm due to air inside the tissue brings about a difference in RSP in the order of 2.7%. This emphasizes the sensitivity of the measurement methodology for determining RSPs. Therefore, inhomogeneous tissues with air cavities have been excluded from the analysis. Rietzel *et al.*[89] corrected their experimental data for air mainly on the borders of the tissue samples. We consider correcting for air cavities doubtful since the RSP measurement is highly sensitive for air and the method for air correction can strongly influence the resulting RSPs. To improve future measurement of tissues, we suggest to measure larger tissues inside water where the air cavities fill with water. In the analysis scatter effects of the protons in the field in and out the VOI are assumed to cancel out. Alternatively, measurements could be performed with a pencil beam and a large ionisation chamber where the measured depth dose distribution corresponds to a path of a small beam and might be less sensitive to lateral tissue inhomogeneities. Proton radiography can potentially provide 2D stopping power images which can be compared to the 3D images from DECT integrated over the tissue thickness. This could give insight in the influence of tissue inhomogeneities on the measured RSP.

Schaffner and Pedroni[18] estimated the accuracy of their SECT calibration curve for determination of RSPs at 1.8% for bone and 1.1% for soft tissue. Our results show larger deviations for SECT predicted RSPs with respect to experimental values. Careful reconsideration of the uncertainty associated with the determination of RSPs from clinical SECT imaging seems desirable.

Table 5.2. Estimated mass densities ρ_m, DECT measured relative electron densities $\rho_{e,m}{}'/\rho_{e,w}$ and calibrated effective atomic numbers Z'_{cal} of 17 bovine tissues. Relative stopping powers (RSPs) derived from SECT and DECT are compared to experimentally determined RSPs at a proton energy of 143.5 MeV (average in tissue).

No.	Tissue	ρ_m [g cm^{-3}]	$\rho_{e,m}{}'/\rho_{e,w}$ meas	Z'_{cal}	RSP SECT	RSP DECT	RSP Exp	RSP SECT-Exp [%]	RSP DECT-Exp [%]
1	liver (1)	1.151	1.063	7.24	1.070	1.082	1.051	1.8	2.9
2	kidney	1.096	1.035	7.26	1.057	1.054	1.020	3.6	3.3
3	heart (1)	1.042	1.043	7.28	1.059	1.061	1.041	1.7	1.9
4	lung	0.628	0.452	7.18	0.435	0.457	0.444	-2.0	2.9
5	muscle	1.035	1.052	7.09	1.061	1.073	1.046	1.4	2.6
6	thymus	1.058	1.036	7.06	1.051	1.057	1.030	2.0	2.6
7	heart thymus	0.997	0.979	6.34	0.995	1.009	0.985	1.0	2.4
8	tongue	1.047	1.010	6.79	1.026	1.033	1.010	1.6	2.3
9	brain	1.083	1.030	7.27	1.047	1.048	1.031	1.6	1.6
10	spleen	1.112	1.051	7.55	1.074	1.067	1.049	2.4	1.7
11	adipose	1.009	0.953	5.69	0.959	0.996	0.970	-1.1	2.7
12	bladder	1.093	1.026	7.18	1.044	1.047	1.030	1.4	1.7
13	bone cortical	1.068	1.068	13.67	1.222	1.034	0.982	24.4	5.3
14	bone mixed	1.065	1.149	13.22	1.261	1.119	1.062	18.7	5.4
15	liver (2)	1.043	1.069	7.26	1.078	1.088	1.063	1.4	2.4
16	heart (2)	1.218	1.048	7.17	1.059	1.068	1.047	1.1	2.0
17	thyroid	1.035	1.029	7.20	1.043	1.048	1.029	1.4	1.8

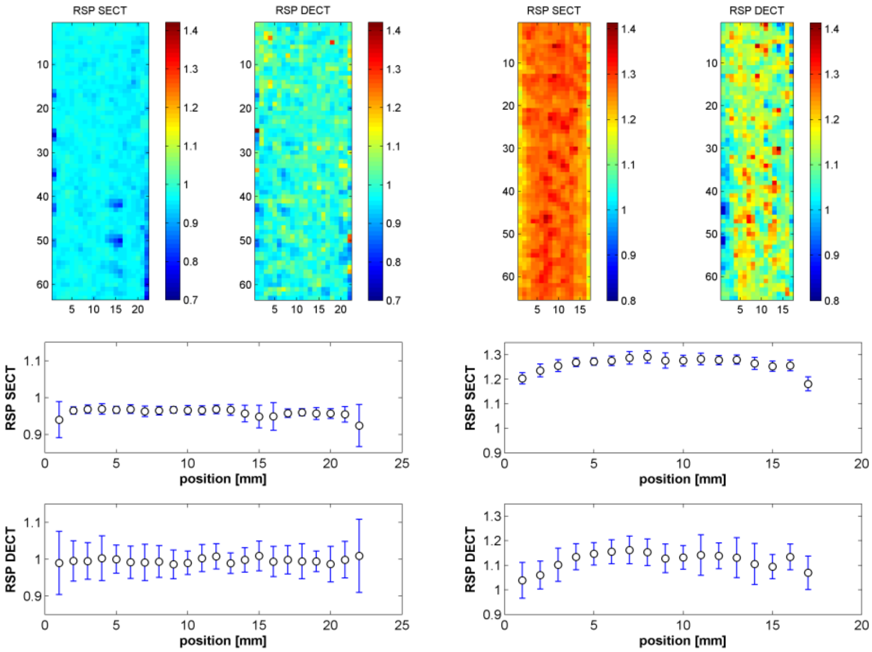

(a)

(b)

Figure 5.5. Relative stopping powers (RSPs) for (a) adipose (No. 11) and (b) mixed bone (No. 14) determined from SECT and DECT images by selecting regions of interest (ROIs) in each slice. Top images are 2D mappings of the 3D volumes of interest (VOIs) where the vertical axis represents the subsequent voxel numbers in the circular ROI in each slice (xy plane) and the horizontal axis represents the slice position in the sample [mm] (z plane). The bottom profiles visualise the mean and standard deviation in the RSP of each slice.

5.4 Conclusions

The accuracy of relative stopping powers derived from SECT and DECT, respectively, has been evaluated by comparing them to experimentally determined values. The relative difference between SECT predicted and experimentally determined RSPs of 32 materials range from -21 to 16% (difference -3.0±7.8%) while the DECT predicted RSPs are mainly within 3.5% (difference 2.0±2.2%) of the experimental values. The SECT predicted RSPs vary considerably while the DECT predicted RSPs show a systematic positive deviation which might be explained by the choice of mean excitation energy for water. For the 17 bovine tissues the differences of the SECT and DECT predicted RSPs with respect to experimental values are within 3.6% (difference 1.3±1.3%) and 3.3% (difference 2.3±0.5%) respectively, except for the bone samples. Partial volume averaging between air and bone in the two bone samples leads to large deviations for SECT of 19 and 24% while DECT predicted RSPs deviate 5.4 and 5.3% from experimental values. For clinical SECT imaging for treatment planning a high resolution (slice thickness ≤ 1 mm) could improve the accuracy of the RSP and range prediction. A high resolution restricts the partial volume averaging and can visualize small air volumes which cause range shifts. The applicability of the SECT stoichiometric calibration method is restricted to materials which closely approximate the average tissues used for the calibration in composition and density. This is in all probability not the case for real human tissues. The DECT method provides more accurate RSPs for a wide range of materials and tissues and is much less sensitive to partial volume averaging. DECT can provide patient specific tissue RSPs while SECT provides generic tissue RSPs. It is of clinical importance to reconsider the uncertainty introduced by using the SECT calibration method for prediction of tissue RSPs. The improvement which can be achieved with the proposed DECT method will improve the conformity between planned and delivered dose distribution and thus should lead to clinical benefit.

Chapter 6

Summary and Outlook

6.1 Introduction

In this thesis the possibilities to derive accurate proton stopping powers from dual energy computed tomography (DECT) images of a patient are explored. These stopping powers can be used in proton therapy treatment planning to predict the energy transfer of the protons to the tissue and the corresponding absorbed energy (dose). The DECT method has been assessed in detail and compared to a single energy CT (SECT) method that uses a stoichiometric calibration and is the current clinical standard. In this assessment and comparison, high accuracy proton range measurements provided experimental ground truth proton stopping powers relative to that of water for a wide range of materials and animal tissues.

6.2 Dual energy CT tissue characterization

DECT provides linear attenuation coefficients for two photon spectra and thus results in extra information compared to SECT using only one photon spectrum. This advantage of DECT can be exploited by using a theoretical framework, including an accurate parameterization of the photon-electron interaction cross section, which describes the dependence of the linear attenuation coefficient on the electron density and atomic number as a function of photon energy. Using spectral weightings specific for the tube potentials applied for imaging with a particular CT system, the theoretical framework allows solving for the effective atomic number and electron density from the two measured linear attenuation coefficients. This is a natural parameterization of this twofold dependence of the linear attenuation coefficient. By implementing an iterative optimization procedure which changes the spectral weighting of the parameterization of the cross section using the obtained effective atomic number and electron density, electron densities are determined with high accuracy (~1%). The derived electron density has a clear physical meaning and is directly relevant for proton dose calculations. The effective atomic number is more difficult to interpret. This number incorporates the Z dependence of the photon interaction processes. A systematic deviation between measured and calculated effective atomic numbers has been observed for materials of known composition. This deviation is attributed to a phenomenological beam hardening correction for water in the CT reconstruction process.

6.3 Proton stopping powers for dose calculation

The tissue electron density, which can be accurately determined from DECT, provides the largest contribution to the proton stopping power. In addition, the proton stopping power depends on the mean excitation energy of the tissue. The effective atomic number corrected for the water beam hardening correction correlates well with the mean excitation energy. In this study we used an empirical relation to convert effective atomic numbers from DECT into mean excitation energies. With this relation the values of the logarithm of the mean excitation energy $\ln\langle I\rangle$ obtained from the effective atomic numbers are for the average tissue compositions[17,39] within 1% and for most materials used in our measurements within 3% of values calculated with Bragg's additivity rule. A 3% difference in $\ln\langle I\rangle$ corresponds to a 1.7% difference in relative stopping power. Using the electron densities and mean excitation energies derived from DECT images, relative proton stopping powers have been calculated.

High accuracy measurements of proton depth dose distributions have been performed with a water phantom. The measured range in water has been determined with an uncertainty < 0.03 mm. The measured depth dose distributions correspond well with Geant4 Monte Carlo simulated depth dose distributions. An improved correspondence has been found as compared to the measurements and simulations presented by Boon *et al.*[90]. This could be due to the selected physics list or improvement of the physics in the Geant4 Monte Carlo code.

Relative proton stopping powers have been determined from depth dose measurements with an uncertainty < 0.4%. This uncertainty can be further reduced by a higher energy stability of the proton beam and using samples with a thickness larger than the approximately 20 mm water equivalent thickness used in our experiments. However, an increased sample thickness will lead to averaging of the relative stopping power over a larger energy range due to its energy dependence and different multiple Coulomb scattering as compared to the situation for water only. For this study, the achieved accuracy (< 0.4% and for most materials 0.2%) is sufficient to provide sub percent ground truth relative stopping powers for comparison with values derived from DECT, SECT and Geant4 simulations.

The measured difference in relative proton stopping power between 62 MeV and 149 MeV is within 0.7% for analytical standards. This energy dependence of the relative stopping power is material dependent and increases with decreasing proton energy. In the stopping region this can amount in a difference of the order of 6% with respect to the relative stopping power at 149 MeV. Therefore it is of importance to incorporate the energy dependence of the relative stopping power in treatment planning for proton therapy to avoid unnecessary loss of accuracy in dose calculation.

With the stoichiometric SECT calibration method as well as the proposed DECT method, relative proton stopping powers are calculated using an approximation of the Bethe-Bloch formalism. The impact of the correction terms, which are neglected in this approximation of the proton stopping power, is estimated at 1 to 1.5% for clinically relevant proton energies. For calculation of relative proton stopping powers these correction terms contribute less than 0.3%. Bragg's additivity rule is used for calculation of mean excitation energies for compounds in both the SECT and DECT methods and in the Geant4 Monte Carlo simulations. This requires elemental mean excitation energies, which are not precisely known. In addition, different values are proposed for the mean excitation energy of water. With the current available theory and mean excitation energies, relative stopping powers have been predicted by the proposed DECT method with an accuracy better than 2% for most assessed materials. A similar accuracy has been observed for Geant4 simulations. The differences between the DECT method and Geant4 simulations compared to the experimentally determined relative stopping powers are predominantly positive. The two most likely explanations for these systematic positive deviations are an underestimation of elemental mean excitation energies[73,74] and/or an overestimation of the mean excitation energy of water. In this study the ICRU recommended value for the mean excitation energy of water of 78 eV[67] is used. For mean excitation energies of the elements the ICRU recommended values of ICRU report 37[71] are used. Bragg's additivity rule with these elemental mean excitation energies gives a mean excitation energy for water of 69 eV. This is not consistent with the ICRU recommended value of 78 eV. A decrease from the applied 78 eV for water to the previously accepted value of 75 eV[71,75] yields a reduction of 0.5% and selection of 69 eV yields a reduction of 1.5% in relative stopping powers. This would lead to an improved correspondence of the DECT predicted relative stopping powers with the experimental values. For more accurate relative stopping power prediction, an accurate determination of elemental mean excitation energies and verification of Bragg's additivity rule for compounds (including water) is required.

6.4 Dual energy CT compared to single energy CT for relative stopping power estimation

In chapter 5 we compare the accuracy of relative stopping power predictions using the stoichiometric SECT method with the DECT method on an image basis. The stoichiometric single energy CT calibration method relates a CT number measured at a single x-ray tube voltage to a relative stopping power by deriving a composition and density or directly using a calibration curve. This is not specific since different tissues can have the same CT numbers on a SECT image but differ in composition, density and relative stopping power. The validity of the SECT method is limited to materials and tissues with a composition as well as density very similar to the materials used for the calibration. Dual energy CT tissue characterization allows a physics based determination of the electron density the accuracy of which is independent of the materials. With these electron densities and mean excitation energies derived from the calibrated effective atomic numbers, relative stopping powers have been determined which are close to experimental values. Larger differences have only been found for materials without hydrogen in their composition. The relative differences with respect to experimental relative stopping powers are between -21 and 16% (difference -3.0±7.8%) for SECT while for DECT the differences are mainly within 3.5% (difference 2.0±2.2%) for the 32 assessed materials. When a mean excitation energy of 69 eV is selected for water the accuracy of DECT for the materials is within about 2% (figure 6.1). The differences for 17 bovine tissues are within 3.6% (difference 1.3±1.3%) for SECT and 3.3% (difference 2.3±0.5%) for DECT of experimental values, except for the bone samples. With a mean excitation energy of water of 69 eV the differences for DECT reduce to less than 1.8% for the tissues with respect to experimental relative stopping powers while the differences for SECT remain within 3.5%. SECT proved to be more susceptible for partial volume averaging effects between e.g. air and bone in the bone samples and yields large deviations (~20%) in these cases. The DECT method is based on the physics interactions of photons with tissue and is more robust to patient specific variations in composition and density of the tissues. Therefore, DECT leads to an improved physical quality of proton therapy treatment planning.

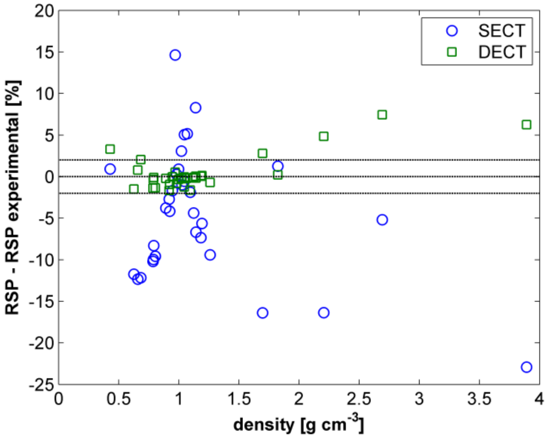

Figure 6.1. Relative differences between relative stopping powers (RSPs) determined with single energy CT (SECT) and dual energy CT (DECT) compared to experimental RSPs as a function of mass density for 32 materials. The RSPs are derived with a mean excitation energy for water of 69 eV. The horizontal lines represent differences of ±2% and 0%, respectively.

For current clinical practice using SECT, high resolution imaging is of importance to restrict partial volume averaging and visualize small air cavities which cause range shifts. Schaffner and Pedroni estimated the uncertainty associated with the conversion of patient CT data to relative proton stopping powers at 1.8% for bone and 1.1% for soft tissue[18]. The uncertainty due to the calibration curve alone was estimated at 1%[18]. This uncertainty combined with an uncertainty in measured CT numbers of ~2% leads to the widely adopted range uncertainty in the order of 3.5%[16]. We have measured differences for the tissue substitutes and soft tissues up to 3.6%. For other materials that have tissue-like compositions based on C, H or C, H, O, larger differences between measured and predicted relative stopping powers (~10%) have been found for the stoichiometric SECT method. Materials like ceramics used in prostheses and silicone oil used in treatment of ocular tumours deviate even more while the results from the DECT method do not show these large differences. This confirms that SECT is not material specific and cannot provide patient specific tissue relative stopping powers. Careful reconsideration of the clinically applied range uncertainty is therefore desired. A patient specific method could improve the accuracy of proton therapy treatment planning. The proposed DECT method has proven to be more accurate and material specific.

6.5 Possible future developments

Spectral CT can provide linear attenuation coefficients for more energy bins. With these attenuation coefficients it might be possible to reconstruct an attenuation curve for each voxel. However, the attenuation curves for different tissues lie close together, like the curves of the tissue substitutes given in figure 6.2. Therefore, extracting a composition from these curves will not be completely model independent. The *K*-edges of tissues (elements with a $Z < 20$) are below 4 keV while the spectral range in CT between 1 and 30 keV is filtered out by x-ray tube prefiltration and attenuation in the patient. Spectral CT might improve the estimate of the local weighting function introduced in chapter 2 eq. (4). By using a reconstructed $\bar{\mu}_j(E,\boldsymbol{r})$ for each energy bin instead of an average $\bar{\mu}_j(\boldsymbol{r})$ for the whole spectral distribution a more specific local weighting function could be calculated. This might improve the accuracy in determining the electron density and effective atomic number.

Accurate tissue characterization with DECT critically depends on the accuracy with which the measured CT numbers represent the linear attenuation coefficients of the scanned materials. In this work we used reconstructed CT numbers which included a water beam hardening correction. Consequently, systematic deviations have been found in the derived effective atomic numbers. It would be of interest to apply the method described in chapter 2 on raw (spectral) CT data combined with an accurate description of the reconstruction and measurement process.

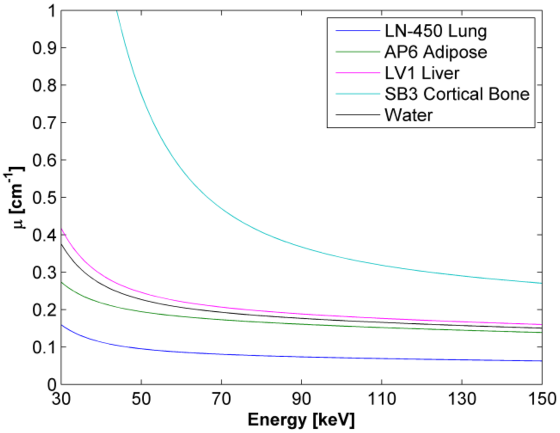

Figure 6.2. Linear attenuation coefficient μ as a function of energy for different tissue substitutes and water.

Different studies have investigated the potential of DECT for deriving the composition and density of the tissue for dose calculation[37,78]. Landry *et al.*[48] presented a simulation study on tissue segmentation for brachytherapy Monte Carlo dose calculation using the effective atomic number and relative electron density. With DECT the dose calculation errors were reduced with respect to SECT based segmentation but tissues with very similar effective atomic numbers and relative electron densities could not be distinguished.

For in vivo dose verification in particle therapy an accurate determination of the composition of the tissue is needed to predict the PET- and prompt gamma production. An imaging modality providing information that is more specific for the composition is required to allow accurate quantification of the tissue composition and density.

Proton CT can provide tissue proton stopping powers from the interaction of protons with the tissue. This could lead to an accuracy gain with respect to the use of DECT[91]. The spatial resolution in proton CT is limited by multiple Coulomb scattering. By selecting only protons which are scattered over a small angle the spatial resolution improves. The use of higher energy (~200 MeV) protons for proton CT provides less scattering and a better soft tissue contrast compared to low energy protons. The accuracy in relative stopping power estimation which can be achieved with proton CT critically depends on the accuracy of the proton energy measurement before and after the patient. A 1% range uncertainty requires an energy resolution of 0.6% at 200 MeV[92]. In practice, relative stopping power images derived from DECT could be calibrated by proton radiography or proton CT.

6.6 Clinical implementation of dual energy CT for proton therapy

Accurate determination of electron densities and relative stopping powers with DECT requires a good separation of the two x-ray photon spectra. A high energy spectrum where the interactions with the tissue are dominated by Compton scattering can be achieved with a tube voltage of 150 kV combined with a tin (Sn) filter. The best results are obtained if 150 kV Sn is combined with a low energy tube voltage of 90 kV for enhanced photoelectric absorption. When the tube voltage is further reduced to 80 kV, beam hardening artefacts appear in the images which limit the image quality.

For clinical implementation of DECT for proton therapy treatment planning, collaboration with a vendor for treatment planning software is needed. The DECT method could then be included in the dose calculation software. This would enable quantification of the difference in dose distributions for proton therapy between relative stopping powers derived using the SECT and DECT method. The differences for photon dose calculations when using DECT derived electron densities with respect to values obtained with a SECT calibration curve would be of interest to assess.

With the DECT method relative proton stopping powers can be determined on an image basis with accuracy better than 2% when inconsistensies in mean excitation energies are solved. The validity of the DECT method for materials without hydrogen in their composition has to be individually verified. Relative proton stopping powers predicted by the stoichiometric SECT calibration method deviate -23 to 15% for arbitrary materials by a mean excitation energy of water of 69 eV. For tissues and tissue substitutes, relative proton stopping powers have been determined with accuracy better than 3.5% except for bone (~20%). Due to the small validity bandwidth and non-patient specificity of the stoichiometric SECT method no single uncertainty value can be given for all human tissues.

The improvement in the accuracy of tissue relative proton stopping powers which can be accomplished with the DECT method is likely to be of great benefit for the accuracy of dose calculations in proton therapy.

Nederlandse Samenvatting

Inleiding

In de afgelopen decennia hebben toegenomen kennis en nieuwe technologische ontwikkelingen geleid tot een verbetering in de kwaliteit van de behandeling bij kanker. Het succes van de behandeling neemt toe maar kanker blijft een moeilijke ziekte om te genezen gezien de vijfjaarsoverleving van patiënten slechts rond de 60% is[1]. De prognose hangt wel sterk af van het type tumor en de uitbreiding van de ziekte. Verdere verbetering van de behandeling is nodig om een hogere genezingsgraad te kunnen bereiken.

Radiotherapie is een vorm van behandeling die gebruik maakt van ioniserende straling. Bij conventionele radiotherapie vindt uitwendige bestraling met hoog-energetische fotonen of elektronen plaats of inwendige bestraling via in het lichaam gebrachte radioactieve bronnen. De behandeling met fotonen is in de loop van de tijd sterk geoptimaliseerd met betrekking tot dosisreductie (reductie van de geabsorbeerde energie) in de kritieke structuren die rond de tumor liggen. De te behalen verbetering wordt echter beperkt door de manier waarop fotonen hun energie afgeven in het weefsel. Deze energieafgifte van fotonen geeft een hoge intreedosis en een min of meer exponentiele afname van de dosis met diepte (figuur S1). Protonentherapie is een vorm van radiotherapie die in opkomst is. Protonen geven hun energie geleidelijk af bij het doordringen in het weefsel. Het energieverlies neemt toe als de energie van de protonen afneemt. Aan het einde van hun pad verliezen de protonen lokaal veel energie en geven een hoge dosis af, de zogenaamde Bragg piek (figuur S1). De positie van de Bragg piek kan gevarieerd worden door de energie van de protonen te veranderen. Na de Bragg piek zijn de protonen gestopt in het weefsel en is er geen dosisafgifte meer. Hierdoor is het mogelijk om met protonen een hogere conformiteit van het hoge-dosis gebied aan het tumorvolume te bereiken. Dit kan leiden tot een lager risico op complicaties en stralingsgeïnduceerde tumoren. In het bijzonder voor patiënten met een tumor in het hoofd-hals gebied en voor kinderen kan dit in veel gevallen een betere prognose en kwaliteit van leven opleveren.

Door de lokale hoge dosis die protonen afgeven is het van groot belang dat het energieverlies van de protonen in het weefsel erg nauwkeurig voorspeld wordt. Onnauwkeurigheden hierin kunnen leiden tot een hoge dosis in gezond weefsel of geen dosis in een deel van de tumor. Om nauwkeurig te kunnen berekenen hoe de protonen hun energie overdragen aan het weefsel is kwantitatieve informatie van het weefsel nodig in termen van het verwachte energieverlies van protonen per afgelegde afstand (proton stopping power). De proton stopping power wordt vaak genormaliseerd op de proton stopping power van water tot een relatieve stopping power (RSP). Deze RSP wordt in de klinische praktijk verkregen uit röntgen-computertomografie (CT)-gegevens van de patiënt. Bij CT wordt de verzwakking van een fotonenbundel gemeten en omgezet in CT-waarden die samen een afbeelding van een doorsnede van de patiënt vormen. Voor dosisberekeningen in protonentherapie wordt een CT-scan met één fotonenergiespectrum (single energy CT, SECT) gemaakt. Een stoichiometrische kalibratiemethode relateert de gemeten CT-waarden aan de RSP's[18,34].

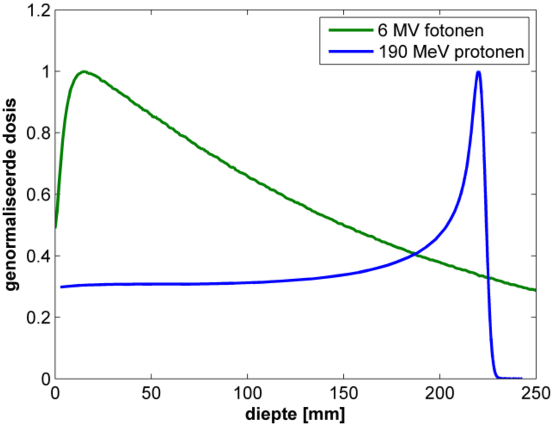

Figuur S1. Genormaliseerde dosis-diepte curves in water voor 6 MV fotonen en 190 MeV protonen.

In deze studie wordt een nieuwe methode gepresenteerd om weefsels te karakteriseren op basis van CT-beeldvorming bij twee fotonenergiespectra (dual energy CT, DECT). DECT levert twee afbeeldingen op met CT-waarden waaruit de elektronendichtheid en het effectieve atoomgetal van elk weefsel bepaald kunnen worden. Vanuit deze twee weefselspecifieke parameters kunnen RSP's worden bepaald. De nauwkeurigheid van deze DECT methode is onderzocht en vergeleken met de SECT kalibratiemethode. Hierbij zijn als referentiewaarden experimentele RSP's gebruikt die bepaald zijn aan de hand van zeer nauwkeurige metingen van de protondracht (indringdiepte van de protonen).

Dual energy CT weefselkarakterisatie voor protonentherapie planning

Een gereconstrueerde CT-afbeelding geeft een matrix met CT-waarden (Hounsfield units) die de lineïeke verzwakkingscoëfficiënten van het weefsel voor fotonen relatief aan water weergeven. De verzwakking is afhankelijk van de verschillende processen waarmee fotonen in wisselwerking treden met materie. De mate waarin elk van deze interactieprocessen optreedt, is afhankelijk van de energie van de fotonen en van de elektronendichtheid en samenstelling van het weefsel.

Dual energy CT geeft lineïeke verzwakkingscoëfficiënten voor twee fotonenspectra en biedt daarom extra informatie ten opzichte van single energy CT dat één fotonenspectrum gebruikt (figuur S2). Dit voordeel van DECT kan worden benut door een theoretische beschrijving te gebruiken van de afhankelijkheid van de lineïeke verzwakkingscoëfficiënt van de elektronendichtheid en het atoomgetal. Deze theoretische beschrijving, spectraal gewogen met de gebruikte fotonenspectra in de dual energy acquisitie (figuur S2), maakt het mogelijk om uit de twee gemeten lineïeke verzwakkingscoëfficiënten een effectief atoomgetal en een elektronendichtheid te bepalen. Dit is een natuurlijke parameterisatie van deze fysisch tweevoudige afhankelijkheid van de lineïeke verzwakkingscoëfficiënt. Met een iteratieve optimalisatieprocedure waarbij, op basis van de bepaalde effectieve atoomgetallen en elektronendichtheden, de spectrale weging wordt aangepast kunnen elektronendichtheden met een hoge nauwkeurigheid worden bepaald (~1%).

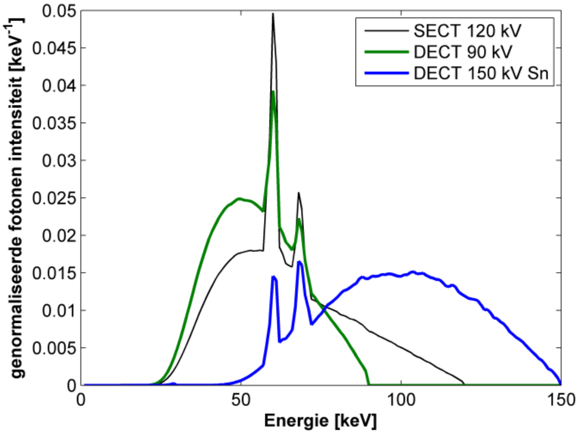

Figuur S2. Spectrale fotondistributies bij röntgenbuisspanningen van 120 kV, gebruikt voor de SECT acquisitie, en 90 kV en 150 kV (met extra tin filter) gebruikt voor de DECT acquisitie. De data geeft de spectra van de SOMATOM Force weer en is afkomstig van Siemens Medical Solutions, Forchheim, Germany.

Het energieverlies van protonen in weefsel wordt bepaald door de elektronendichtheid en de gemiddelde excitatie-energie welke afhangt van het atoomgetal. De gemiddelde excitatie-energie geeft de minimaal mogelijke energieoverdracht in een botsing van het proton met een elektron in het materiaal weer.

De elektronendichtheid die met DECT bepaald wordt, kan direct gebruikt worden voor de berekening van het energieverlies van protonen en dus voor dosisberekeningen voor protonentherapie. Het effectief atoomgetal is lastiger te interpreteren. De waarde van het effectieve atoomgetal wordt bepaald door de wijze waarop de verschillende interactieprocessen van de fotonen met het materiaal afhangen van het atoomgetal van dat materiaal. Zowel in de gemeten lineïeke verzwakkingscoëfficiënten als in de bepaalde effectieve atoomgetallen is een systematische afwijking gevonden. Deze afwijking wordt hoogstwaarschijnlijk veroorzaakt door een fenomenologische correctie in het CT reconstructieproces voor opharding van het fotonenspectrum (het filteren van laag energetische fotonen) als de bundel door een materiaal gaat. Deze correctie, die gebaseerd is op water, leidt tot een systematische afwijking van de CT-waarden voor andere materialen dan water. Het effectief atoomgetal is gecorrigeerd voor deze systematische afwijking waarna een verband is bepaald tussen de gekalibreerde waarden en de gemiddelde excitatie-energie. Met dit verband en de uit DECT bepaalde elektronendichtheden kunnen proton stopping powers worden uitgerekend. Deze stopping powers kunnen worden gebruikt voor het voorspellen van het energieverlies van protonen in weefsels voor protonentherapie planning.

Energieverlies van protonen

Met protonenbundels van het AGOR cyclotron zijn dosis-diepte metingen in een waterfantoom uitgevoerd (zie figuur S1). De dracht van protonen in water is in verschillende experimenten bepaald met een onzekerheid kleiner dan 0.03 mm. Om relatieve stopping powers van verschillende materialen en weefsels te meten, zijn deze materialen in water gepositioneerd om vervolgens het verschil in dracht te meten ten opzichte van de meting in alleen water. Uit de gemeten drachtverschillen en nauwkeurige metingen van de materiaaldikten zijn relatieve stopping powers voor 32 onderzochte materialen bepaald met een onzekerheid < 0.4% (voor de meeste materialen 0.2%).

Naast metingen met protonen zijn ook dosis-diepte simulaties met de Geant4 Monte Carlo code uitgevoerd. De protonen en andere deeltjes worden in deze simulaties gevolgd en er wordt berekend hoeveel energie ze afgeven aan het medium via de verschillende interactieprocessen. De gesimuleerde dosis-diepte curves in water komen goed overeen met de metingen. Hiermee is de simulatie voor water gevalideerd en is vervolgens bij het toevoegen van verschillende materialen in het water gekeken naar het effect hiervan op de dracht van de protonen. Uit deze simulaties zijn ook relatieve stopping powers bepaald.

Relatieve stopping powers

De relatieve stopping power is energieafhankelijk. Deze energieafhankelijkheid hangt af van het materiaal en neemt toe met afnemende energie van de protonen. Voor analytische standaarden zijn verschillen in RSP's gemeten tot 0.7% tussen 62 MeV en 149 MeV protonen. Bij lage energie, in het gebied waar de protonen stoppen, kan dit verschil ten opzichte van 149 MeV protonen oplopen tot 6%. Om onnodig nauwkeurigheidsverlies in dosisberekeningen te voorkomen is het van belang dat de energieafhankelijkheid van de RSP meegenomen wordt in de planning voor protonen therapie.

Zowel de stoichiometrische SECT kalibratiemethode als de DECT methode gebruiken een benadering van de Bethe-Bloch vergelijking om RSP’s te berekenen. De invloed van de verwaarloosde correctietermen in deze benadering op de proton stopping power is geschat op 1 tot 1.5% maar het effect op de RSP is kleiner dan 0.3%. Bij het bepalen van de gemiddelde excitatie-energieën voor de SECT en DECT methode is een sommatieregel gebruikt, ook wel bekend als Bragg’s additivity rule. Voor het toepassen van deze regel zijn gemiddelde excitatie-energieën nodig van de elementen die in het materiaal voorkomen. Deze gemiddelde excitatie-energieën van de elementen zijn niet nauwkeurig bekend en mogelijk onderschat. Daarnaast is er voor het bepalen van de RSP ook een gemiddelde excitatie-energie van water nodig. In deze studie is hiervoor een recent door de ICRU voorgestelde waarde van 78 eV[67] gebruikt. Als Bragg’s additivity rule wordt toegepast voor water, consistent met de SECT en DECT methoden, geeft dit echter een gemiddelde excitatie-energie van 69 eV. Dit levert een reductie in de RSP op van 1.5% vergeleken met RSP’s die bepaald zijn met SECT en DECT bij een waarde van 78 eV. Binnen deze aangegeven onzekerheden zijn RSP’s bepaald met DECT met een nauwkeurigheid beter dan 2% voor de meeste onderzochte materialen. De RSP’s die bepaald zijn aan de hand van de Geant4 Monte Carlo simulaties hebben een vergelijkbare nauwkeurigheid. Zowel de DECT als de Geant4 voorspelde RSP’s vertonen systematische positieve verschillen met de experimenteel bepaalde RSP’s, die reduceren bij gebruik van Bragg’s additivity rule voor het bepalen van de gemiddelde excitatie-energie van water.

Single energy en dual energy CT voor het bepalen van relatieve stopping powers

De stoichiometrische SECT kalibratiemethode relateert de CT-waarden die gemeten zijn met één fotonenspectrum aan een RSP op basis van berekende CT-waarden en RSP’s voor gemiddelde weefselsamenstellingen en dichtheden[17,39]. Omdat de gemeten CT-waarden afhankelijk zijn van zowel de dichtheid als de samenstelling van het materiaal is deze methode niet specifiek. Dit houdt in dat materialen met een verschillende dichtheid en samenstelling dezelfde CT-waarde kunnen opleveren. Daarnaast komen de gemiddelde weefselsamenstellingen en dichtheden niet precies overeen met de samenstellingen en dichtheden van de weefsels in een willekeurige patiënt. De geldigheid van de SECT kalibratiemethode is beperkt tot materialen en weefsels die in samenstelling en dichtheid sterk lijken op de materialen die gebruikt zijn voor de kalibratie. De dual energy CT methode bepaalt de elektronendichtheid en de gemiddelde samenstelling uit gemeten CT-waarden voor twee fotonenspectra en is daarom materiaalspecifiek.

De nauwkeurigheden van de SECT en de DECT methoden voor het bepalen van RSP's zijn vergeleken op basis van verkregen RSP afbeeldingen. De relatieve verschillen voor de 32 onderzochte materialen variëren voor SECT tussen de -21% en 16% (verschil -3.0±7.8%) ten opzichte van experimentele RSP's. Voor DECT zijn de verschillen hoofdzakelijk binnen 3.5% (verschil 2.0±2.2%). Alleen voor materialen die geen waterstof bevatten zijn de verschillen groter. Als een gemiddelde excitatie-energie voor water van 69 eV wordt toegepast valt de nauwkeurigheid van DECT voor de meeste materialen binnen 2% (figuur S3). Voor 15 onderzochte weefsels zijn de verschillen voor SECT binnen 3.6% (verschil 1.3±1.3%) en voor DECT binnen 3.3% (verschil 2.3±0.5%) in vergelijking met de experimentele waarden. Een gemiddelde excitatie-energie voor water van 69 eV brengt de met DECT bepaalde RSP's van de weefsels binnen een nauwkeurigheid van 1.8%, terwijl de RSP's die verkregen zijn met SECT binnen 3.5% van de experimentele waarden blijven. De verschillen ten opzichte van experimentele RSP's voor de twee gemeten botschijven zijn voor SECT erg groot (~20%). Door vermenging van lucht en botpoeder in deze schijven is de dichtheid relatief laag terwijl het effectief atoomgetal van het botsample hoog is. Dit levert een hoog CT nummer op en leidt tot een overschatting van de RSP op basis van de SECT kalibratiemethode. De nauwkeurigheid van DECT is voor dit zogenoemde partial volume effect (middeling van CT-waarden voor verschillende materialen in een volume element) veel minder gevoelig doordat de methode gebaseerd is op de fysische interacties van de fotonen met het weefsel. Omdat de DECT methode zowel een effectief atoomgetal als een electronendichtheid bepaalt, is de methode robuust voor patiëntspecifieke variaties in samenstelling en dichtheid van het weefsel. De DECT methode kan patiëntspecifieke RSP's geven waar SECT alleen generieke RSP's geeft.

In de literatuur wordt de onzekerheid in de SECT kalibratiecurve geschat op 1%[18] en de onzekerheid in de gemeten CT-waarden op ~2%. Dit geeft een geschatte onzekerheid in de dracht van ~3.5%[16]. Deze onzekerheid in de dracht wordt breed geaccepteerd en toegepast. In deze studie zijn voor de SECT methode verschillen gevonden in de RSP's van de weefsels binnen 3.5% met uitzondering van bot. Voor bot en willekeurige andere materialen zijn veel grotere verschillen gemeten (~5 tot 20%). De in de literatuur gegeven onzekerheden, die gebaseerd zijn op een zeer beperkt aantal metingen, zijn gegeven deze resultaten te optimistisch.

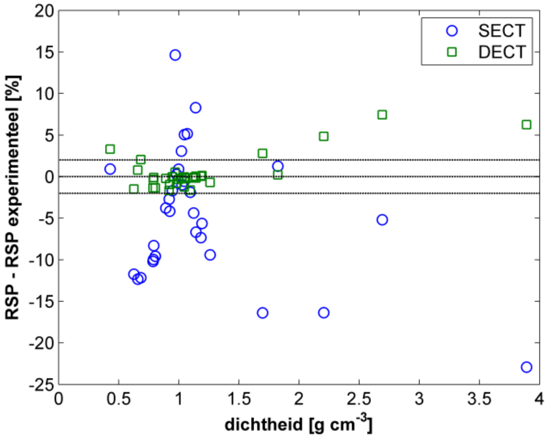

Figuur S3. Relatieve verschillen tussen relatieve stopping powers (RSPs) bepaald met single energy CT (SECT) en dual energy CT (DECT) ten opzichte van experimentele RSPs als functie van de dichtheid voor 32 materialen. De RSPs zijn bepaald bij een gemiddelde excitatie-energie voor water van 69 eV. De horizontale lijnen geven een verschil van respectievelijk ±2% en 0% weer.

Conclusies

Met de DECT methode kunnen relatieve stopping powers voorspeld worden binnen een nauwkeurigheid van 2%, bij consistent gebruik van Bragg's additivity rule voor het bepalen van de gemiddelde excitatie-energie. Voor materialen die geen waterstof bevatten moet de met DECT bepaalde relatieve stopping power apart geverifieerd worden. De SECT kalibratiemethode is alleen geldig voor een beperkte selectie van materialen en weefsels. Gezien de grote afwijkingen die met SECT gevonden zijn voor willekeurige materialen, is het niet mogelijk een algemene onzekerheid in de met SECT te bepalen relatieve stopping power te geven. De verbetering in de nauwkeurigheid waarmee relatieve stopping powers bepaald kunnen worden met de DECT methode, leidt tot een betere overeenkomst tussen de voorspelde en afgeleverde dosisverdeling en kan daarmee klinisch voordeel opleveren voor protonentherapie.

References

[1] Integraal kankercentrum Nederland, http://www.cijfersoverkanker.nl/.

[2] Health Council of the Netherlands, "Proton radiotherapy. Horizon scanning report," Tech. Rep. publication no. 2009/17, The Hague.

[3] V. W. C. Wu, D. L. W. Kwong, and J. S. T. Sham, "Target dose conformity in 3-dimensional conformal radiotherapy and intensity modulated radiotherapy," Radiother. and Oncol. **71**(2), 201–206, 2004.

[4] F. Stieler, D. Wolff, H. Schmid, G. Welzel, F. Wenz, and F. Lohr, "A comparison of several modulated radiotherapy techniques for head and neck cancer and dosimetric validation of VMAT," Radiother. Oncol. **101**(3), 388–393, 2011.

[5] R. R. Wilson, "Radiological Use of Fast Protons," Radiology **47**(5), 487–491, 1946.

[6] H. Paganetti, ed., *Proton therapy physics*. CRC Press Taylor & Francis Group, 2012.

[7] Loma Linda University Cancer Center, http://protons.com/why-choose-loma-linda/our-center.

[8] P. Metcalfe, T. Kron, and P. Hoban, *The physics of radiotherapy x-rays and electrons*. Madison, Wisconsin: Medical Physics Publishing, 2007.

[9] S. R. Cherry, J. A. Sorenson, and M. E. Phelps, *Physics in nuclear medicine*. Saunders, Elsevier, 3rd ed., 2003.

[10] J. E. Turner, *Atoms, radiation and radiation protection*. Weinheim: Wiley-VCH Verlag GmbH & Co. KGaA,, 2007.

[11] W. D. Newhauser and R. Zhang, "The physics of proton therapy," Phys. Med. Biol. **60**(8), R155–R209, 2015.

[12] J.A. Langendijk, P. Lambin, M. Schippers, A.A. van 't Veld, D. De Ruysscher, and M. Verheij, "De introductie van radiotherapie met protonen in Nederland," Nederlands Tijdschrift voor Oncologie **9**(3), 117–129, 2012.

[13] E. Pedroni, S. Scheib, T. Böhringer, A. Coray, M. Grossmann, S. Lin, and A. Lomax, "Experimental characterization and physical modelling of the dose distribution of scanned proton pencil beams," Phys. Med. Biol. **50**(3), 541–561, 2005.

[14] A. Lomax, "Intensity modulation methods for proton radiotherapy," Phys. Med. Biol. **44**(1), 185–205, 1999.

[15] J. Seco and F. Verhaegen, eds., *Monte Carlo Techniques in Radiation Therapy*. CRC Press Taylor & Francis Group, 2013.

[16] J. Schuemann, S. Dowdell, C. Grassberger, C. H. Min, and H. Paganetti, "Site-specific range uncertainties caused by dose calculation algorithms for proton therapy," Phys. Med. Biol. **59**(15), 4007–4031, 2014.

[17] H. Q. Woodard and D. R. White, "The composition of body tissues," Br. J. Radiol. **59**(708), 1209–1218, 1986.

[18] B. Schaffner and E. Pedroni, "The precision of proton range calculations in proton radiotherapy treatment planning: experimental verification of the relation between CT-HU and proton stopping power," Phys. Med. Biol. **43**(6), 1579–1592, 1998.

[19] W. Schneider, T. Bortfeld, and W. Schlegel, "Correlation between CT numbers and tissue parameters needed for Monte Carlo simulations of clinical dose distributions," Phys. Med. Biol. **45**(2), 459–478, 2000.

[20] T. G. Flohr, C. H. McCollough, H. Bruder, M. Petersilka, K. Gruber, C. Süβ, M. Grasruck, K. Stierstorfer, B. Krauss, R. Raupach, A. N. Primak, A. Küttner, S. Achenbach, C. Becker, A. Kopp, and B. M. Ohnesorge, "First performance evaluation of a dual-source CT (DSCT) system," Eur. Radiol. **16**(2), 256–268, 2006.

[21] M. Torikoshi, T. Tsunoo, M. Sasaki, M. Endo, Y. Noda, Y. Ohno, T. Kohno, K. Hyodo, K. Uesugi, and N. Yagi, “Electron density measurement with dual-energy x-ray CT using synchrotron radiation,” Phys. Med. Biol. **48**(5), 673–685, 2003.

[22] J. K. Van Abbema, A. Van der Schaaf, W. Kristanto, J. M. Groen, and M. J.W. Greuter, “Feasibility and accuracy of tissue characterization with dual source computed tomography,” Physica Medica **28**(1), 25–32, 2012.

[23] M. Yang, G. Virshup, J. Clayton, X. R. Zhu, R. Mohan, and L. Dong, “Theoretical variance analysis of single- and dual-energy computed tomography methods for calculating proton stopping power ratios of biological tissues,” Phys. Med. Biol. **55**(5), 1343–1362, 2010.

[24] E. Roessl and R. Proksa, “K-edge imaging in x-ray computed tomography using multi-bin photon counting detectors,” Phys. Med. Biol. **52**(15), 4679–4696, 2007.

[25] J. P. Schlomka, E. Roessl, R. Dorscheid, S. Dill, G. Martens, T. Istel, C. Bäumer, C. Herrmann, R. Steadman, G. Zeitler, A. Livne, and R. Proksa, “Experimental feasibility of multi-energy photon-counting K-edge imaging in pre-clinical computed tomography,” Phys. Med. Biol. **53**(15), 4031–4047, 2008.

[26] U. Schneider and E. Pedroni, “Multiple Coulomb scattering and spatial resolution in proton radiography,” Med. Phys. **21**(11), 1657–1663, 1994.

[27] R. W. Schulte, V. Bashkirov, M. C. Loss Klock, T. Li, A. J. Wroe, I. Evseev, D. C. Williams, and T. Satogata, “Density resolution of proton computed tomography,” Med. Phys. **32**(4), 1035–1046, 2005.

[28] P. Dendooven, H. J. T. Buitenhuis, F. Diblen, P. N. Heeres, A. K. Biegun, F. Fiedler, M.-J. van Goethem, E. R. van der Graaf, and S. Brandenburg, “Short-lived positron emitters in beam-on PET imaging during proton therapy,” Phys. Med. Biol. **60**(23), 8923–8947, 2015.

[29] C. Richter, G. Pausch, S. Barczyk, M. Priegnitz, I. Keitz, J. Thiele, J. Smeets, F. Vander Stappen, L. Bombelli, C. Fiorini, L. Hotoiu, I. Perali, D. Prieels, W. Enghardt, and M. Baumann, “First clinical application of a prompt gamma based in vivo proton range verification system,” Radiother. Oncol. **118**(2), 232–237, 2016.

[30] M. Yang, X. R. Zhu, P. C. Park, U. Titt, R. Mohan, G. Virshup, J. E. Clayton, and L. Dong, “Comprehensive analysis of proton range uncertainties related to patient stopping-power-ratio estimation using the stoichiometric calibration,” Phys. Med. Biol. **57**(13), 4095–4115, 2012.

[31] H. Paganetti, “Range uncertainties in proton therapy and the role of Monte Carlo simulations,” Phys. Med. Biol. **57**(11), R99–R117, 2012.

[32] B. Heismann and M. Balda, “Quantitative image-based spectral reconstruction for computed tomography,” Med. Phys. **36**(10), 4471–4485, 2009.

[33] A. J. Lomax, T. Boehringer, A. Coray, E. Egger, G. Goitein, M. Grossmann, P. Juelke, S. Lin, E. Pedroni, B. Rohrer, W. Roser, B. Rossi, B. Siegenthaler, O. Stadelmann, H. Stauble, C. Vetter, and L. Wisser, “Intensity modulated proton therapy: A clinical example,” Med. Phys. **28**(3), 317–324, 2001.

[34] U. Schneider, E. Pedroni, and A. Lomax, “The calibration of CT Hounsfield units for radiotherapy treatment planning,” Phys. Med. Biol. **41**(1), 111–124, 1996.

[35] R. A. Rutherford, B. R. Pullan, and I. Isherwood, “Measurement of effective atomic number and electron density using an EMI scanner,” Neuroradiology **11**(1), 15–21, 1976.

[36] B. J. Heismann, J. Leppert, and K. Stierstorfer, “Density and atomic number measurements with spectral x-ray attenuation method,” J. Appl. Phys. **94**(3), 2073–2079, 2003.

[37] M. Bazalova, J.-F. Carrier, L. Beaulieu, and F. Verhaegen, “Dual-energy CT-based material extraction for tissue segmentation in Monte Carlo dose calculations,” Phys. Med. Biol. **53**(9), 2439–2456, 2008.

[38] ICRP, “Report of the Task Group on Reference Man,” ICRP Publication **23**, 1975.

[39] D. R. White, H. Q. Woodard, and S. M. Hammond, “Average soft-tissue and bone models for use in radiation dosimetry,” Br. J. Radiol. **60**(717), 907–913, 1987.

[40] D. R. White, E. M. Widdowson, H. Q. Woodard, and J. W. T. Dickerson, “The composition of body tissues (ii) Fetus to young adult,” Br. J. Radiol. **64**(758), 149–159, 1991.

[41] M. Saito, “Potential of dual-energy subtraction for converting CT numbers to electron density based on a single linear relationship,” Med. Phys. **39**(4), 2021–2030, 2012.

[42] G. Landry, J. Seco, M. Gaudreault, and F. Verhaegen, “Deriving effective atomic numbers from DECT based on a parameterization of the ratio of high and low linear attenuation coefficients,” Phys. Med. Biol. **58**(19), 6851–6866, 2013.

[43] D. F. Jackson and D. J. Hawkes, “X-ray attenuation coefficients of elements and mixtures,” Physics Reports **70**(3), 169–233, 1981.

[44] M. J. Berger, J. H. Hubbell, S. M. Seltzer, J. Chang, J. S. Coursey, R. Sukumar, D. S. Zucker, and K. Olsen, “XCOM: Photon cross section database (version 1.5).” [Online] Available: http://physics.nist.gov/xcom [11/27/2012], 2010.

[45] P. J. Mohr, B. N. Taylor, and D. B. Newell, “The 2010 CODATA Recommended Values of the Fundamental Physical Constants (Web Version 6.0).” This database was developed by J. Baker, M. Douma, and S. Kotochigova. Available: http://physics.nist.gov/constants, 2011.

[46] H. A. Duisterwinkel, J. K. van Abbema, M. J. van Goethem, R. Kawachimaru, L. Paganini, E. R. van der Graaf, and S. Brandenburg, “Spectra of clinical CT scanners using a portable Compton spectrometer,” Med. Phys. **42**(4), 1884–1894, 2015.

[47] M. Petersilka, H. Bruder, B. Krauss, K. Stierstorfer, and T. G. Flohr, “Technical principles of dual source CT,” Eur. J. Radiol. **68**(3), 362–368, 2008.

[48] G. Landry, P. V. Granton, B. Reniers, M. C. Öllers, L. Beaulieu, J. E. Wildberger, and F. Verhaegen, “Simulation study on potential accuracy gains from dual energy CT tissue segmentation for low-energy brachytherapy Monte Carlo dose calculations,” Phys. Med. Biol. **56**(19), 6257–6278, 2011a.

[49] G. Landry, B. Reniers, P. V. Granton, B. van Rooijen, L. Beaulieu, J. E. Wildberger, and F. Verhaegen, “Extracting atomic numbers and electron densities from a dual source dual energy CT scanner: Experiments and a simulation model,” Radiother. Oncol. **100**(3), 375–379, 2011b.

[50] M. Tsukihara, Y. Noto, T. Hayakawa, and M. Saito, “Conversion of the energy-subtracted CT number to electron density based on a single linear relationship: an experimental verification using a clinical dual-source CT scanner,” Phys. Med. Biol. **58**(9), N135–N144, 2013.

[51] J. K. van Abbema, M.-J. van Goethem, M. J. W. Greuter, A. van der Schaaf, S. Brandenburg, and E. R. van der Graaf, “Relative electron density determination using a physics based parameterization of photon interactions in medical DECT,” Phys. Med. Biol. **60**(9), 3825–3846, 2015.

[52] N. Hünemohr, B. Krauss, C. Tremmel, B. Ackermann, O. Jäkel, and S. Greilich, “Experimental verification of ion stopping power prediction from dual energy CT data in tissue surrogates,” Phys. Med. Biol. **59**(1), 83–96, 2014a.

[53] ICRU, “Tissue substitutes in radiation dosimetry and measurement Report No. 44,” Bethesda, MD, USA, 1989.

[54] A. E. Bourque, J.-F. Carrier, and H. Bouchard, “A stoichiometric calibration method for dual energy computed tomography,” Phys. Med. Biol. **59**(8), 2059–2088, 2014.

[55] N. Hünemohr, N. Niebuhr, and S. Greilich, “Reply to comment on "Experimental verification of ion stopping power prediction from dual energy CT data in tissue surrogates",” Phys. Med. Biol. **59**(22), 7085–7087, 2014b.

[56] M. F. Moyers, M. Sardesai, S. Sun, and D. W. Miller, “Ion stopping powers and CT numbers,” Medical Dosimetry **35**(3), 179–194, 2010.

[57] J. Perl, J. Shin, J. Schümann, B. Faddegon, and H. Paganetti, “TOPAS: An innovative proton Monte Carlo platform for research and clinical applications,” Med. Phys. **39**(11), 6818–6837, 2012.

[58] S. Agostinelli *et al.*, “Geant4: a simulation toolkit,” Nuclear Instruments and Methods in Physics Research A **506**(3), 250–303, 2003.

[59] J. F. Ziegler, “Stopping of energetic light ions in elemental matter,” J. Appl. Phys. **85**(3), 1249–1272, 1999.

[60] H. Bichsel, “Shell corrections in stopping powers,” Phys. Rev. A **65**, 052709–1–11, 2002.

[61] W. H. Bragg and R. Kleeman, “On the α particles of radium, and their loss of range in passing through various atoms and molecules,” Phil. Mag. Series 6 **10**(57), 318–340, 1905.

[62] R. Zhang and W. D. Newhauser, “Calculation of water equivalent thickness of materials of arbitrary density, elemental composition and thickness in proton beam irradiation,” Phys. Med. Biol. **54**(6), 1383–1395, 2009.

[63] E. R. van der Graaf, R. W. Ostendorf, M.-J. van Goethem, H. H. Kiewiet, M. A. Hofstee, and S. Brandenburg, “AGORFIRM, the AGOR facility for irradiations of materials,” Radiation and its Effects on Components and Systems (RADECS) pp. 451–454, 2009.

[64] IAEA, “Absorbed dose determination in external beam radiotherapy: An international code of practice for dosimetry based on standards of absorbed dose to water,” Technical Reports Series 398, International Atomic Energy Agency, 2000.

[65] S. N. Boon, P. van Luijk, J. M. Schippers, H. Meertens, J. M. Denis, S. Vynckier, J. Medin, and E. Grusell, “Fast 2D phantom dosimetry for scanning proton beams,” Med. Phys. **25**(4), 464–475, 1998.

[66] Y. Kumazaki, T. Akagi, T. Yanou, D. Suga, Y. Hishikawa, and T. Teshima, “Determination of the mean excitation energy of water from proton beam ranges,” Radiation Measurements **42**(10), 1683–1691, 2007.

[67] P. Sigmund, A. Schinner, and H. Paul, “Errata and Addenda for ICRU Report 73, Stopping of ions heavier than helium,” tech. rep., ICRU, 2009.

[68] D. Schardt, P. Steidl, M. Krämer, U. Weber, K. Parodi, and S. Brons, “Precision Bragg-curve measurements for light-ion beams in water,” tech. rep., GSI, Darmstadt, Germany, 2007.

[69] A. Weber, D. Cordini, J. Heufelder, R. Stark, L. Moser, A. Joussen, and G. Willerding, “Influence of density variations on the proton range in therapy of ocular tumors,” Physical and biological basis of hadron radiotherapy. Book of abstracts , 2011.

[70] A. Weber, D. Cordini, R. Stark, and J. Heufelder, “The influence of silicone oil used in ophthalmology on the proton therapy of uveal melanomas,” Phys. Med. Biol. **57**(24), 8325–8341, 2012.

[71] ICRU, “Stopping powers for electrons and positrons Report No. 37,” Bethesda, MD, USA, 1984.

[72] J. F. Ziegler, J. P. Biersack, and M. D. Ziegler, *SRIM The Stopping and Range of Ions in Matter*. Chester, MD: SRIM Co., 2008.

[73] H. Bichsel and T. Hiraoka, “Energy loss of 70 MeV protons in elements,” Nuclear Instruments and Methods in Physics Research Section B: Beam Interactions with Materials and Atoms **66**(3), 345–351, 1992.

[74] T. Hiraoka, K. Kawashima, K. Hoshino, A. Fukumura, and H. Bichsel, “Energy loss of 70 MeV protons in organic polymers,” Med. Phys. **20**(1), 135–141, 1993.

[75] ICRU, “Stopping powers for protons and alpha particles Report No. 49,” Bethesda, MD, USA, 1993.

[76] A. Besemer, H. Paganetti, and B. Bednarz, “The clinical impact of uncertainties in the mean excitation energy of human tissues during proton therapy,” Phys. Med. Biol. **58**(4), 887–902, 2013.

[77] N. Hudobivnik, F. Schwarz, T. Johnson, L. Agolli, G. Dedes, T. Tessonnier, F. Verhaegen, C. Thieke, C. Belka, W. H. Sommer, K. Parodi, and G. Landry, “Comparison of proton therapy treatment planning for head tumors with a pencil beam algorithm on dual and single energy CT images,” Med. Phys. **43**(1), 495–504, 2016.

[78] N. Hünemohr, H. Paganetti, S. Greilich, O. Jäkel, and J. Seco, “Tissue decomposition from dual energy CT data for MC based dose calculation in particle therapy,” Med. Phys. **41**(6), 061714–1–14, 2014c.

[79] L. Beaulieu, A. Carlsson Tedgren, J.-F. Carrier, S. D. Davis, F. Mourtada, M. J. Rivard, R. M. Thomson, F. Verhaegen, T. A. Wareing, and J. F. Williamson, “Report of the task group 186 on

model-based dose calculation methods in brachytherapy beyond the TG-43 formalism: Current status and recommendations for clinical implementation," Med. Phys. **39**(10), 6208–6236, 2012.

[80] H. Bichsel, "Stopping power and ranges of fast ions in heavy elements," Phys. Rev. A **46**, 5761–5773, Nov 1992.

[81] J. C. Ashley, R. H. Ritchie, and W. Brandt, "Z_1^3 effect in the stopping power of matter for charged particles," Phys. Rev. B **5**, 2393–2397, 1972.

[82] P. Bauer and D. Semrad, "Chemical and physical state effects in electronic stopping," in *Theory of the Interaction of Swift Ions with Matter.*, vol. 46, Part 2 of *Advances in Quantum Chemistry*, pp. 153–163, Academic Press, 2004.

[83] M. J. Berger, J. S. Coursey, M. A. Zucker, and J. Chang, "ESTAR, PSTAR, and ASTAR: Computer Programs for Calculating Stopping-Power and Range Tables for Electrons, Protons, and Helium Ions (version 1.2.3)." [Online] Available: http://physics.nist.gov/Star [03/30/2016], 2005.

[84] JCGM/WG 1, "Evaluation of measurement data - Guide to the expression of uncertainty in measurement," JCGM 100:2008, Joint Committee for Guides in Metrology, 2008.

[85] M. Witt, U. Weber, D. Kellner, R. Engenhart-Cabillic, and K. Zink, "Optimization of the stopping-power-ratio to Hounsfield-value calibration curve in proton and heavy ion therapy," Z. Med. Phys. **25**(3), 251–263, 2015.

[86] O. Jäkel, C. Jacob, D. Schardt, C. P. Karger, and G. H. Hartmann, "Relation between carbon ion ranges and x-ray CT numbers," Med. Phys. **28**(4), 701–703, 2001.

[87] J. F. Janni, "Proton range-energy tables, 1 keV-10 GeV," Atomic Data and Nuclear Data Tables **27**(2), 147–339, 1982.

[88] R. E. Alvarez and A. Macovski, "Energy-selective reconstructions in X-ray computerised tomography," Phys. Med. Biol. **21**(5), 733–744, 1976.

[89] E. Rietzel, D. Schardt, and T. Haberer, "Range accuracy in carbon ion treatment planning based on CT-calibration with real tissue samples," Radiation Oncology **2**(1), 1–9, 2007.

[90] S. N. Boon, *Dosimetry and Quality Control of Scanning Proton beams*. PhD thesis, University of Groningen, 1998.

[91] D. C. Hansen, J. Seco, T. S. Sorensen, J. B. B. Petersen, J. E. Wildberger, F. Verhaegen, and G. Landry, "A simulation study on proton computed tomography (CT) stopping power accuracy using dual energy CT scans as benchmark," Acta Oncologica **54**(9), 1638–1642, 2015.

[92] G. Poludniowski, N. M. Allinson, and P. M. Evans, "Proton radiography and tomography with application to proton therapy," Br. J. Radiol. **88**(1053), 20150134, 2015.

Dankwoord

Een groot ‘dank jullie wel voor jullie betrokkenheid en hulp’ zou kunnen volstaan, maar ik wil hier toch graag nog een paar extra woorden aan wijden.

Emiel, de afgelopen jaren waren er periodes van ‘dagelijks’ uitwisselen van ideeën, ‘hele dagen’ experimenteren en ‘dagenlang’ conferenties bezoeken. Je bent altijd toegankelijk, kan erg goed luisteren en waardevolle suggesties doen. Dank je wel voor alle support en je vertrouwen. Sytze, jou kennis was van grote waarde voor het interpreteren van de theorie en de experimentele data. Je hebt altijd ideeën voor nieuwe experimenten en menige discussie volgde jouw gedachten, sprongen in werkelijkheid en tijd. Bedankt voor het zien van kansen, mogelijkheden en vooruitgang. Marcel Greuter, bij jou ben ik begonnen met het dual energy CT onderzoek. Jij zag een nieuwe techniek en we gingen kijken naar de mogelijkheden voor coronaire soft plaque karakterisatie met DECT. We kwamen uit bij kwantitatieve weefsel karakterisatie in termen van effectief atoomgetal en elektronendichtheid wat mogelijk kon worden toegepast voor dosisberekeningen binnen de radiotherapie. Je gaf ruimte om dit uit te zoeken en mailde altijd enthousiast terug, zelfs vanaf Ameland. Arjen van der Schaaf, op dit punt kwam jij in beeld. Je was en bleef geïnteresseerd en positief betrokken bij het onderzoek naar de mogelijke toepassing van DECT voor radiotherapie en in het bijzonder protonentherapie. Bedankt voor je waardevolle suggesties bij menig abstract en manuscript. Ook de andere klinisch fysici bij radiotherapie UMCG (o.a. Arnout van der Borden, Peter van der Hulst, Roel Kierkels, Erik Korevaar en Aart van ’t Veld) zijn betrokken geweest bij dit onderzoek, dank daarvoor. Rozemarijn Vliegenthart en meneer Oudkerk (CMI-NEN, radiologie UMCG), bedankt voor het beschikbaar stellen van de Force CT voor onze metingen waarbij de ondersteuning van Gert Jan Pelgrim, Marleen Vonder, Wim Tukker, Clement Bloupot en Hilko Stoffers van grote waarde was.

Toen we net begonnen aan dit project was ik blij verrast door de expertise die binnen het KVI-CART aanwezig is op het gebied van ontwerp, vormgeving en productie van hoog nauwkeurige experimentele opstellingen. Dankzij de micrometer nauwkeurigheid hebben we met kleine experimentele onzekerheden onze metingen kunnen doen. Ook de elektronica en software nodig voor de aansturing van de translatie stages, bundel en het wegschrijven van de data waren van groot belang voor het succesvol uitvoeren van de protonen experimenten. Bij de experimenten heeft de alertheid van de operateurs, ook diep in de nacht, bijgedragen aan een stabiele bundel en snelle metingen. Allemaal bedankt voor jullie inzet en bijdrage aan dit werk.

Binnen de Medical Physics groep bleven we op de hoogte van elkaars werk en was er ook mogelijkheid tot discussie. De openheid over het werk op alle niveaus maakte mij onderdeel van het geheel. Marc-Jan, Ola en Reint, jullie in het bijzonder bedankt voor het meedenken en werken tijdens de experimenten. Marc-Jan, jou kennis van het systeem en ervaring met het uitvoeren van experimenten heb ik erg gewaardeerd.

Harry, aan het begin van dit onderzoek waren we druk met het klaarstomen van de opstelling waar je veel werk voor hebt verricht. Voor extra functionaliteit had je inventieve oplossingen en wist je altijd de benodigde materialen tevoorschijn te ‘toveren’. We hebben heel wat gelachen bij al dat rondspattende water. Peter, Mariet, Oksana, Tom, Faruk, Nafiseh, Karol en Ikechi, jullie ook bedankt voor de gesprekken bij variërende gelegenheden.

The CT part of this research is performed on the newest generation scanners from Siemens Healthcare and would not have been possible without their cooperation. Karl Stierstorfer, thanks for providing the technical information about the systems and tube output spectra needed for the calculations. Bernhard Schmidt, thank you for the opportunity to collect data in Forchheim and for providing technical information. Bernhard Krauss and Jan Korporaal, thanks for the technical assistance during the data acquisition. Nora Huenemohr we have met at the DECT workshop and later discussed our results during a telephone conference, thank you for your interest.

Tijdens mijn onderzoek kwamen ook verschillende studenten langs voor een project. Erik Duisterwinkel, dank voor je bijdrage aan het ontwikkelen van de Compton spectrometer waar we later bij Siemens metingen van de fotonen spectra van de CT mee hebben kunnen doen. Lucia Paganini, thank you for the time we spent behind Matlab, the tea chats and Italian dishes. Marcel Eleveld en Andrej Sarnatskiy bedankt voor jullie bijdrage aan de CT en protonen metingen van de weefsel samples.

Na het tot stand komen van het manuscript en veelvuldige discussie en optimalisatie rondes kwam het moment om de weergave van dit onderzoek extern aan te bieden ter beoordeling. Meneer Heijmen, mevrouw Koffeman en meneer Schippers, bedankt voor jullie inzet bij het lezen van mijn proefschrift.

In de afgelopen jaren ben je altijd bij mij op de kamer gebleven Josbert. We konden erg goed met ons eigen werk bezig zijn maar hebben ook van gedachten gewisseld over dingen. Bedankt voor het delen van wat je bezig hield en het luisteren naar mijn verhalen. Succes bij het vinden van je weg.

“Sauna?” het waren die appjes die ik altijd met een glimlach las, bedankt Corien en bedankt voor je geduld als het soms weer even duurde omdat ik eerst wat af moest maken. Het waren fijne avonden. Aukelien, je reis vanuit Ashford om deze dag mee te maken weerspiegeld je betrokkenheid de afgelopen jaren. Bedankt Corien en Aukelien dat jullie mijn paranimfen willen zijn.

De museumbezoekjes, shopacties en etentjes waren leuke gelegenheden om bij te praten Janneke over zoveel dat ons bezig hield.

(Schoon) broer(s), zussen en ouders: het was mooi en belangrijk voor mij om dingen met jullie te kunnen delen.

Papa en mama, ontelbare momenten van liefde en betrokkenheid waren ook de afgelopen jaren van grote waarde.

There's a loyalty that's deeper than mere sentiments … Marcel, jij hebt mij altijd gesteund in nieuwe uitdagingen, dit was er één van. Dat ik dit project mag afronden is dan ook zeker aan jou te danken, woorden kunnen dit niet beschrijven … Lisanne en Nivian, de afgelopen jaren zijn jullie deel gaan uitmaken van 'ons'. Elke dag geniet ik van jullie aanwezigheid in mijn leven, jullie vragen om meer van de wereld om je heen te begrijpen en jullie allesveroverende lach…

We hebben elkaar nodig … iedereen die om me heen stond (familie, vrienden, collega's, oppas, buren …) bedankt voor jullie zijn.

List of publications

J. K. van Abbema, M.-J. van Goethem, M. J. W. Greuter, A. van der Schaaf, S. Brandenburg, and E. R. van der Graaf, “Relative electron density determination using a physics based parameterization of photon interactions in medical DECT,” Phys. Med. Biol. 60(9), 3825–3846, 2015.

H. A. Duisterwinkel, J. K. van Abbema, M. J. van Goethem, R. Kawachimaru, L. Paganini, E. R. van der Graaf, and S. Brandenburg, “Spectra of clinical CT scanners using a portable Compton spectrometer,” Med. Phys. **42**(4), 1884–1894, 2015.